ICFO – Institut de Ciències Fotòniques
UPC – Universitat Politècnica de Catalunya

Light absorption and ergodicity in systems that transform light into other forms of energy

Doctoral Thesis by

Catarina Gonçalves Ferreira

Thesis Advisor: **Prof. Jordi Martorell**

Organic Nanostructured Photovoltaics Group

Thesis submitted in partial fulfillment of the requirements
for the degree of Doctor of Philosophy in Photonics

Barcelona, 2023

To my family, friends, and Eduardo

Acknowledgements

A rather long, tough, but extremely rewarding journey of my life is coming to an end, and I cannot help but thank the ones who made it possible for me to get here.

First of all, I would like to thank my supervisor, Professor Jordi Martorell, for the chance he gave me to pursue my PhD studies in his group at ICFO, and for all the guidance he provided me in the past years. Thanks to him, I had the opportunity to conduct state-of-the-art research, in one of the best photonics institutes worldwide, and to have direct contact with cutting-edge science on a daily basis.

I also want to thank all the members of the Organic Nanostructured Photovoltaics group for the assistance they provided me whenever I needed it, but also for the wonderful moments that we shared outside the lab. In this regard, I would like to particularly acknowledge Johann and Quan for introducing me to the lab work and dynamics and for making my transition to the PhD so smooth; Mariia for all the collaborations we worked on together, and for accompanying me during my whole stay at ICFO, sharing with me a lot of good moments, but also struggles; Guillermo for all the scientific discussions we had and for always pushing me to get the best possible results on our shared h-CPP project; Carles for presenting me to the universe of photoelectrochemistry and for all the patience he needed to answer my millions of questions; Francisco for listening to my complaints but also for sharing with me amazing Friday Coffees and laughs; and all the newest members, Valentina, Sidney, Dimitrios, Yatzil, Pavlo, and Kawa, for the wonderful energy they bring in every day and for always putting a smile on my face, even in the toughest moments.

Additionally, I would like to thank the amazing "Xerinola" group: Eduardo, Álvaro, Sandra, José, Ugaitz, Kavitha, and Pamina, for all the extraordinary moments we shared outside ICFO's doors, including dinners, parties, hikes and even skiing! They definitely made my time here better and more joyful.

However, this journey might not have been possible if it was not for my previous supervisor, Professor Senentxu Lanceros-Méndez, who always encouraged me to follow my studies and to keep investing in scientific research. It was thanks to him that I was first introduced to lab work and that I had the chance to be included in an incredible state-of-the-art research group.

On a different note, I cannot forget my longtime friends that I had to leave behind when I decided to embrace this adventure, but that keep supporting me no matter what and are always happy to receive me back in Portugal with their arms wide open: Inês, Rita, Didi, Laura, Miguel, Carlos, Liane, Carol, Catarina L., Bruno M., Paulo, Nelssom, Joana, João, Fábio, Bruno H... Thank you for showing me that friendship lasts no matter the distance!

I would also like to especially thank my whole family for all the unconditional support they gave me during this journey and for always receiving me with a huge smile every time I was returning home. In particular, I must express my gratitude to my parents, without whom I could not have gotten here. They always did their best to make sure I had everything I needed to be successful and they always supported my decisions, no matter what. They always ruled by example, and as they taught me long ago: "Work on whatever you like to, but put all of your efforts into it and try to be the best version of yourself every day".

Last, but certainly not least, I want to thank Eduardo for all his love and support, and for being by my side every single day of this journey. Together, we jumped into this astounding adventure, moved to a foreign country, started a PhD, and grew a lot personally. He laughed and made me laugh in the best moments, and gave me affection and strength in the most difficult times. He really made my life here easy and joyful, and I can only hope to continue by his side on the next ongoing journeys!

To all of you, who made it possible to successfully complete this cycle of my life, I can only say: a thousand "Thank You"!

Abstract

To mitigate the present environmental crisis, caused by the excessive use of fossil fuels and associated release of carbon dioxide into the atmosphere, it is necessary to significantly reduce worldwide energy consumption, to rely more strongly on clean and renewable sources of energy, but also to maximize energy efficiency in currently existent technologies that make use of energy. To reach such maximal energy efficiency, it is necessary to optimize light propagation, harvesting, and utilization in the different existent optoelectronic technologies. Given that a considerable portion of the global energy consumption is dedicated to illumination or devices incorporating illumination sources in them, a clear path to maximize energy-efficiency would imply minimizing the light losses in such kind of systems. In addition, for maximal energy conversion efficiency it is essential to optimize light absorption in systems that perform an unassisted sunlight transformation into other forms of energy, such as electrical or chemical.

To reach the double goal of optimizing light utilization and transformation, in this thesis we consider the study of optical ergodic configurations, where light rays are randomized after a few bounces at the interfaces, losing any correlation with the external incident state and giving rise to an isotropic radiation inside the material. In Chapter 2 of the thesis, we demonstrate that an ergodic geometry can be used to obtain homogeneously distributed polarized light emission. In the same ergodic system, we also demonstrate that the light with the unwanted polarization can be trapped and transformed back into electricity by using a couple of perovskite solar cells. Such features are potentially useful to increase energy efficiency in optoelectronic devices incorporating illumination sources in them, as is the case of liquid crystal displays. A similar ergodic light propagation is also considered in Chapter 3 to determine what the maximal light trapping and effective light absorption is in a $BiVO_4$-based photoanode of a photoelectrochemical cell used for light transformation into hydrogen. The limits in the efficiency of such energy transformation are seen to be strongly linked to the weakly light-absorbing sub-bandgap states. A three-dimensional nano-structuration of the photoanode in the photoelectrochemical cell is explored as a path to eventually reach ergodicity for light propagation in the photoanode. In the final chapter of the thesis, we consider a tandem construction of two complementary light absorption elements, such as a $BiVO_4$ photoanode and an organic solar cell, to obtain an unassisted conversion of sunlight into hydrogen in photoelectrochemical cells. Optical multilayers designed by implementing an inverse problem-solving approach are found to be an essential ingredient to properly balance light absorption among such two light-absorbing elements in the tandem, leading to an optimal solar-to-hydrogen conversion.

Resumen

Para mitigar la actual crisis ambiental, provocada por el uso excesivo de combustibles fósiles y la consiguiente liberación de dióxido de carbono a la atmósfera, es necesario reducir significativamente el consumo mundial de energía, confiar más en fuentes de energía limpias y renovables, pero también maximizar la eficiencia energética en las tecnologías actualmente existentes que hacen uso de la energía. Para alcanzar tal eficiencia energética máxima, es necesario optimizar la propagación, recolección y utilización de la luz en las diferentes tecnologías optoelectrónicas existentes. Dado que una parte considerable del consumo energético mundial se dedica a la iluminación o a dispositivos que incorporan fuentes de iluminación, un camino claro para maximizar la eficiencia energética pasaría por minimizar las pérdidas de luz en este tipo de sistemas. Además, para obtener la máxima eficiencia de conversión de energía, es esencial optimizar la absorción de luz en los sistemas que realizan una transformación de la luz solar, sin aplicar un voltaje externo, en otras formas de energía, como eléctrica o química.

Para alcanzar el doble objetivo de optimizar la utilización y transformación de la luz, en esta tesis consideramos el estudio de configuraciones ópticas ergódicas, donde los rayos de luz se aleatorizan tras unos pocos rebotes en las interfaces, perdiendo cualquier correlación con el estado incidente externo y dando lugar a un radiación isotrópica en el interior del material. En el Capítulo 2 de la tesis, demostramos que se puede utilizar una geometría ergódica para obtener una emisión de luz polarizada homogéneamente distribuida. En el mismo sistema ergódico, también demostramos que la luz con la polarización no deseada puede atraparse y transformarse de nuevo en electricidad mediante el uso de un par de células solares de perovskita. Tales características son potencialmente útiles para aumentar la eficiencia energética en dispositivos optoelectrónicos que incorporan fuentes de iluminación en ellos, como es el caso de las pantallas de cristal líquido. Una propagación de luz ergódica similar también se considera en el Capítulo 3 para determinar cuál es la captura de luz máxima y la absorción de luz efectiva en un fotoánodo basado en $BiVO_4$ de una celda fotoelectroquímica utilizada para la transformación de luz en hidrógeno. Se considera que los límites en la eficiencia de dicha transformación de energía están fuertemente vinculados a los estados de energía inferior al gap del material, que absorben débilmente la luz. Se explora una nanoestructuración tridimensional del fotoánodo en la celda fotoelectroquímica como un camino para alcanzar eventualmente la ergodicidad para la propagación de la luz en el fotoánodo. En el capítulo final de la tesis, consideramos una construcción en tándem de dos elementos de absorción de luz con perfiles de absorción complementarios, como un fotoánodo de $BiVO_4$ y una celda solar orgánica, para obtener una conversión no asistida por un voltaje externo de luz solar en hidrógeno en celdas fotoelectroquímicas. Se ha descubierto que la implementación de multicapas ópticas diseñadas con el objetivo de optimizar la absorción de luz son un

ingrediente esencial para equilibrar adecuadamente la absorción de luz entre los dos elementos absorbentes de luz en el tándem, lo que lleva a una conversión óptima de energía solar a hidrógeno.

Resum

Per a mitigar l'actual crisi mediambiental, causada per l'ús excessiu de combustibles fòssils i l'alliberament associat de diòxid de carboni a l'atmosfera, és necessari reduir significativament el consum d'energia a escala mundial, confiar més en fonts d'energia netes i renovables, però també maximitzar l'eficiència energètica en les tecnologies actualment existents que utilitzen l'energia. Per assolir aquesta eficiència energètica màxima, és necessari optimitzar la propagació de la llum, la recol·lecció i la utilització en les diferents tecnologies optoelectròniques existents. Atès que una part considerable del consum global d'energia es dedica a la il·luminació o dispositius que incorporen fonts d'il·luminació en ells, un camí clar per maximitzar l'eficiència energètica implicaria minimitzar les pèrdues de llum en aquest tipus de sistemes. A més, per a una eficiència màxima de conversió d'energia, és essencial optimitzar l'absorció de llum en sistemes que realitzen una transformació de la llum solar no assistida en altres formes d'energia, com ara l'electricitat o la química.

Per assolir el doble objectiu d'optimitzar la utilització i transformació de la llum, en aquesta tesi considerem l'estudi de configuracions ergòdiques òptiques, on els raigs de llum són aleatoris després d'uns quants rebots a les interfícies, perdent qualsevol correlació amb l'estat d'incidència extern i donant lloc a una radiació isotròpica dins del material. En el Capítol 2 de la tesi, es demostra que una geometria ergòdica pot ser utilitzada per obtenir una emissió de llum polaritzada distribuïda homogèniament. En el mateix sistema ergòdic, també demostrem que la llum amb la polarització no desitjada pot ser atrapada i transformada de nou en electricitat utilitzant dues cèl·lules solars de perovskita. Aquestes característiques són potencialment útils per augmentar l'eficiència energètica en dispositius optoelectrònics que incorporen fonts d'il·luminació en ells, com és el cas de les pantalles de cristall líquid. Una propagació de llum ergòdica similar també es considera en el Capítol 3 per determinar quina és la màxima captura de llum i l'absorció de llum efectiva en un fotoànode basat en $BiVO_4$ d'una cèl·lula fotoelectroquímica utilitzada per a la transformació de la llum en hidrogen. Els límits en l'eficiència d'aquesta transformació d'energia es veuen fortament vinculats als estats subbanda prohibida de feble absorció de llum. Una nanoestructura tridimensional del fotoànode en la cèl·lula fotoelectroquímica s'explora com un camí per arribar finalment a l'ergodicitat per a la propagació de la llum en el fotoànode. En el capítol final de la tesi, es considera una construcció en tàndem de dos elements d'absorció de llum complementaris, com un fotoànode $BiVO_4$ i una cèl·lula solar orgànica, per obtenir una conversió de la llum solar en hidrogen en cèl·lules fotoelectroquímiques. Es troba que les multicapes òptiques dissenyades per implementar un enfocament invers de resolució de problemes són un ingredient essencial per equilibrar adequadament l'absorció de llum entre aquests dos elements absorbidors en el tàndem, portant a una conversió òptima d'energia solar a hidrogen.

Academic production

List of publications included in this thesis:

- C.G. Ferreira, M. Zhang, C. Ros, and J. Martorell. *Redefining short circuit current density limit of bismuth vanadate photoanodes*. In preparation, tentative title.

- C.G. Ferreira, C. Sansierra, F. Bernal-Texca, M. Zhang, C. Ros, and J. Martorell. *Bias-free solar-to-hydrogen in a BiVO$_4$/PM6:Y6 compact tandem with optically balanced light absorption*. Submitted.

- G. Martínez-Denegri, C.G. Ferreira, M.A. Ruiz-Preciado, P. Fassl, M. Kramarenko, U.W. Paetzold, and J. Martorell. *Wide bandgap perovskite photovoltaic cells for stray light recycling in a system emitting broadband polarized light*. Advanced Energy Materials **12** (2022), 2201473.

- C.G. Ferreira, G. Martínez-Denegri, M. Kramarenko, J. Toudert, and J. Martorell. *Light recycling using perovskite solar cells in a half cylinder photonic plate for an energy efficient broadband polarized light emission*. Advanced Photonics Research **2** (2021), 2100077.

Other publications in peer-reviewed journals:

- M. Kramarenko, C.G. Ferreira, J. Toudert, and J. Martorell. *Photon recycling and antireflection dielectric multilayers for achieving ultimate efficiencies in planar geometry perovskite solar cells*. In preparation, tentative title.

- M. Kramarenko, C.G. Ferreira, G. Martínez-Denegri, C. Sansierra, J. Toudert, and J. Martorell. *Relation between fluorescence quantum yield and open-circuit voltage in complete perovskite solar cells*. Solar RRL **4** (2020), 1900554.

Contributions to international conferences

- C.G. Ferreira, C. Sansierra, F. Bernal-Texca, M. Zhang, C. Ros, and J. Martorell. *Solar-to-hydrogen conversion with an optimally balanced light absorption in a BiVO$_4$/PM6:Y6 compact tandem*. Oral presentation accepted in **PIERS - Photonics and Electromagnetics Research Symposium 2023**.

- G. Martínez-Denegri, C.G. Ferreira, M.A. Ruiz-Preciado, P. Fassl, M. Kramarenko, U.W. Paetzold, and J. Martorell. *A half-cylinder photonic plate for broadband light polarization and light recycling by integrated engineered perovskite photovoltaic cells*. Oral presentation in **OSA Advanced Photonics Congress 2022**.

- C.G. Ferreira, G. Martínez-Denegri, M. Kramarenko, J. Toudert, and J. Martorell. *Half cylinder photonic plate with broadband polarized light emission incorporating light recycling to electricity using perovskite solar cells*. Oral presentation in **OSA Advanced Photonics Congress 2021**.

Contents

List of Figures

List of Tables

List of acronyms

3-D Three-dimensional

BVO Bismuth vanadate

EQE External quantum efficiency

FE Faradaic efficiency

FF Fill factor

FTO Fluorine-doped tin oxide

h-CPP Half-cylinder photonic plate

HER Hydrogen evolution reaction

ITO Indium tin oxide

LCD Liquid crystal display

LED Light-emitting diode

ML Multilayer

MRP Multilayer reflective polarizer

OER Oxygen evolution reaction

OPV Organic photovoltaic

PCE Power conversion efficiency

PEC Photoelectrochemical

PV Photovoltaic

PVK Perovskite

RHE Reversible hydrogen electrode

SEM Scanning electron microscope

STH Solar-to-hydrogen

List of selected symbols

α Absorption coefficient

E_g Bandgap energy

$J\text{-}V$ Current density - voltage

$J_\mathrm{bias-free}$ Bias-free current density

J_sc Short circuit current density

k Wave vector

n Refractive index

R_s Series resistance

R_sh Shunt resistance

V_oc Open circuit voltage

Introduction

1.1 Current energy status

The rapid growth of the world's population, the development of industries, the improvement in living standards, and the massive transportation of people and goods are leading to a practically continuous increase in global energy consumption, which in 2021 achieved a new record.[1–3]

As seen in Figure 1.1 a), a significant fraction of this energy, more precisely 82%, is obtained through the burning of fossil fuels, such as coal, oil, and natural gas. The extensive use of these energy sources does not constitute a sustainable path to meet the global energy demands owing to the limited availability of fossil fuels but mainly due to the large emissions of greenhouse gases, such as carbon dioxide (CO_2), associated with their use.[3,4,6] As seen in Figure 1.1 b), the amount of CO_2 released to the atmosphere from fossil fuels' burning keeps increasing over the years and it already represents three-quarters of the total CO_2 emissions.[2,4] This poses a serious threat to the planet since it directly contributes to a climate emergency. As seen in Figure 1.1 c), the global surface temperature has been continuously raising during the last decades, being the past nine years the warmest ever recorded. We are, therefore, facing a very alarming scenario with possibly disastrous environmental consequences, which include more frequent and severe extreme climate events, such as heatwaves, heavy rainfall or droughts, or the retreat of glaciers with subsequent raise of the sea level, which can induce major changes in the ecosystems and lead to the extinction of several species.[5,7]

To mitigate such environmental crisis, global energy consumption should largely rely on clean and renewable energy sources, such as solar, wind, or hydrothermal, while energy waste must be reduced to a minimum. Provided that a significant fraction of the world's present energy consumption goes into illumination sources or devices that incorporate illumination sources in them,[8,9] it becomes essential to make an appropriate use of the light to minimize losses in the currently available devices. In addition, optimal light absorption must be targeted in systems that transform sunlight into other forms of energy to achieve maximum conversion efficiency. Therefore, the design of energy-efficient systems capable of mitigating light losses and maximizing light harvesting and conversion is crucial to make a more sustainable use of the energy resources.
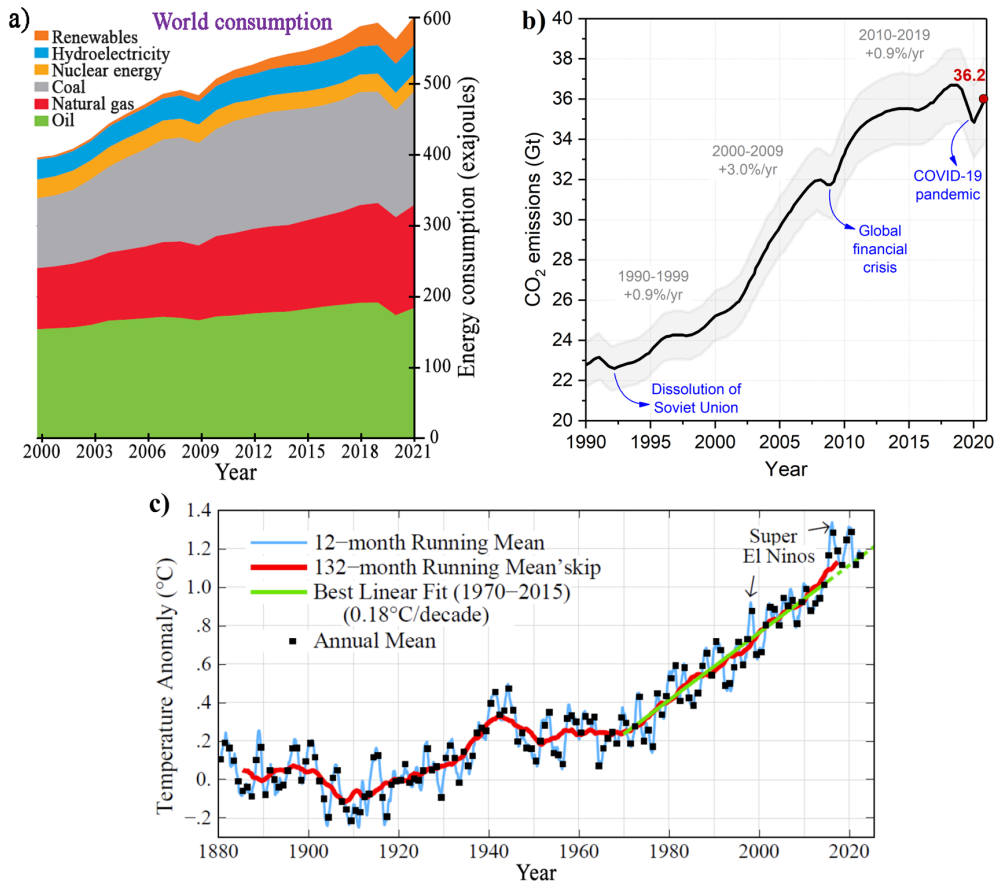
Figure 1.1: a) Total world energy consumption during the last two decades, by source type. Adapted from Reference 1. b) Total CO_2 emitted from the burning of fossil fuels between 1990 and 2021. Adapted from Reference 4. c) Global surface temperature variation relative to the average of the period 1880-1920. From Reference 5.

1.2 Route to optimize light absorption and utilization

1.2.1 Minimize light losses

Currently, energy efficiency in illumination sources or in most of the optoelectronic technologies integrating illumination sources is far from optimal, provided they either suffer from a poor light usage or from significant light losses. In particular, in some devices incorporating a liquid crystal display (LCD), such as smartphones, computers, and televisions, more than 90% of the light emitted by the source ends up being lost in the different optical components of the display.[10–12] The use of absorbing polarizers to provide the linearly polarized illumination needed for the image formation is the main responsible for this waste of energy, accounting for at least 50% of light loss.[8,13–15] Cur-

rent strategies to reduce such a light waste involve the incorporation of a dual brightness enhancement film,[13,16,17] composed of hundreds of nanolayers alternating isotropic and birefringent polymers, or the integration of a conversion element, such as a prism film or a diffuser plate,[17–19] which can convert the polarization of the light into the desired one but require the use of more complex lithography techniques and have limited efficiency.

An alternative approach is to use a luminescent solar concentrator[20–24] that relies on fluorescent organic dyes[25–27] or quantum dots[28,29] to selectively absorb light with a given polarization and re-emit it at a longer wavelength via photoluminescence. This re-emitted light is then guided towards the edges of the luminescent solar concentrator, where small-area photovoltaic (PV) cells are incorporated for the conversion of the light photons into an electric current. Although this is a very promising configuration for the reduction of optical losses, by avoiding parasitic absorption and reusing the light with unwanted polarization, its application to LCDs requires the fluorescent materials to emit into the deep red and near-infrared spectral region, to make full use of the incident light and to avoid a potential corruption of the image.[30] This resulted in very low power conversion efficiencies for the devices experimentally tested.[31,32]

To overcome such an issue, in the present thesis, we will depart from this latter approach to design an optically efficient guiding structure capable of transmitting diffuse and polarized light by combining an ergodic geometry, described in detail in Section 1.4.1, with a multilayer reflective polarizer. As we will demonstrate, the discarded polarization component will be trapped very effectively inside this guiding structure and guided to the edges where small-area PV cells are incorporated, as in the design of the luminescent solar concentrator. To achieve maximal conversion efficiency for the recycling of this stray light, perovskite (PVK) solar cells will be used as the conversion element. This kind of PV cell exhibits the ideal characteristics to effectively recycle light in optoelectronic devices illuminated by visible light sources, which include a broad bandgap tunability,[33–37] low open-circuit voltage (V_{oc}) losses[38–41] and efficient photon to collected electron-hole pair conversion.[42]

Therefore, by combining ergodicity, light trapping, and an efficient recycling of the unused light back into electricity we will be able to propose an efficient design to significantly reduce energy losses in the currently available LCDs.

1.2.2 Enhance light absorption

In a system that, instead of using light for illumination, transform it into another form of energy, a better utilization of such light energy is also needed to enhance the efficiency of the different energy transformation processes. In particular, this thesis will focus on devices capable of converting solar energy into two usable forms of energy, such as electrical or chemical energy. While the first kind of energy conversion is achieved by the use of PV cells, the last requires the utilization of photoelectrochemical (PEC) devices. The operation principles associated with each one of these technologies can be

found in Section 1.3. For both cases, the conversion efficiency is strongly linked to the light absorption capability, so the design of energy-efficient devices demands optimal harvesting of the incident sunlight photons. This is a challenging task, especially in thin-film PV and PEC technologies, that require the use of very thin absorbing layers to ensure proper separation and extraction of the charge carriers while avoiding recombination. Hence, advanced optical techniques must be employed to maximize light absorption and conversion in this sort of devices, as discussed in Section 1.4.2.

This kind of techniques has been widely employed to enhance light harvesting in PV cells,[43–51] but fewer studies were dedicated to optically increasing the performance of PEC devices by tailoring light propagation and absorption.[52–60] The current thesis focuses on the design of energy-efficient photoanodes for the water-splitting reaction, with optimal light distribution and maximal absorption. In particular, bismuth vanadate ($BiVO_4$ (or BVO)) is considered as the semiconductor photoanode material, since it presents a relatively narrow bandgap, in addition to being earth-abundant, non-toxic, and highly stable in neutral and basic electrolytes.[57, 61–63] However, such kind of photoanodes are not capable of performing spontaneous gas evolution, without the need for an external voltage source, given that the conduction band of the BVO is located slightly below the thermodynamic potential for water reduction.[57, 64, 65] To tackle this issue, tandem architectures in which the photoanode is connected to a photovoltaic cell that provides enough voltage to accomplish bias-free water splitting have been studied. To date, relatively high solar-to-hydrogen conversion efficiencies have been achieved in systems where the BVO-based photoanode was nanostructured to enhance light absorption.[57, 58, 60] However, the high light scattering losses in the BVO, mostly caused by the nano-structuration, prevent the implementation of an ideal compact tandem structure and require more complicated designs.

Therefore, after a first study on the limit absorption and photocurrent generation of BVO photoanodes when in the presence of an optimal light trapping, we focus on the design of an optimal compact tandem PEC cell for unassisted water splitting, based on transparent BVO photoanodes. To reach maximal bias-free solar-to-hydrogen (STH) conversion efficiency, we will combine such transparent photoanodes with an organic photovoltaic (OPV) cell that has a complementary absorption profile to the one of the BVO. In addition, we will integrate a multilayer structure, properly optimized to ensure a perfect balance of the light among the absorbing elements and a maximum absorption in the BVO photoanode. Hence, we will demonstrate that optimal light harvesting and distribution is key to maximizing the conversion efficiency for different BVO-based devices.

1.3   Devices for light energy transformation

Common to all the designs proposed in this thesis is the incorporation of devices for the transformation of light energy into another usable form of energy. Indeed, all the devices proposed either incorporate PV cells for the conversion of light photons into

an electrical current, and/or PEC cells for the production of a solar fuel, such as hydrogen. The operating principles of both technologies share some common points and are described below.

1.3.1 Operating principles of photovoltaic cells

Photovoltaic cells are devices that rely on the photovoltaic effect to convert light into electricity, as schematically shown in Figure 1.2. When a photon reaches the semiconductor active layer of a PV cell with an energy $h\upsilon$ superior to its bandgap E_g, it is absorbed in the material and generates an electron-hole pair (1). Such photocarriers are intended to diffuse through the semiconductor until they encounter an energy barrier that may separate charges of opposite sign (2). This energy barrier can be formed by the junction between two semiconductors selectively doped with electrons (n-type) and with holes (p-type), as in the case of the p-n junction solar cells, or it can be created by the inclusion in both sides of the semiconductor material of two additional layers capable of blocking the transport of electrons or holes, as occurs for the p-i-n or n-i-p devices. When connecting an external load, the charge carriers are extracted from the solar cell and an electric current is generated (3).[66,67]
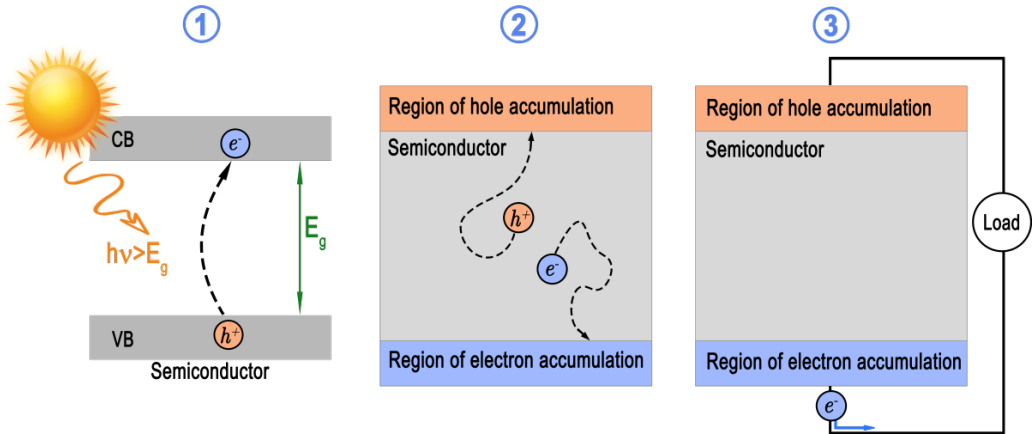
Figure 1.2: Illustrative scheme of the working mechanism of a PV cell. VB and CB stand for the semiconductor valence and conduction bands, respectively.

A typical current density - voltage (J-V) curve obtained from a PV cell is shown in Figure 1.3 a). The main electrical parameters characterizing the solar cell performance, such as the short-circuit current density (J_{sc}), the open circuit voltage, the fill factor (FF) and the power conversion efficiency (PCE), can be extracted from these curves.

In particular, the J_{sc} is the current per unit area that flows through the cell when this is short-circuited, i.e. when $V = 0$. The J_{sc} is proportional to the photon absorption in the active layer of the PV cell, A_{AL}, to the photon-to-current conversion efficiency, η_A,
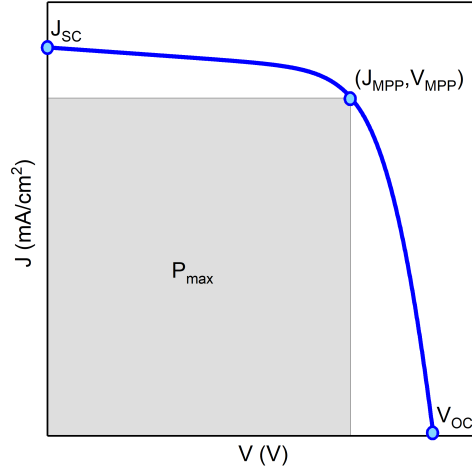
Figure 1.3: Illustrative example of a *J-V* curve obtained for a solar cell under light irradiation, with the main PV electrical parameters indicated.

and to the incident photon flux, Φ.

$$J_{sc} = q \int \Phi(\lambda) A_{AL}(\lambda) \, \eta_A \, d\lambda = q \int \Phi(\lambda) EQE(\lambda) \, d\lambda, \tag{1.1}$$

In the previous equation, the wavelength-dependent external quantum efficiency (EQE) corresponds to the ratio between the collected photo-generated carriers and the number of incident photons.

The V_{oc} is the voltage measured when no current flows through the external circuit, so $J = 0$. For cells presenting an ideal diode behavior, this voltage is dependent on the J_{sc} and on the radiative (J_{rad}) and non-radiative ($J_{non-rad}$) recombination dark currents, according to the Shockley-Queisser model:[39,68,69]

$$V_{oc} \approx \frac{k_B T}{q} \ln\left(\frac{J_{sc}}{J_{rad} + J_{non-rad}}\right) = \frac{k_B T}{q} \ln\left(\frac{J_{sc}}{J_{rad}}\right) + \frac{k_B T}{q} \ln(QY), \tag{1.2}$$

where QY is the cell's external fluorescence quantum yield, corresponding to the ratio between the number of photons re-emitted by the active layer or escaping the cell and the number of incident photons absorbed at the active layer. In the absence of non-radiative photogenerated carrier recombination, QY = 100%, the last term of equation (1.2) vanishes and the V_{oc} of the cell is maximum. In this case, the PV cell is operating at the radiative limit and its open circuit voltage $V_{oc,rad}$ is given by

$$V_{\text{oc,rad}} = \frac{k_{\text{B}}T}{q} \ln\left(\frac{J_{\text{sc}}}{q \iint A_{\text{AL}}(\lambda, \theta) \, \text{BB}(\lambda) \, d\theta \, d\lambda}\right), \tag{1.3}$$

where $\text{BB}(\lambda)$ is the blackbody radiation spectrum of the solar cell and θ it the angle of photon emission .

The FF, on the other hand, is defined as the ratio between the maximum power delivered by the PV cell (P_{max}), which is the power measured at the maximum power point (MPP), and the product of V_{oc} and J_{sc}. It characterizes how "rectangular" the J-V curve is and is affected by the electrical non-idealities of the device

$$\text{FF} = \frac{P_{\text{max}}}{J_{\text{sc}} \, V_{\text{oc}}} = \frac{J_{\text{MPP}} \, V_{\text{MPP}}}{J_{\text{sc}} \, V_{\text{oc}}}. \tag{1.4}$$

Finally, the PCE is the typical indicator for benchmarking the performance of solar cells and corresponds to the ratio between the maximum generated power and the incident sunlight power, which is $100 \ \text{mW/cm}^2$ for standard AM1.5G illumination, and can be written as a function of the measurable parameters of the J-V curve as

$$\text{PCE} = \frac{P_{\text{max}}}{P_{\text{sunlight}}} = \frac{J_{\text{sc}} \, V_{\text{oc}} \, \text{FF}}{P_{\text{sunlight}}}. \tag{1.5}$$

The efficiency of a PV cell can be increased, for instance, by using semiconductor materials with improved absorption above the bandgap, or by eliminating non-radiative recombination losses and electrical non-idealities in the device.

1.3.2 Operating principles of PEC cells for water splitting

Photoelectrochemical water splitting is a process that uses sunlight to generate molecular hydrogen and oxygen from water, through the reaction:

$$2\text{H}_2\text{O} \rightarrow 2\text{H}_2 + \text{O}_2 \tag{1.6}$$

It has gained increased attention in recent years as a means to store solar energy in chemical bonds since the hydrogen produced in this reaction can be stored and later used as a solar fuel.

The basic mechanism of PEC water splitting is illustrated in Figure 1.4. Similar to what happens in PV cells, this process is initiated by the absorption of a photon and by the creation of an electron-hole pair in a semiconductor material that acts as photoelectrode, provided the energy of such photon is higher than the bandgap of the semiconductor (1). These charge carriers are then separated, and if they do not suffer recombination, they are driven to the surface of the respective electrode (2) to perform the corresponding
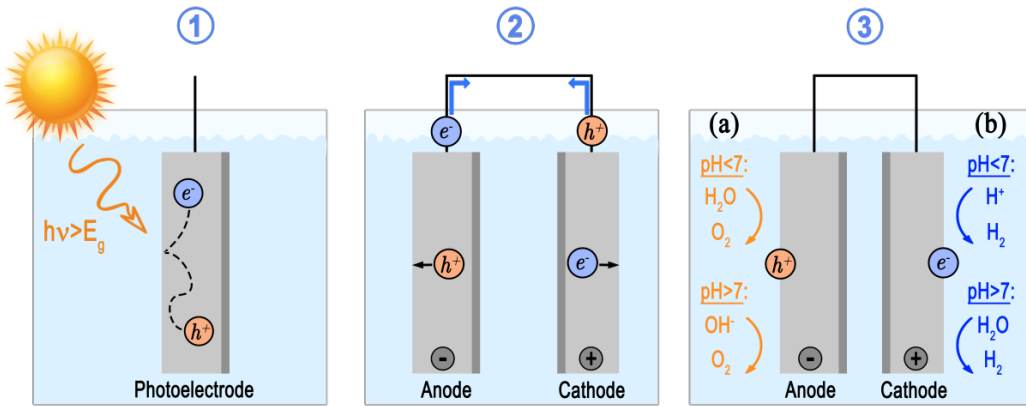
Figure 1.4: Illustrative scheme of the working mechanism of a PEC system for water splitting.

water splitting half-reaction. In particular, holes migrate to the surface of the anode and participate in the oxygen evolution reaction (OER) (3a), described by

$$2H_2O + 4h^+ \rightarrow O_2 + 4H^+ \tag{1.7}$$

if the medium is acidic, or by

$$4OH^- + 4h^+ \rightarrow O_2 + 2H_2O \tag{1.8}$$

if the medium is alkaline.

On the contrary, electrons are driven to the surface of the cathode to perform the hydrogen evolution reaction (HER) (3b), given by

$$2H^+ + 2e^- \rightarrow H_2 \tag{1.9}$$

or by

$$2H_2O + 2e^- \rightarrow H_2 + 2OH^- \tag{1.10}$$
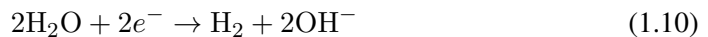
for acid and alkaline media, respectively.[70,71]

At standard temperature (298 K), pressure (1 atm) and ionic concentration (1 molar) the overall water splitting reaction has a Gibbs free energy of $+237$ kJ per mol of produced H_2, which means that to overcome the thermodynamic threshold for the reaction, each electron must be given a potential energy equivalent to 1.23 eV.[72–74] In other words, at standard conditions, spontaneous water splitting requires a potential difference between cathode and anode of at least 1.23 V. However, higher voltages are needed to overcome the various losses and inefficiencies in the PEC systems.[71,75–77]
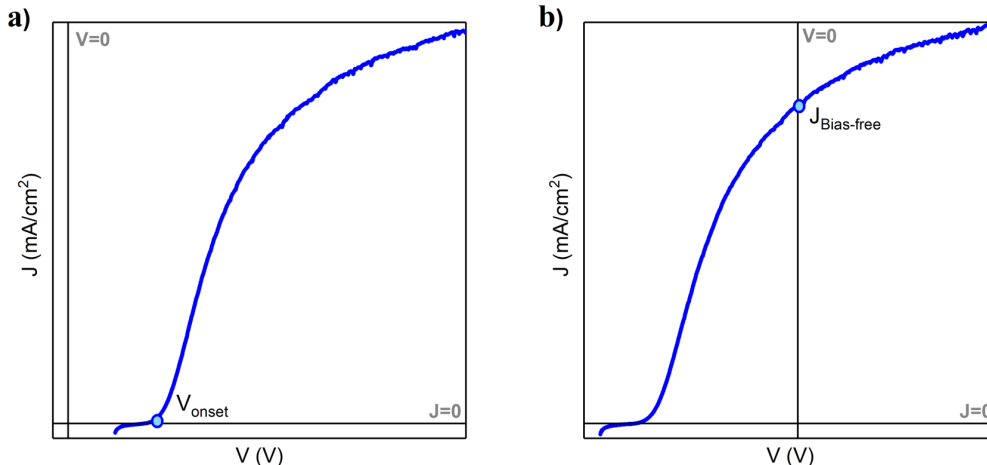
Figure 1.5: Comparison between a) a case where the PEC system is not capable of spontaneously performing the reaction and b) an example where spontaneous water splitting occurs in the presence of sunlight, generating a current density $J_{\mathrm{bias-free}}$.

Representative examples of J-V curves obtained for PEC devices under illumination can be seen in Figure 1.5 and provide important information about the water splitting capability of a given system. For instance, in the case of curve (a) the PEC cell cannot perform the water splitting reaction powered solely from sunlight irradiation and a voltage equal to or higher than the onset potential V_{onset} must be provided by an external bias source. In contrast, for curve (b) the onset potential is negative and a current $J_{\mathrm{bias-free}}$ is generated when no voltage is applied to the system, which means that the PEC system is capable of performing unassisted water splitting in the presence of sunlight. The magnitude of this photocurrent is related to the rate of the water splitting reaction and to the production of hydrogen and oxygen, and is key to determine the efficiency of the PEC water-splitting process. Such efficiency is typically described by the STH conversion efficiency under zero-bias conditions, which corresponds to the ratio between the rate of hydrogen production and the incident sunlight power, and is calculated as follows[71,78,79]

$$\mathrm{STH} = \frac{J_{\mathrm{bias-free}} \times 1.23 \times \mathrm{FE}}{P_{\mathrm{sunlight}}}, \tag{1.11}$$

where FE is the faradaic efficiency, defined as the ratio between the experimentally measured amount of hydrogen produced and the theoretical one estimated from Faraday's law.[80,81]

1.3.3   Power conversion using different light sources

The power conversion efficiency of the PV and PEC devices is strongly linked to the spectral distribution and intensity of the light source used. This is particularly evident in equation (1.1), which relates the J_{sc} to the wavelength-dependent incident photon flux, $\Phi(\lambda)$.

When the light source is the sun, the incident photon flux for sunlight irradiation on the surface of the Earth is standardized to the AM1.5G spectrum of Figure 1.6. In this case, the maximum power conversion efficiency achievable for planar configuration single-junction PV cells can be determined from the Shockley-Queisser detailed balance theory.[69, 82] For PEC systems where the light source is also the sun, more complicated models have been developed to account for the different kinds of losses, that include non-radiative recombination, non-idealities in charge transport, or imperfect catalyst kinetics, in various configurations comprising a different number of absorbing materials.[75, 83–85]
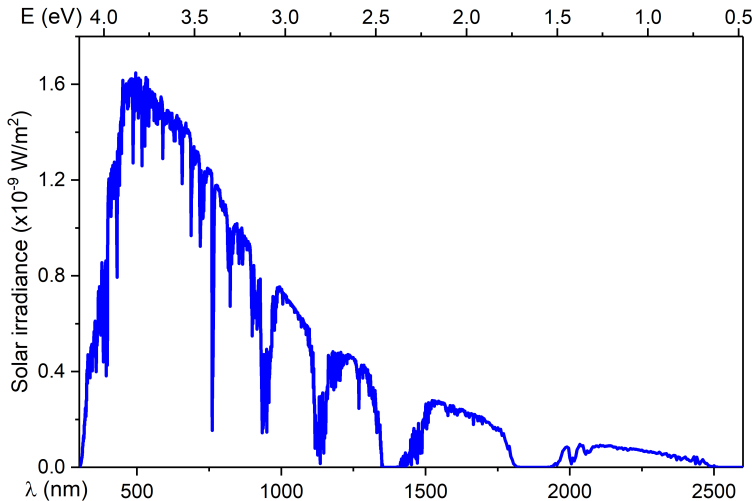
Figure 1.6: AM1.5G spectrum of the solar irradiance that reaches the surface of the Earth as a function of light energy E (top axis) and wavelength λ (bottom axis).

On the other hand, when using a monochromatic light source, such as a laser or a diode, to illuminate the PV or PEC devices, the PCE limits set for sunlight irradiation can be largely surpassed. Indeed, when the bandgap of the semiconductor materials used is well matched with the energy of the incident photons, the thermalization losses are minimized and the conversion efficiency can be boosted.[86–89]

Therefore, as it will be discussed in subsequent chapters, the choice of the absorbing materials to be employed as active layers for the PV or PEC systems must always take into consideration the profile of the incident light source, to achieve maximal energy-efficiency for any given kind of systems.

1.4 Optimal light propagation for energy-efficient devices

As previously mentioned in the beginning of this introductory chapter, the pursuit for energy efficient devices entails the optimization of light absorption and utilization. To achieve such a goal requires the control and manipulation of the light propagation inside the different materials, as well as the utilization of advanced structures tailored to reduce light losses or to enhance energy conversion efficiency. A promising route to design such structures involves taking advantage of ergodicity to allow light waves to explore and interact with different regions of the material in a statistically representative manner. Alternative approaches include the use of photonic configurations capable of optimally distributing the light inside the devices and trapping it in their active layers to promote enhanced light absorption and conversion.

1.4.1 Ergodic propagation of light

In ergodic geometries, light rays are randomized after a few bounces at the interfaces, losing any correlation with the external incident state, and giving rise to an isotropic radiation inside the material, as illustrated in Figure 1.7. The use of such geometries is key to achieve maximal light trapping and an effective light absorption, as demonstrated in a landmark work published by Yablonovitch.[90,91] On the other hand, the randomization of the light rays and the isotropic light propagation promoted by such ergodicity may also play a crucial role in different devices that require, for instance, the emission of diffuse and homogeneously distributed light.

a) Non-ergodic geometry **b)** Ergodic geometry
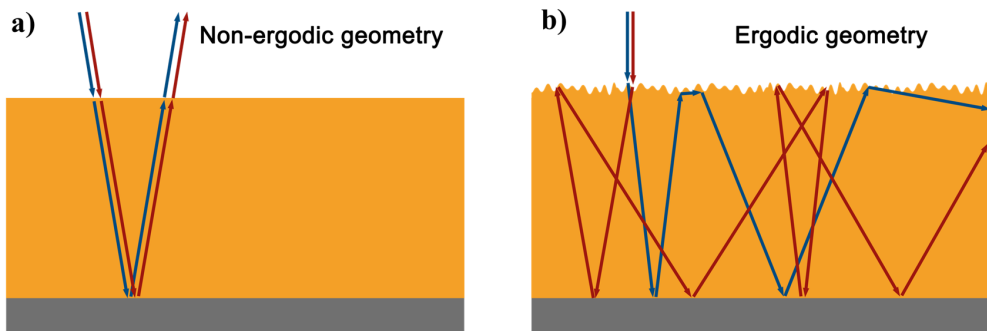
Figure 1.7: Examples of a) non-ergodic and b) ergodic geometries, comparing the trajectories of two different light rays propagating inside each of the geometries.

To achieve such an ergodicity in light propagation, random surface texturing of one or more interfaces of the material[90–92] is typically required. Nevertheless, works involving incorporation of ordered or periodic structures such as micro-lenses,[93–95] micro-

prisms,[96,97] micro-domes,[46,98] lenslet arrays,[99,100] optical fibers,[101,102] or a half-cylinder photonic plate (h-CPP)[103] in the front interface of thin-film solar cells have demonstrated increased light trapping and absorption in the active layer made of a semiconductor material.

However, only in reference 103, which considered a half-cylinder photonic plate composed of a periodic array of interconnected half-cylinders placed on top of a glass substrate, the ergodicity was rigorously demonstrated. To study the effect that ergodicity would have in light propagation and absorption, a highly reflective mirror was placed on the opposite side of the glass, assuming the light was entering from the curved surface of the photonic plate, as illustrated in Figure 1.8 a). As clearly seen in such a figure, the trajectories of the rays are strongly affected by the incident angle and position where the incoming ray enters the h-CPP. A cumulative distribution function between two consecutive reflections of the same ray, $\Delta\beta$, is shown in Figure 1.8 b), independent on the input ray parameters. This result proves the ergodicity in ray propagation relative to the geometrical redistribution of the ray trajectories inside the h-CPP, meaning that any region of the phase space of the ray trajectories can be visited regardless of the ray input parameters.
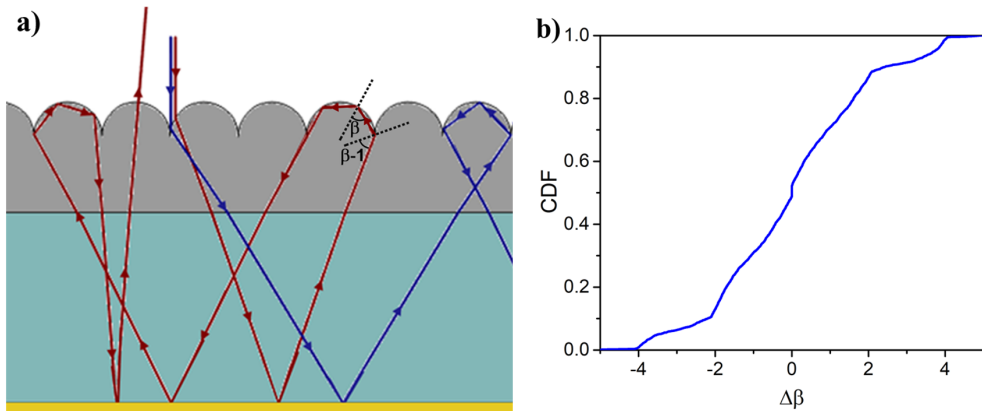
Figure 1.8: a) Simulated ray trajectories for two light rays entering the h-CPP at different points (not at scale). b) Cumulative distribution function of $\Delta\beta$, computed over a series of ray segments. Figures are taken from Reference 103.

The use of these ergodic geometries is of great importance in the design of energy-efficient devices with high energy conversion efficiency and reduced losses. Such geometries may act as a mechanism to efficiently disperse light and transmit it in a homogeneous manner, or they may be employed to reach the limits of light absorption, as will be discussed in the following section.

1.4.2 Light absorption limit

The ability of a material to absorb energy is described by its wavelength-dependent absorption coefficient, α. In principle, a maximal light absorption, A, can be achieved for infinitely thick materials with $\alpha > 0$, as the absorption scales with the thickness of the material, d, according to the expression

$$A = 1 - e^{-\alpha d}, \tag{1.12}$$

that is valid when d is much larger than the wavelength of the incident light.

However, thickening the materials is not always a feasible route. For many thin-film PV and PEC technologies, the thickness of the absorbing layer is limited by other thickness-dependent parameters, such as the exciton diffusion length, responsible for an efficient charge extraction. For this reason, different approaches targeting the increase of the effective light path inside thin absorbing layers, by either exploiting wave interference or trapping of the light by geometrical structures, have attracted significant attention in the field of photovoltaics and to a lower degree in the field of photoelectrochemistry.

A theoretical upper limit for light absorption due to light trapping in a material with refractive index n and finite thickness d, larger than the wavelength of the incident light, was set by Yablonovitch.[90,91] The model developed adopted a statistical ray optics approach, by assuming an ergodic propagation of the light inside a textured absorbing layer for which $\alpha d \ll 1$. To determine the limit absorption in such a layer, the principle of the detailed balance was employed in a configuration incorporating a perfect reflector on the back, where the losses at the boundaries were neglected. As a result, a maximum enhancement in light absorption of $4n^2$ was estimated to be achievable by means of ray optics light trapping.

This limit set by Yablonovitch is a benchmark parameter to evaluate the light absorption capability of different material designs. For this reason, several works were dedicated to the search of optimal structures that could approach such a limit, either by considering periodic[104–114] or random[115–117] texturing of the material interfaces. In some cases, that considered thin materials operating under the wave optics regime,[106,107,115,118,119] highly absorptive materials,[109] or scattering features smaller than the wavelength of the light,[105,120,121] for which the assumptions made by Yablonovitch are no longer valid, some resonances were obtained for very specific angle-wavelength combinations, for which this $4n^2$ limit was slightly surpassed. However, when averaging the absorption enhancement over the whole angular and wavelength space, the results always ended up falling under the ray optics limit.

1.4.3 Light propagation at different length scales

In the present thesis the focus is on the design and optimization of highly energy-efficient devices, targeting maximal light harvesting and utilization, with reduced losses.

As outlined in the two preceding sections it is of utmost relevance the search for geometries capable of promoting an ergodic propagation of the light rays and/or that may eventually lead to the absorption limit of the light for a broadband wavelength range. Indeed, we will demonstrate that some of the strategies presented in the two preceding sections allow for tailoring the light transmission and propagation, as well as the maximization of light absorption in configurations involving structures that are considerably larger than the wavelength of the incident light and therefore operate under the ray optics regime.

We will also consider what the efficiency limit is and how to enhance light absorption in energy-harvesting systems, such as thin-film PV or PEC cells, which require the use of very thin absorbing materials, close to the wavelength of the incoming light, for which the geometrical optics approach is no longer valid. In those cases, it will be necessary to consider a wave optics model for the propagation of the light, to include the interference effects between the forward and backward propagating waves. In the next section, we will present in great detail the tools necessary to model and optimize light propagation and absorption in such thin-layer structures. As it will be seen in the next chapters, a proper design of such thin configurations allows for significant enhancements in light absorption and conversion in different energy transformation systems.

1.5 Modeling energy-efficient devices

In the previous sections, we discussed a ray optics approach to describe light propagation in materials that are substantially thicker than the wavelength of the incoming radiation and established a limit for light absorption in that regime. Conversely, in the current section we explore propagation of light in thin-layered materials, which must be described by a full-wave propagation model. On the basis of such wave propagation lie the Maxwell equations that describe the behavior of the electric ($\mathbf{E}$) and magnetic fields ($\mathbf{B}$) and their interactions with matter.

$$
\begin{array}{llll}
(i) & \nabla \cdot \mathbf{E}(\mathbf{r}, t) = \dfrac{\rho}{\varepsilon_0} & (iii) & \nabla \times \mathbf{E}(\mathbf{r}, t) = -\dfrac{\partial \mathbf{B}(\mathbf{r}, t)}{\partial t} \\[4mm]
(ii) & \nabla \cdot \mathbf{B}(\mathbf{r}, t) = 0 & (iv) & \nabla \times \mathbf{B}(\mathbf{r}, t) = \mu_0 \mathbf{J} + \mu_0 \varepsilon_0 \dfrac{\partial \mathbf{E}(\mathbf{r}, t)}{\partial t}
\end{array}
\tag{1.13}
$$

where $\mathbf{r}$ is the spatial position, t the time, $\mathbf{J}$ the electric current density, ρ the charge density, ε the permittivity (or dielectric function), and μ the permeability of the medium.

The electromagnetic wave equations, describing the propagation of light, can be determined from equation (1.13). For the particular case of a homogeneous medium, a general solution is a plane wave, given by

$$
\mathbf{E}(\mathbf{r}, t) = E_0 \, e^{i(\mathbf{k} \cdot \mathbf{r} - \omega t)} \, \hat{\mathbf{e}},
\tag{1.14}
$$

where E_0 is the amplitude of the field, $\hat{e}$ is the polarization unit vector of the field, ω the angular frequency and $\mathbf{k} = \omega \mathbf{v}$ the wave vector, with $\mathbf{v}$ corresponding to the speed of the light in the medium. In addition, the electric and magnetic fields in this case are orthogonal and their amplitudes are related by

$$B_0 = v \, E_0. \tag{1.15}$$

These solutions for the electromagnetic fields provide insights into the characteristics of the light waves as they propagate through different media. In the following section, we will depart from such solutions to describe the behavior of light when it interacts with layered structures.

1.5.1 General transfer matrix method

For multilayer structures that are composed of homogeneous and isotropic layers with thicknesses of the order of the wavelength of the incident light, separated by interfaces that are optically flat and all parallel to one another, the electromagnetic wave propagation can be determined by solving the Maxwell equations (1.13) in one-dimension and by employing a transfer-matrix approach to take into account interference effects due to the coherence of the light.[122–124]

When light propagating in a medium j reaches the interface separating it from medium k, it will be partially transmitted and partially reflected. The amplitudes of transmission and reflection at the interface are described by the Fresnel coefficients, which are obtained by setting the appropriate boundary conditions for the electric and magnetic fields at the interface, and depend on the angle of incidence, θ_i, complex refractive indexes of both media, n_j and n_k, and polarization of the light.
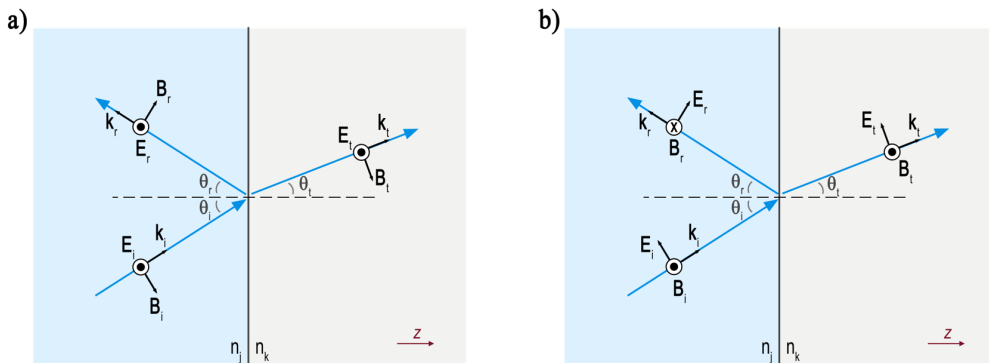
Figure 1.9: Changes in electric field $\mathbf{E}$, magnetic field $\mathbf{B}$ and wave vector $\mathbf{k}$ at the interface between an incident medium j with refractive index n_j and a final medium k with index n_k, for a) s- and b) p-polarized light. The subscripts i, r and t refer to the incident, reflected and transmitted components, respectively.

In the case of s-polarized (or transverse electric) light, the electric field is parallel to the plane of the interface, as illustrated in Figure 1.9 a), and the Fresnel coefficients for the reflection, $r_{j,k}^{(s)}$, and transmission, $t_{j,k}^{(s)}$, are given by

$$r_{j,k}^{(s)} = \frac{n_j k_j - n_k k_k}{n_j k_j + n_k k_k} \qquad t_{j,k}^{(s)} = \frac{2\,n_j k_j}{n_j k_j + n_k k_k}\,, \qquad (1.16)$$

while for p-polarized (or transverse magnetic) light the magnetic field is parallel to the surface separating the two media, as shown in Figure 1.9 b), and the Fresnel coefficients are written as

$$r_{j,k}^{(p)} = \frac{n_j k_k - n_k k_j}{n_j k_k + n_k k_j} \qquad t_{j,k}^{(p)} = \frac{2\,n_j k_j}{n_j k_k + n_k k_j}\,, \qquad (1.17)$$

where the complex wave vector in the medium j, k_j, depends on the angle of incidence, refractive indexes of both media and wave vector in the vacuum, $k_0 = 2\pi/\lambda$.

The electric field at the incident medium, E_j, can be related to the one of medium k through the so-called interface matrix $I_{j,k}$, which takes into account the previously defined Fresnel coefficients such that, for each polarization component

$$\begin{bmatrix} E_{j_R}^+ \\ E_{j_R}^- \end{bmatrix} = I_{jk} \begin{bmatrix} E_{k_L}^+ \\ E_{k_L}^- \end{bmatrix}; \quad I_{j,k} = \frac{1}{t_{j,k}} \begin{bmatrix} 1 & r_{j,k} \\ r_{j,k} & 1 \end{bmatrix}. \qquad (1.18)$$

In this case, we are considering that layer j is on the left side of layer k, as illustrated in Figure 1.9, so the electric field E_{j_R} is the one on the right boundary of layer j, just before the interface, while E_{k_L} is the field on the left boundary of layer k, right after the interface. The plus and minus signs indicate the direction of propagation of the field ($+$ means from left to right, while $-$ indicates from right to left).

In addition, the electric field also varies alongside a given layer j. To relate the field at the left and right interfaces of this layer, a propagation matrix P_j should be used

$$\begin{bmatrix} E_{j_L}^+ \\ E_{j_L}^- \end{bmatrix} = P_j \begin{bmatrix} E_{j_R}^+ \\ E_{j_R}^- \end{bmatrix}; \quad P_j = \begin{bmatrix} e^{-ik_{jz}d_j} & 0 \\ 0 & e^{ik_{jz}d_j} \end{bmatrix}, \qquad (1.19)$$

where d_j is the thickness of the layer j and z is the direction perpendicular to the layer interfaces, as indicated by the axis system.

This matrix formalism describing the changes in electric field across a boundary or alongside a given layer can be directly extended to a multilayer structure with f-1 thin layers (where f is a finite number), enclosed between an incident and a final medium, as the one represented in Figure 1.10. In this case, a total system matrix $S_{0,f}$ that describes the whole stack can be obtained simply by multiplying all the individual interface and propagations matrices such that, for each polarization
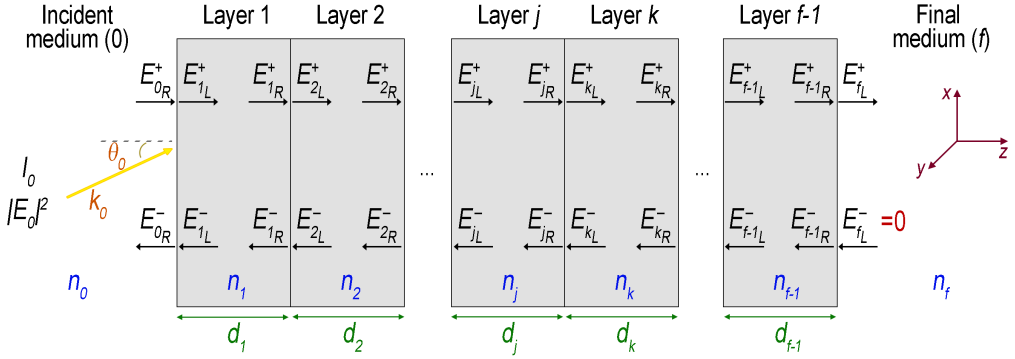
Figure 1.10: Multilayer stack with f-1 thin layers parallel to each other, enclosed between an incident and a final medium, and with light impinging from the left side, as considered for the transfer matrix calculations. The different refractive indexes and electric field components at each layer are also represented, following the same nomenclature used throughout this work.

$$\begin{bmatrix} E_{0_R}^+ \\ E_{0_R}^- \end{bmatrix} = S_{0,f} \begin{bmatrix} E_{f_L}^+ \\ E_{f_L}^- \end{bmatrix} ; \quad S_{0,f} = \left(\prod_{j=1}^{f\text{-}1} I_{j\text{-}1,j} P_j \right) I_{f\text{-}1,f}. \tag{1.20}$$

Since this total matrix relates the electric field in the incident medium with the one in the final medium, it allows for a direct calculation of the total reflectance, R, and transmittance, T, of the thin multilayer system. When no light is incident from the final medium ($E_{f_L}^- = 0$), they are simply given by

$$R = |r_{0,f}|^2 ; \quad r_{0,f} = \frac{E_{0_R}^-}{E_{0_R}^+} = \frac{S_{0,f}(2,1)}{S_{0,f}(1,1)}; \tag{1.21}$$

$$T = \frac{k_f}{k_0} |t_{0,f}|^2 ; \quad t_{0,f} = \frac{E_{f_L}^+}{E_{0_R}^+} = \frac{1}{S_{0,f}(1,1)}. \tag{1.22}$$

On the other hand, similar matrices can be written for the partial subsystems comprising all the layers between the incident medium and the left boundary of a given layer j, S_{0,j_L}, as well as the one containing all the layers between this interface and the final medium, $S_{j_L,f}$. The use of these partial matrices allows us to determine the transmission coefficients t_{0,j_L}^+ and t_{0,j_L}^-, between the incident medium and any layer j, from which we can get the electric field in the direction of propagation z, at any point of the multilayer stack. For s-polarization, this field takes the form

$$\mathbf{E}_j^{(s)}(z) = E_0 \left[t_{0,j_L}^+ e^{ik_{jz}z} + t_{0,j_L}^- e^{-ik_{jz}z} \right] \hat{\mathbf{y}}, \tag{1.23}$$

while for p-polarization two different components must be considered, as illustrated in Figure 1.9,

$$\mathbf{E}_{jx}^{(\mathrm{p})}(z) = E_0 \frac{k_{jz}}{k_0 n_j} \left[t_{0,jL}^+ \mathrm{e}^{\mathrm{i}k_{jz}z} + t_{0,jL}^- \mathrm{e}^{-\mathrm{i}k_{jz}z} \right] \widehat{\mathbf{x}}, \tag{1.24}$$

$$\mathbf{E}_{jz}^{(\mathrm{p})}(z) = E_0 \frac{k_{0x}}{k_0 n_j} \left[t_{0,jL}^+ \mathrm{e}^{\mathrm{i}k_{jz}z} + t_{0,jL}^- \mathrm{e}^{-\mathrm{i}k_{jz}z} \right] \widehat{\mathbf{z}}. \tag{1.25}$$

The absorbance $A_j(\lambda)$ of layer j at a given wavelength λ and polarization is obtained by integrating the optical power dissipated at a depth z, $Q_j(z)$, over the propagation direction. This power dissipated is related to the time-averaged Poynting vector $\langle S_j(t) \rangle_z$, which in turn depends on the electric field E_j inside the layer, such that

$$A_j(\lambda) = \frac{1}{I_0(\lambda)} \int_0^{d_j} Q_{jz}(z) dz = \frac{1}{I_0(\lambda)} \int_0^{d_j} -\frac{\partial}{\partial z} \left[\frac{1}{2} \mathbb{R}\mathrm{e} \left(\mathbf{E}_j \times \mathbf{H}_j^* \right) \right] dz, \tag{1.26}$$

where $I_0(\lambda)$ is the irradiance of the incident light and $\mathbf{H}_j^*$ is the complex conjugate of the magnetic field at layer j, which can be related to $\mathbf{E}_j$ by applying the Maxwell equations of (1.13). Finally, the absorbance of layer j can be written as

$$A_j^{(\mathrm{s})}(\lambda) = \frac{c\varepsilon_0 \mathbb{I}\mathrm{m}(k_{jz}) \mathbb{R}\mathrm{e}(k_{jz})}{k_0(\lambda)\, I_0(\lambda)} \int_0^{d_j} \left| E_j^{(\mathrm{s})}(z) \right|^2 dz, \tag{1.27}$$

for s-polarized light, while for p-polarization it takes the form

$$A_j^{(\mathrm{p})}(\lambda) = \frac{c\varepsilon_0 \mathbb{I}\mathrm{m}(k_{jz}) \mathbb{R}\mathrm{e}(k_{jz})}{k_0(\lambda)\, I_0(\lambda)} \int_0^{d_j} \left(\left| E_{jx}^{(\mathrm{p})} \right|^2 + \left| E_{jz}^{(\mathrm{p})} \right|^2 \right) dz. \tag{1.28}$$

The EQE and J_{sc} of thin film solar cells or photoelectrodes can therefore be determined by direct substitution of these absorbances into equation (1.1).

The transfer matrix method shown so far is a very powerful tool, as it allows us to describe in a simple way and with great accuracy the light absorption and propagation in planar systems composed of multiple thin layers, where the light is coherent. Nevertheless, it can be further extended to planar systems also incorporating thicker layers where this coherency is lost, as it happens for example in glass substrates, which are usually millimeter-thick.

The generalized version of the transfer matrix method[125, 126] considers a system composed of N thin multilayer stacks (MS) and M thick layers (TL), as schematically represented in Figure 1.11. The electric field propagation in each individual multilayer stack is determined as previously described, but the incident irradiance, or electric field amplitude, is now different for each multi-stack and depends on the full system configuration. In order to determine it, another matrix description will be used, this time relating changes in the irradiances, instead of the electric fields, for each element (thin multi-stack or thick layer).
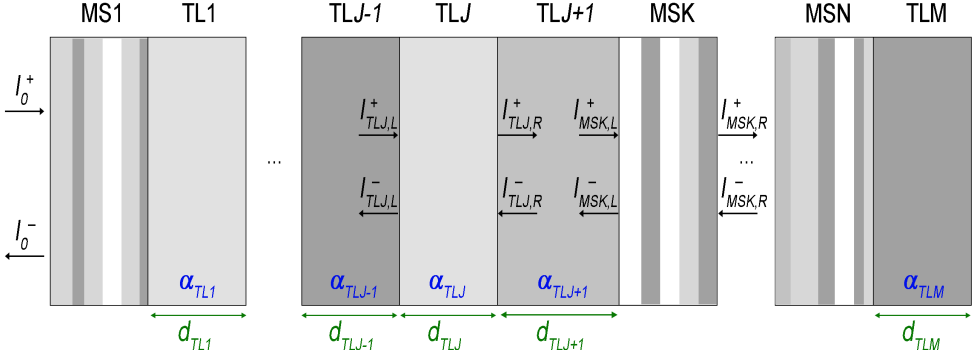
Figure 1.11: Illustrative example of a system considered for the application of the general transfer matrix method, combining N thin multilayer stacks with M thick layers. The irradiances at different interfaces are represented, as they are now the quantities to be related.

In this regard, the matrix IRR_{MS}, that relates the irradiances before and after a given multilayer stack is given by

$$IRR_{\text{MS}} = \frac{1}{T_{\text{MS}}} \begin{bmatrix} 1 & -R_{\text{MS}} \\ R_{\text{MS}} & T_{\text{MS}}T'_{\text{MS}} - R_{\text{MS}}R'_{\text{MS}} \end{bmatrix}. \tag{1.29}$$

where the different matrix elements are related to the total transmittance and reflectance of the multi-stack when illuminated from the front side (T_{MS}, R_{MS}) and from the back side (T'_{MS}, R'_{MS}), and can be obtained by direct application of equations (1.21) and (1.22).

On the other hand, the changes in irradiance alongside the thick layers can be described by a matrix IRR_{TL}, which depends on the absorption coefficient, α_{TL}, and on thickness, d_{TL}, of the material

$$IRR_{\text{TL}} = \begin{bmatrix} e^{\alpha_{\text{TL}}d_{\text{TL}}} & 0 \\ 0 & e^{-\alpha_{\text{TL}}d_{\text{TL}}} \end{bmatrix}. \tag{1.30}$$

In a similar way as before, it is possible to write a single matrix that describes the behavior of the irradiance in the full tandem system, or in parts of it, simply by multiplying all the matrices corresponding to the different multi-stacks and glasses, in the proper order. From that, one can easily get the irradiance I_{MS} that enters in a given thin multilayer stack, which in turn is directly related to the electric field amplitude that enters that multi-stack, $|E_{\text{MS}}|^2$, by

$$|E_{\text{MS}}|^2 = \frac{k_{0z}}{k_{MSz}} \frac{I_{\text{MS}}}{I_0} |E_0|^2. \tag{1.31}$$

where k_{0z} and k_{MSz} are the wave vectors in the z direction at the incident medium and

at the entrance of the given multilayer stack MS.

This allows us to fully describe the electromagnetic field propagation in any planar device, composed both by thin and thick layers, and to obtain the amount of light transmitted, reflected, or absorbed, which emphasizes the importance of this generalized version of the transfer matrix method as a tool to model planar optical systems.

1.5.2 Optimization problems

The transfer matrix method previously presented allows one to easily model light propagation in planar devices with a given fixed configuration in terms of the number of layers, materials, and thicknesses. Although it is a very powerful tool, its sole use is typically insufficient to find optimal configurations that can bring photonic devices toward their limits. Scanning all variable parameters of the system is feasible when the parameter space is small, but it gets extremely inefficient and time and computational resource-consuming when the number of free variables increases. For this reason, it is necessary to choose and use appropriate optimization algorithms in combination with the transfer matrix method to obtain the optimal configurations that can maximize energy efficiency in different devices.

Generally, an optimization problem consists in finding the best parameters, within a certain domain, that maximize or minimize a given function, called objective function, which may be subjected to one or more constraints. These problems start from an initial solution, which is obtained by evaluating the objective function at an initial point that is commonly set by the user, and move towards a final optimal solution that is obtained after several iterations, by application of an appropriate optimization algorithm. The general flow of an optimization problem is represented in Figure 1.12.[127–129]

The choice of an adequate optimization algorithm depends on the objective function, size of the parameter space, type of constraints applied, and use of continuous or discrete variables, among others. Depending on the algorithm used, local or global solutions can be found.

Local optimization algorithms are typically more suitable to solve, in a faster way, simple problems where the region of the optimal solution is known. They start from an initial position, defined by the user, and move towards the local extreme (maximum or minimum) in that region. For this reason, the choice of an appropriate initial point is mandatory to find a good solution for the objective function.[128, 130] The most commonly used local optimization algorithms rely on the gradient of the objective function to move more effectively toward the optimal solution.[129–132] A good example is the least mean squares algorithm, which is commonly applied to fit experimental data with a given function $f(x)$ and uses a gradient-based method to minimize the summed squares of the difference between the data collected and the values of the function $f(x)$, for all points x_i.[128, 132–134]
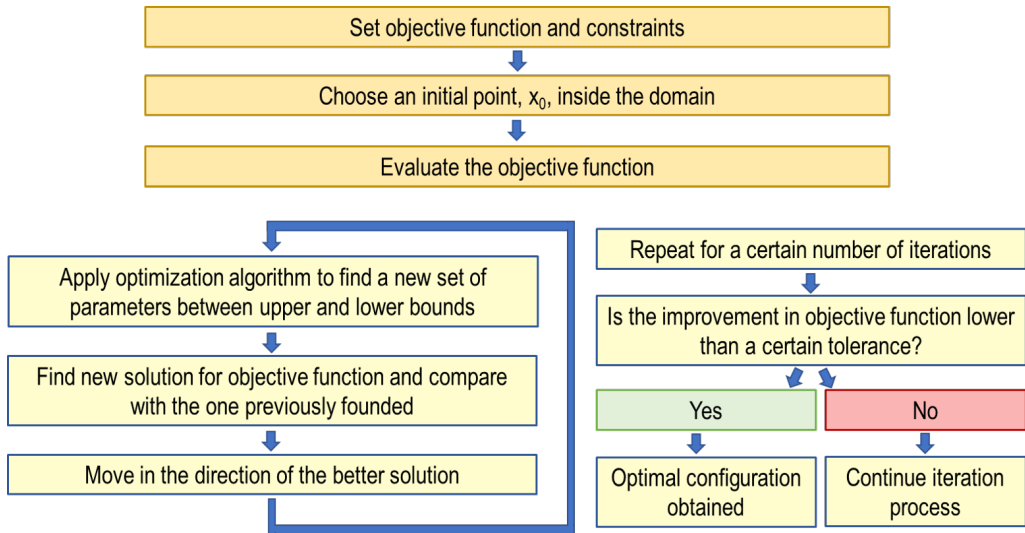
Figure 1.12: General flow for solving an optimization problem.

On the other hand, global optimization algorithms focus on finding the globally optimal solution to the problem, which usually is more time-consuming but also more effective when little is known about the objective function. They typically start from a single candidate, or a population of candidate solutions, but revise the whole parameter space in search of the optimal parameters.[129, 130, 135] An example of a global optimization algorithm, recurrently used in this work, is the genetic algorithm, which is inspired in the biological natural selection process. It starts from a randomly chosen population of individuals and evolves in such a way that the chromosomes of the fitter individuals (i.e., the ones that provide better solutions for the optimization function) are passed to the next generation, through the crossover operation. In addition, it allows for the spontaneous appearance of mutations, which will help in accessing the whole parameter space to search for the globally optimal solution.[129–131, 136]

1.6 Thesis outline

The current thesis is focused on studying the interplay of ergodicity and absorption in several configurations that are relevant to either promote a more sustainable use of the energy or to enhance the transformation of sunlight into other forms of energy.

In this regard, Chapter 2 takes advantage of the ergodicity previously demonstrated in a half-cylinder photonic plate to develop a novel light-guiding structure capable of emitting diffuse and polarized light for a broad range of wavelengths in the visible spec-

trum with low losses, and that shows potential for application in liquid crystal displays. By incorporating in the ends of this guide PVK solar cells with a bandgap appropriately tuned to the emission wavelength of a red light source, a highly efficient recycling of the stray light back into electricity is predicted.

Chapter 3 explores the limiting performance of bismuth vanadate as a photoanode for the water-splitting reaction. In particular, high sensitivity EQE characterization allows us to thoroughly examine the absorption and conversion limits of this semiconductor material, especially in the region below the bandgap, and to determine with high precision its effective refractive indexes. These will later be used to predict the maximum short circuit current density achievable, when in the presence of appropriate light trapping.

Finally, in Chapter 4, tandem devices incorporating the previously studied highly transparent bismuth vanadate photoanodes together with organic photovoltaic cells are designed and fabricated for unassisted water splitting. To bring the STH conversion efficiency of the tandem towards its limit, a PM6:Y6-based OPV cell with a bandgap close to the theoretically optimal one is chosen and a multilayer structure with optimized configuration is introduced in between the two different tandem elements to perfectly balance the light absorption among them, taking into account the absorption profile of the different semiconductor materials.

Design of a novel guiding structure for the emission of diffuse polarized light with low losses

As noted in the introduction chapter of the current thesis, ergodic geometries are useful for maximizing absorption while trapping and guiding light, but also for a diffuse and homogeneously distributed light emission.

In this chapter, we make use of a half-cylinder photonic plate, where such an ergodicity was previously demonstrated,[103] to design a novel light guiding structure capable of emitting diffuse polarized light for a broad range of wavelengths in the visible spectrum while converting back into electrical energy the light with the unwanted polarization. In addition to the h-CPP central element, the structure we consider incorporates a multilayer reflective polarizer (MRP) and a highly reflective bottom element composed of irregular sequences of dielectric layers optimized with the aim of maximizing the ratio between the light emitted with s- relative to p-polarization and of minimizing the light losses. Two identical PVK photovoltaic cells, with a wide bandgap tuned to the emission of red light, are incorporated on the front and back ends of the structure, to convert into electricity the light with the unwanted polarization that gets trapped inside the guide.

2.1   Design of the guiding structure to polarize and recycle light

The light guiding structure herein proposed to achieve diffused emission of polarized light combined with potential harvesting and conversion back into electricity of the unwanted polarization is schematically represented in Figure 2.1.

In its core lies a half-cylinder photonic plate for an ergodic propagation of the light, as previously described. On top of the periodic array of half-cylinders, the guide incorporates a non-absorbing multilayer reflective polarizer composed of an irregular sequence of dielectric layers, aiming to achieve broadband polarization selectivity. In addition, it integrates a highly reflective element on the bottom and two perovskite photovoltaic cells
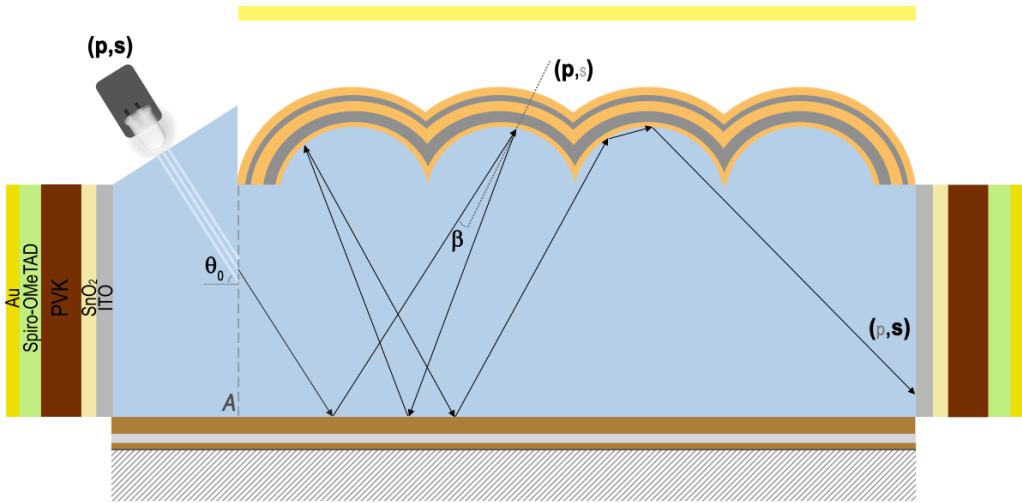
Figure 2.1: Schematic representation of the guide proposed in this thesis, showing its main elements: a half-cylinder photonic plate covered by a multilayer reflective polarizer, a bottom reflective element, and two perovskite solar cells on the front and back ends. Light is introduced with a certain deviation angle, θ_0, relative to the guide axis, through an optical prism or any other suitable light coupling element. The drawing is only a schematic representation of the guide. The dimensions are not at scale and the number of dielectric layers or half-cylinders do not correspond to any of the studied configurations.

for light conversion to electricity at the front and back ends.

The materials and dimensions of the guiding structure were chosen to correspond to the ones previously fabricated,[103] and are schematically illustrated in Figure 2.2. In particular, a photonic plate consisting of a periodic array of 346 interconnected half-cylinders is deposited on top of a glass substrate with a thickness of 2.2 mm and a total length of 3.1 cm, using a transparent polymeric material that fully covers the substrate, with a refractive index $n = 1.52$, that matches the one of the glass. The diameter of each fiber is 103.8 μm, but they are slightly overlapping in such a way that their centers are separated by only 89.64 μm; their height is 25.30 μm and the vertical distance between the top of each fiber and the glass substrate is 78.08 μm.

Light from a light-emitting diode (LED) may be coupled through the top interface using a prism or any other suitable light coupling element, in such a way that the rays cross the incident plane A with a given angle θ_0 relative to the guide axis. To achieve an even and homogenous diffuse light emission from the top of the guide, the incident rays should point towards the central part of the guide, which corresponds to an angle θ_0 deviating from the axis guide by 12 deg, a value that results from the total length and height of the guide considered in this thesis. At the incident plane A, 600 rays equally spaced by 1 μm, which may undergo up to 200 reflections within the structure, were considered.
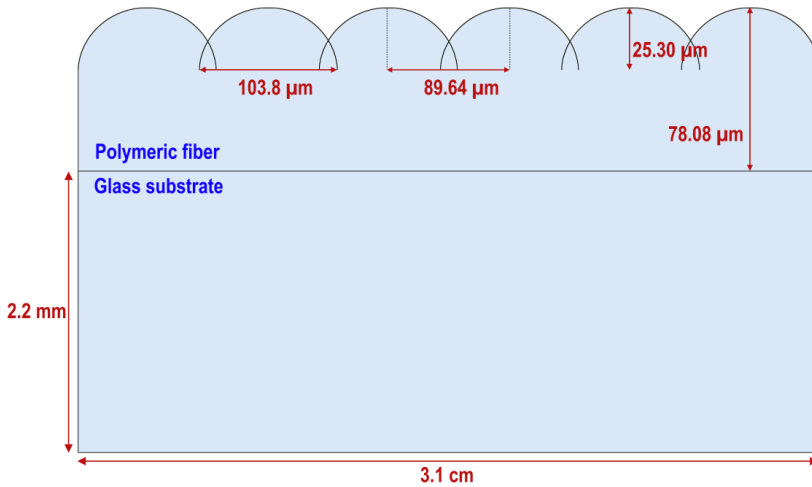
Figure 2.2: Schematic representation of the photonic plate considered in this thesis, with the main dimensions properly indicated. This drawing is not at scale and the number of half-cylinders does not correspond to the one used in this thesis.

2.2 Computational optimization of the guiding structure

The light guiding structure herein proposed incorporates a unique combination of periodic order in the h-CPP and disorder in the MRP. It contains a complex combination of micro and nanometric structures, and therefore the approach implemented to resolve the electromagnetic wave propagation combines the use of ray optics tracing in the core of the guide together with a full wave vector propagation in the multilayer structures.

Each time a given ray is incident at one of the interfaces that separate the core of the guide from the MRP or the bottom reflective element, the corresponding intersection point and angle of incidence are computed using a home-made ray tracing code. Considering this angle of incidence, the transfer matrix formalism, described in Section 1.5.1, is applied to determine the light transmission, reflection, and absorption, for each of the polarization components and wavelengths of the light source. We may note that this formalism can be used with a very large accuracy, even for the non-flat interface between the h-CPP and the MRP, provided the radius of the cylinders is two to three orders of magnitude larger than the thicknesses of the layers in the polarizer. The light reflected is then used to update the irradiance of the ray propagating inside the guide after this intersection. The light absorbed in the bottom reflector will account for the losses. The light transmitted through the top reflective polarizer is used to calculate the power that would be detected on a plane parallel to the guide (see Figure 2.1), whenever the ray transmitted does not reenter in the guide through one of the neighboring cylinders.

For a given ray, the total light transmitted through the polarizer or lost by absorption for a certain wavelength is obtained by summing the contributions from all the trajecto-

ries (up to 200) undergone inside the guide. Finally, to simulate the behavior of a realistic beam, with a micrometric diameter, the results obtained for the 600 different initial rays are averaged, for each one of the three different wavelengths considered: 466 nm, 560 nm, and 630 nm, corresponding to the emission of blue, green and red light from the LEDs, respectively.

To obtain the optimal configurations for both multilayer structures, the MRP and the bottom high reflective element, an inverse design approach is implemented by means of a genetic algorithm, presented in Section 1.5.2. For the top reflective polarizer, the target is to maximize the transmission of p-polarized light, while minimizing the one with s-polarization, so the polarization extinction power ratio of the beam is chosen as the quantity to minimize during the optimization procedure. On the contrary, for the bottom reflective element, the objective is to minimize the light losses by absorption.

2.2.1   Polarization separation in the multilayer reflective polarizer

The combined effect of the h-CPP and the multilayer reflective polarizer is the key to an efficient separation of the polarization components, enabling the transmission of the p-polarization while maintaining the s-polarized light trapped inside the fiber plate. For this reason, it is crucial to ensure that we obtain what may be generically defined as the optimal configuration. This implies a good choice of materials and number of layers for the MRP, as well as a proper definition of the objective function and constraints for the optimization problem.

A combination of dielectric materials alternating high and low refractive index was thus considered for the MRP, in analogy with a distributed Bragg reflector. In particular, WO_3 and LiF were chosen, provided that they exhibit a large index contrast while, at the same time, they can be effectively deposited on top of the h-CPP by thermal evaporation to form the curved multilayer polarizer. At this stage, a simple 200 nm thick silver mirror, also deposited by thermal evaporation, was chosen to fully cover the opposite surface of the guiding structure and to provide the high reflectivity needed at this interface. The refractive indexes of all materials used to perform the computational simulations can be found in Appendix A.

The total number of layers in the MRP was varied and, for each case, the thicknesses of the materials were optimized using the genetic algorithm available at MATLAB® Global Optimization Toolbox,[137] considering the default creation, crossover, and mutation functions. The objective function to minimize was the wavelength-averaged polarization extinction ratio of the power detected on a plane parallel to the guide. Three different constraints were considered, which included: (i) an unconstrained optimization, (ii) setting the minimum p-polarized wavelength-averaged power to be detected on a plane parallel to the guide to 55% of the incident irradiance, and (iii) simultaneously limiting the maximum color discrepancy in the power to be detected on a plane parallel to the guide to less than 5% and the minimum wavelength-averaged p-polarized power to

40% of the initial intensity. To compare the effect of the different constraints, the number of layers in the MRP was fixed to 25 and the variations in power computed for each case are presented in Figure 2.3.
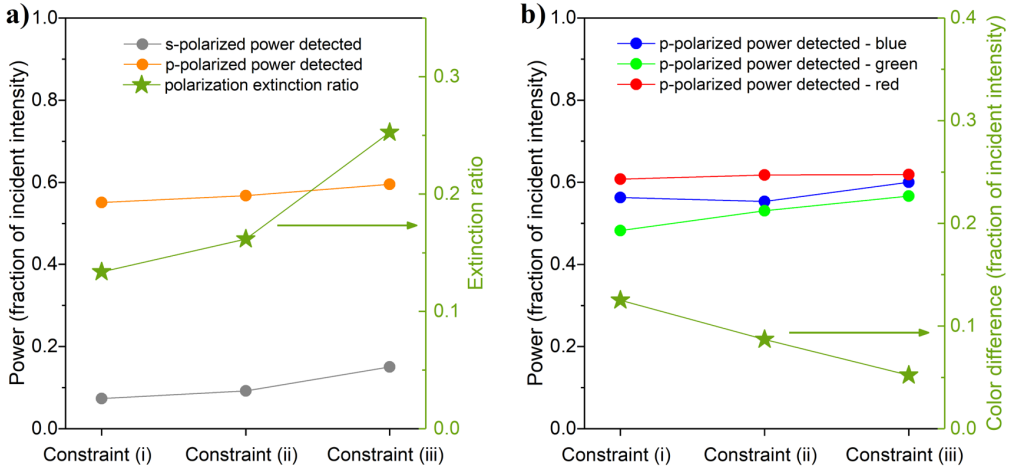

Figure 2.3: Comparison between the different optimization constraints applied, for a 25-layer MRP, in terms of a) wavelength-averaged s- and p-polarized power detected (left axis), as well as polarization extinction ratio (right axis) and b) p-polarized power detected for each wavelength (left axis) and maximum color difference observed (right axis). In these simulations, the reflective element considered on the bottom of the h-CPP is a 200 nm thick silver.

As illustrated in Figure 2.3 a), the lowest wavelength-averaged polarization extinction ratio for the power detected in a plane parallel to the guide was observed when no constraints were imposed at all (case (i)), which is attributed to a smaller amount of s-polarized light transmitted. However, the power detected for the p-polarization is also the lowest and the color balance for the p-polarized light is the worst of the three, as shown in Figure 2.3 b). In opposition, imposing constraint (iii) leads to very well color-balanced configurations (as expected), together with the highest values of wavelength-averaged p-polarization power detected. Unfortunately, this came with the cost of a considerably higher polarization extinction ratio, as the structure obtained for the MRP allowed a high amount of s-polarized light to be transmitted out. Finally, the most balanced results were obtained for constraint (ii), which combined reasonably low polarization extinction ratios with a quite high amount of p-polarized light detected and a color discrepancy that is in between the other two cases. So, although all three approaches would yield a final structure that would successfully accomplish the separation of the two polarization components, the use of the second constraint ensures a sufficiently high emission of p-polarized light, with a good color balance, without significantly increasing the polarization extinction ratio. Therefore, constraint (ii) was applied to optimize the configuration of the MRP for an increasing number of dielectric layers, from 9 to 33.
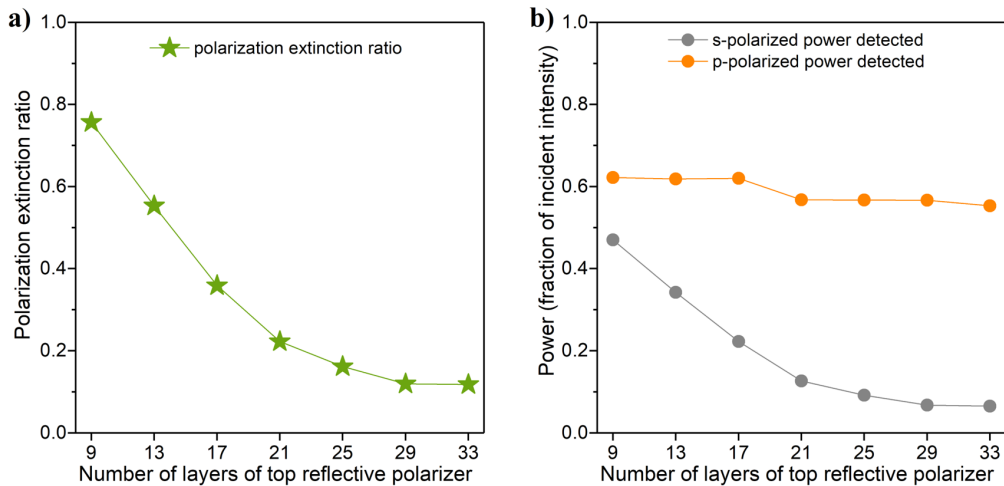
Figure 2.4: Change in a) polarization extinction ratio and b) wavelength-averaged power detected for the s- and p-polarization components separately with the number of layers in the MRP (from 9 to 33). In these simulations, the reflective element considered on the bottom of the h-CPP is a 200 nm thick silver mirror.

The results obtained are plotted in Figure 2.4. According to these results, a decrease in the polarization extinction ratio is observed with the increase in the number of layers in the MRP, up to 29. Beyond that, no improvement in terms of polarization separation is obtained. As seen in Figure 2.4 b), the continuous decrease in the s-polarized light transmitted through the top surface saturates after 29 layers in the MRP. Provided the p-polarized light is to a large extent independent from the number of layers in the MRP, the polarization extinction ratio as a function of the number of layers follows a similar pattern as the transmission of the s-polarization light.

To get a better insight into the mechanism responsible for the polarization separation, the reflectance maps of s- and p- components of the light for the optimized MRP structures with 9 and 29 dielectric layers were computed as a function of the wavelength and angle of incidence at the interface that separates the h-CPP from the multilayer polarizer and are plotted in Figure 2.5.

As seen in the reflectance maps, when s-polarized light propagating inside the guiding structure is incident at the interface separating the h-CPP from the optimal 29-layer MRP, a broadband reflectivity approaching unity, spanning from 450 to 650 nm, is obtained regardless of the angle of incidence, from 0 to 90 deg. Thanks to that, the transmission of light with s-polarization is quite low when this 29-layer structure is deposited on top of the photonic plate. This effect, however, is far from being achieved when fewer dielectric layers are considered in the reflective polarizer. For the particular case of a 9-layer MRP, a fairly high reflectance is observed for the s-polarized light between 550 nm and 650 nm, which includes the wavelengths corresponding to the emission of green and red light, but
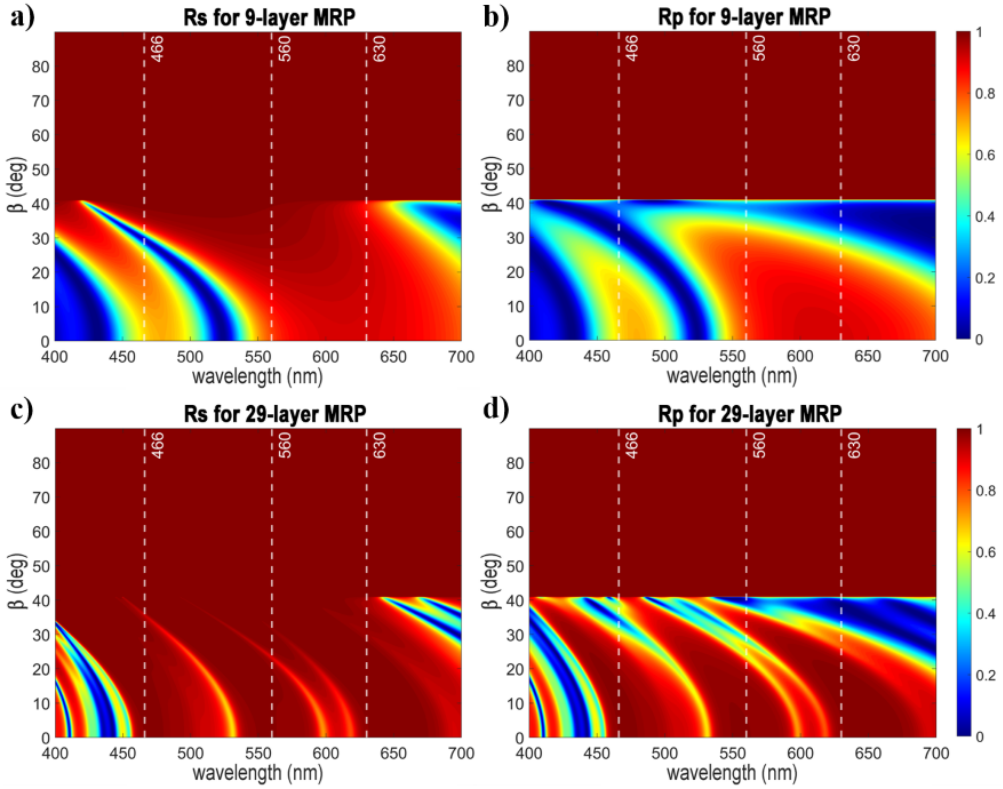
Figure 2.5: a), c) s- and b), d) p-polarization components of the reflectance for the optimized MRP structures with a), b) 9 and c), d) 29 dielectric layers, as a function of the wavelength and angle of incidence (β) at the interface that separates the h-CPP from the multilayer polarizer (see Figure 2.1). The three different wavelengths considered in this thesis for the emission of blue, green, and red light are identified in the maps, with vertical dashed lines.

it drops considerably outside of that range, and in particular in the region of blue light emission. As a consequence, the s-polarized light transmitted increases significantly, in agreement with the results of Figure 2.4 b).

On the contrary, regardless of the number of layers in the MRP, for the three wavelengths of interest, the p-polarized light is transmitted rather effectively when the angle of incidence at the interface separating the h-CPP from the polarizer ranges, approximately, from 30 to 40 deg, in other words, when the p-polarized light is incident in the neighborhood of the Brewster angle. When this MRP is deposited on top of the h-CPP, the combination of the chaotic nature of the light propagation in the core of the fiber plate and the semi-cylindrical shape at the top of the guide ends up allowing for many rays to be incident on the polarizer within the 10-degree range for which the p-polarization reflectance drops, resulting in a rather effective emission of p-polarized light. Since in

this case there are no significant differences between the use of 9 or 29 layers in the MRP for the wavelengths under study, the power detected for the p-polarized light was not very affected by the number of dielectric layers of the reflective polarizer, as seen in Figure 2.4 b).

2.2.2 Reduced light losses in the reflective bottom element

In the analysis performed in the previous section, a 200 nm thick silver mirror, deposited by thermal evaporation, was used as the bottom reflective element of the guiding structure. This material presents a quite high reflectivity (always above 97% for the wavelengths under study, as shown in Figure 2.6), but it is still far from being a perfect reflector.
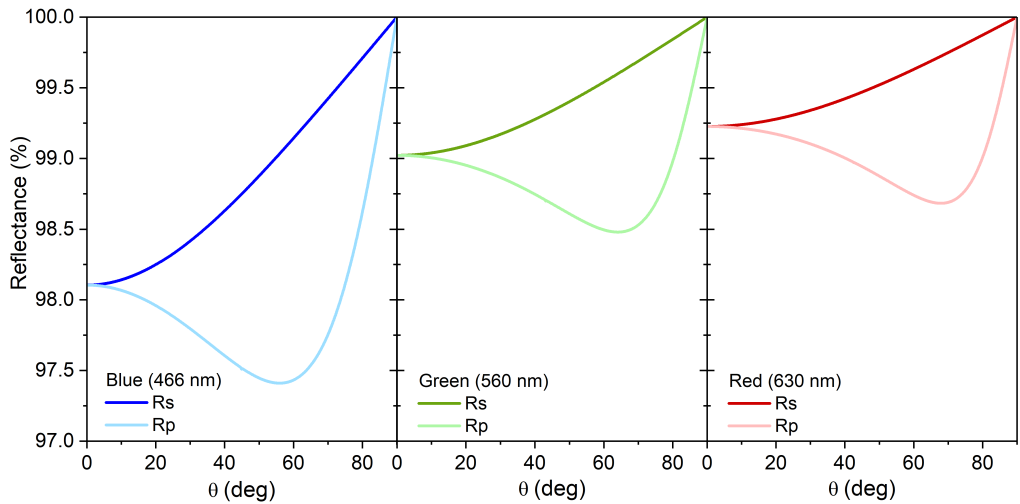
Figure 2.6: Reflectance of the 200 nm thick silver mirror, considered as the bottom reflective element when performing the optimization of the top MRP, for the two different polarization components and the three wavelengths of the light corresponding to the blue, green, and red.

Given that the light rays perform multiple reflections inside the h-CPP, this non-perfect reflection will eventually lead to significant light losses at the bottom interface. As is illustrated in Figure 2.7 a), these absorption losses increase with the number of layers in the top reflective polarizer, especially for the s-polarization, associated with lower emission and better trapping of the light inside the guiding structure. For the particular case of the optimal 29-layer MRP, the total light losses at the bottom mirror almost reach 9% of the incident irradiance when the average of the two polarizations is considered.

With the purpose of minimizing such light losses at the bottom interface, a reflector combining a set of layers intercalating dielectric materials of contrasting refractive index, finished with a thick silver metal layer, was considered instead of the simpler Ag mirror.
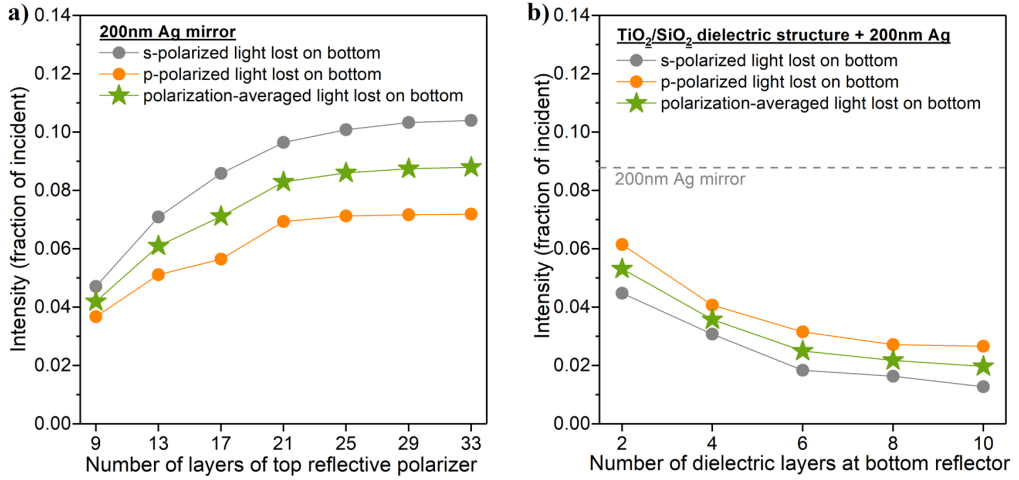
Figure 2.7: a) Light losses at the bottom reflective element when a 200 nm thick silver mirror is considered, as a function of the number of layers in the top MRP. b) Light losses at the bottom reflective element when a TiO_2/SiO_2 dielectric structure is used, as a function of the number of dielectric layers, for the optimal 29-layer MRP.

In this case, TiO_2 and SiO_2 were used as the high and low refractive index materials, respectively, as they present a very high index contrast (see Appendix A) and the planar nature of the bottom interface easily allows for the deposition of these materials by magnetron sputtering. To get the optimal configuration for the bottom reflective element, a procedure similar to the one used for the optimization of the top MRP was employed. A genetic algorithm was chosen for the inverse design optimization of this element, where the objective function to minimize was the average of the absorption losses between the s- and p-polarized light. During the optimization process, the configuration of the top multilayer reflective polarizer was fixed to the optimal 29-layer structure determined in the previous section. On the other hand, the number of dielectric layers in the bottom reflector was varied until some convergence was reached.

The results obtained for the optimization of the bottom element are presented in Figure 2.7 b) as a function of the number of dielectric layers considered. As seen in the figure, a considerable reduction of light lost by absorption is obtained for all the cases when compared with the thick silver mirror considered previously (represented by the dashed line), and it decreases with the number of layers until saturation is reached for an 8-layer structure of TiO_2/SiO_2 finished with thick Ag. In that case, an almost loss-less bottom reflector is obtained, with only 2.2% of the total incident irradiance being absorbed in this element. Of particular interest is the fact that the highest reduction in losses happened for the s-polarized light, which is strongly trapped inside the guiding structure. This demonstrates the potential of the inverse design optimization to find a configuration that selectively reflects in an almost perfect way the s-component of the light, as shown in Figure 2.8, to achieve minimal losses in the entire guide.
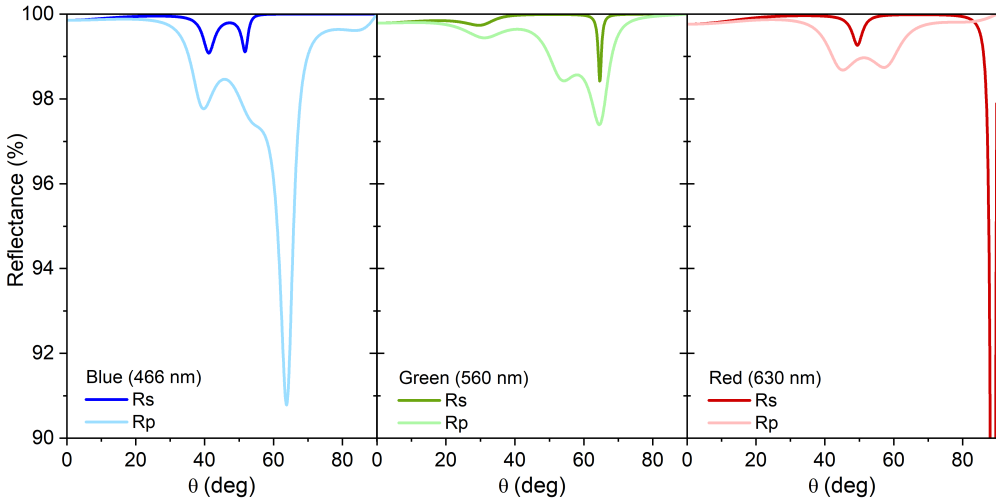
Figure 2.8: Reflectance of the optimized 8-layer reflective bottom element, for the two different polarization components and the three wavelengths of the light corresponding to the blue, green, and red.

The optimal configuration of the guiding structure herein presented is therefore the one that incorporates a 29-layer MRP on top of the h-CPP and a reflective element with 8 dielectric layers followed by thick Ag on the bottom interface. This configuration will be henceforward referred to as h-CPP-P29-R8 and their exact layer sequences and thicknesses are indicated in Table 2.1.

Table 2.1: Configuration of the optimal guiding structure, h-CPP-P29-R8.

Top multilayer reflective polarizer
Substrate/WO$_3$(59nm)/LiF(125nm)/WO$_3$(216nm)/LiF(105nm)/WO$_3$(73nm)/
LiF(95nm)/WO$_3$(200nm)/LiF(74nm)/WO$_3$(232nm)/LiF(90nm)/WO$_3$(69nm)/
LiF(105nm)/WO$_3$(53nm)/LiF(126nm)/WO$_3$(250nm)/LiF(114nm)/WO$_3$(66nm)/
LiF(113nm)/WO$_3$(149nm)/LiF(97nm)/WO$_3$(73nm)/LiF(88nm)/WO$_3$(88nm)/
LiF(85nm)/WO$_3$(137nm)/LiF(87nm)/WO$_3$(73nm)/LiF(143nm)/WO$_3$(250nm)/air
Bottom reflective element
Substrate/TiO$_2$(64nm)/SiO$_2$(231nm)/TiO$_2$(166nm)/SiO$_2$(70nm)/TiO$_2$(116nm)/
SiO$_2$(108nm)/TiO$_2$(57nm)/SiO$_2$(71nm)/Ag(250nm)/air

As clearly observed, the inverse design optimization applied in this thesis leads to a fully irregular distribution of thicknesses in both the MRP and bottom element. In other

words, no correlation can be established among the thicknesses of the different layers, emphasizing the usefulness of such an inverse design approach to find solutions largely differing from the trivial ones. Note that changing the materials would result in a different layer sequence but the physics under study would essentially remain the same.

2.2.3   Collection of light escaping from the sides

The optimal configuration for the guiding structure determined in the previous sections allows for very effective separation of the polarization components without increased light losses. In particular, as indicated in the light distribution scheme of Figure 2.9, close to 42% of the total light entering the guiding structure (74% of p-polarized and 9% of the s-polarized incident light) is diffused through the top interface with a polarization extinction ratio of nearly 0.1, while the light losses on the bottom reflector are limited to 2.2%. This means that more than 54% of the total initial light, mostly with the s-polarization, gets trapped inside the guide, and will continue to propagate until arriving either at the front or the back ends of the guide. The wavelength distribution of the light that reaches such interfaces is shown in Figure 2.10 and it clearly demonstrates that the guide can very effectively trap the s-polarized light at the wavelengths of interest. Since the angle of incidence was chosen so that the incident ray arrives at the central part of the guiding structure, the amount of light reaching both ends is very similar. Changing the initial angle would result in a higher amount of light reaching one of the ends in comparison to the other, as will be demonstrated later in Section 2.2.4.

We may note that the irradiances reported in the scheme of the light distribution sum up only to 98%, as we have neglected light rays which, when emitted from the top of the guide, intersect an adjacent half-cylinder and reenter the photonic plate. Accounting for the contribution from these rays would significantly increase the computation complexity without introducing any relevant change in the h-CPP-P29-R8 optimal structure or the results reported so far.

So, for each of the wavelengths under study (indicated by the vertical dashed lines in Figure 2.10) there is close to 90% of the initial s-polarized and 20% of the p-polarized light which ends up reaching the front and back ends of the guide and that can be effectively recycled back to electricity when incorporating PV cells in these interfaces. To maximize the power conversion efficiency, high V_{oc} solar cells, with the bandgap edge adjusted to the wavelength emission of the red LED, must be used. In particular, PVK solar cells appear to be very promising for this application, as they offer broad bandgap tunability and have low thermalization losses. In this regard, a perovskite with a $Cs_y FA_{(1-y)} Pb(I_x Cl_{(1-x)})_3$ composition and a CsCl to PbI_2 ratio of 0.17, which has wide E_{g} of 1.76 eV and whose refractive indexes were taken from the literature[138] and are plotted in Appendix A, was chosen as the active layer of the photovoltaic cells, with configuration: ITO(100nm)/SnO$_2$(20nm)/PVK/Spiro(200nm)/Au(100nm).
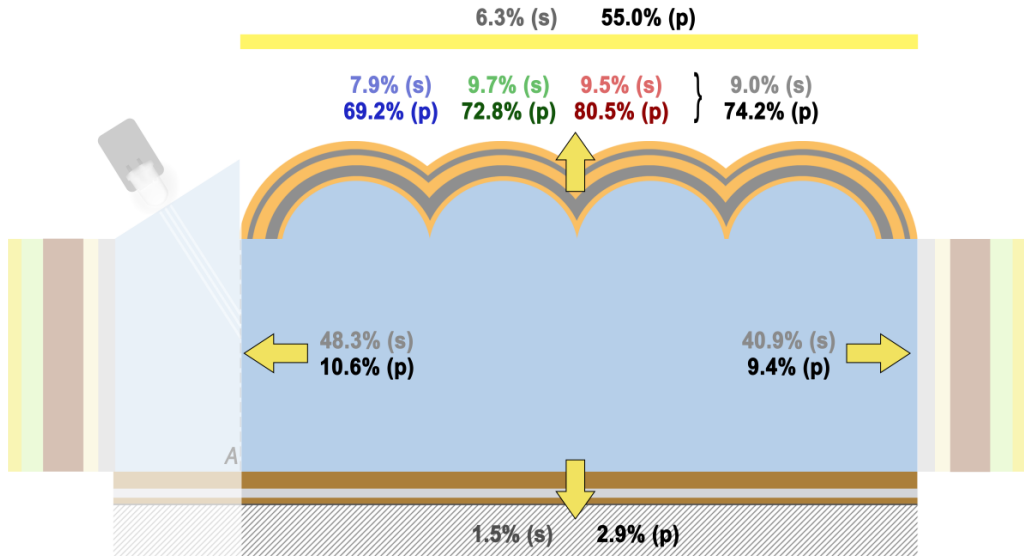
Figure 2.9: Distribution of the light irradiance alongside the guiding structure and power detected in a plane parallel to the guide, for the s- (grey) and p-polarization (black) components separately. For the power detected, the light lost by absorption on the bottom reflector and the one that propagates until reaching the edges of the guide, where the PVK cells are incorporated, only the wavelength-averaged value is shown. For the light transmitted through the top multilayer reflective polarizer, the individual wavelength components are also presented: 466 nm (blue), 560 nm (green), and 630 nm (red).
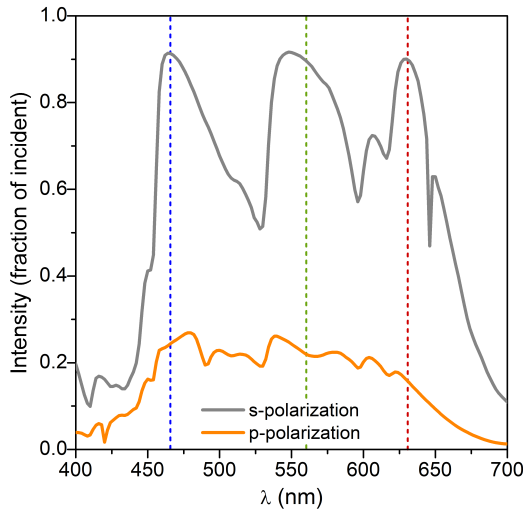
Figure 2.10: Fraction of the incident irradiance that reaches either the front or back interfaces of the h-CPP-P29-R8 guiding structure, for s- and p-polarized light, as a function of the wavelength. The three wavelengths used for the optimization are indicated by the vertical dashed lines.
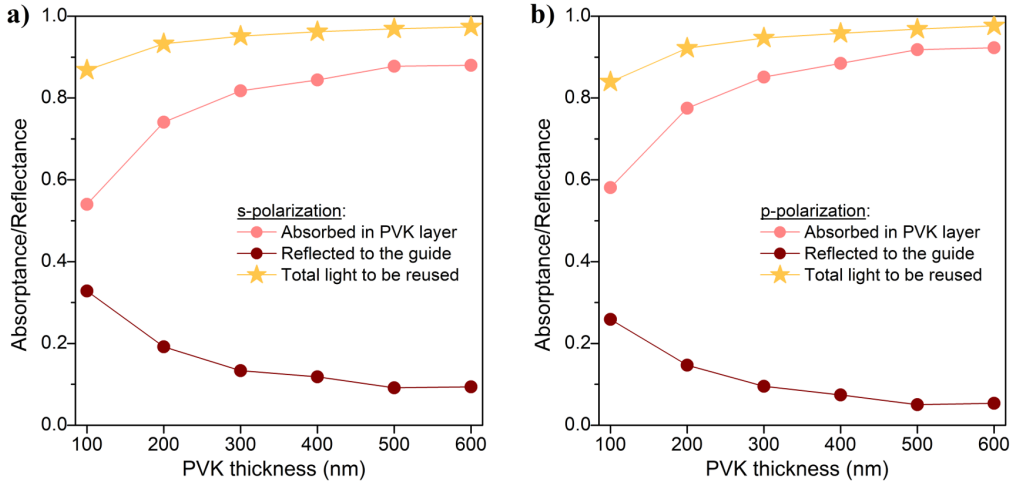
Figure 2.11: a) s-polarized and b) p-polarized light absorption in the active layer of the perovskite cells and reflection back to the fiber plate, together with the total amount of light that can be reused after reaching the ends of the guiding structure (sum of the previous two contributions), as a function of the PVK active layer thickness. The three magnitudes are normalized to the irradiance reaching the front and back interfaces of the guiding structure, and the values obtained correspond to the average contribution of the three wavelengths under study: 466 nm (blue), 560 nm (green), and 630 nm (red).

Figure 2.11 shows, as a function of the thickness of the perovskite layer and light polarization, the amount of light that can be reused when these solar cells are incorporated into the ends of the guide. This happens either because the light is absorbed in the PVK active layer and can be converted into electricity or because it is reflected back to the guiding structure, where it can continue to propagate ergodically. These calculations were performed taking into account the angle of incidence and the intensity of the light reaching the ends of the guide for each one of the 600 initial rays considered in this thesis and reveal an increase in the PVK light absorption and in the amount of light to be reused with the thickness of the active layer. In particular, when a PVK layer thickness of at least 500 nm is considered, close to 90% of the light reaching the ends of the guide is absorbed in the active layer of the solar cell, with very low light losses of about 3%.

To estimate the power conversion efficiency of these 500 nm perovskite photovoltaic cells when directly illuminated by blue, green, and red LEDs, we considered the normalized spectral irradiances plotted in Figure 2.12, which were adapted from the datasheets of commercially available LEDs with the desired central wavelengths and narrow spectral and angular emission.[139–141] The J_{sc} of the cell was calculated using the transfer matrix formalism described in Section 1.5.1, taking into account the angle of incidence at the interface between the guiding structure and the PVK cell for each individual ray, from which the average current density was determined. For the V_{oc} estimation, it was

considered that the PV cell was operating at the radiative limit and that the irradiance of each LED was equal to 1 sun. This is a valid assumption if a radiant power of 5 mW and an illumination area of about 0.3 mm by 1 cm are considered and results in a V_{oc} of 1.51 V for the PVK composition selected, by applying equation (1.3). Regarding the fill factor, a fixed value of 0.80 was chosen, in agreement with the values typically reported in experimental works involving high-quality PVK cells.[142–144]

The calculation of the power conversion efficiency of the PVK cell, when illuminated by each of the different LEDs, was performed by direct application of equation (1.5), where the total irradiances of the LEDs were obtained by integration of the spectral irradiances of Figure 2.12. The values determined for all photovoltaic parameters are presented in Table 2.2.
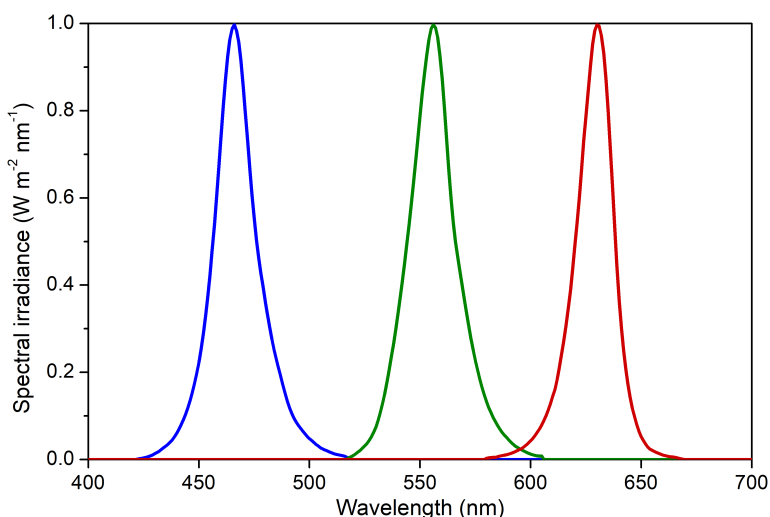
Figure 2.12: Spectral irradiances of the blue, green, and red LEDs considered as light sources for the calculation of the power conversion efficiency of the wide bandgap PVK solar cells. These spectra were adapted from the datasheets of References 139–141.

According to the results, power conversion efficiencies ranging from 38.86% for the blue to 51.88% for the red LED were obtained, with thermalization losses in the PVK layer accounting for the largest loss fraction in this conversion. Further tuning of the perovskite composition to have the bandgap edge matching exactly the emission of the red LED would help to reduce to the minimum possible these thermalization losses and would result in even higher PCEs for the solar cell. Regardless of that, in all cases the conversion efficiencies estimated under narrowband illumination from the LEDs are well above the Shockley-Queisser limit of the cells under sunlight illumination,[69] which is about 27% for the bandgap of the PVK considered.

Table 2.2: Photovoltaic parameters predicted for the wide bandgap PVK solar cells when placed on the ends of the h-CPP-P29-R8 guiding structure, under direct illumination of blue, green, and red LEDs.

LED	J_{sc} (A/m^2)	V_{oc} (V)	FF	I_{LED} (W/m^2)	PCE (%)
Blue	7.91	1.51	0.80	24.59	38.86
Green	10.29	1.51	0.80	26.25	47.37
Red	9.14	1.51	0.80	21.29	51.88

In summary, the use of the guiding structure herein proposed with high bandgap PVK solar cells incorporated in its front and back ends is expected to allow for the direct use of 37.1% of the initial light irradiance, corresponding to the 74.2% of p-polarized light emitted from the top MRP, and for the conversion to electric power of more than 25% of the incident light, considering the color-averaged PCE for the calculation of the recycled power. This means that 62.1% of the power can be efficiently used in our configuration. The nearly 38% of light losses estimated, which include the s-polarized light transmitted from the MRP, the losses on the bottom reflector, and the parasitic absorption and thermalization losses on the PVK solar cell, are considerably below the 50% of light lost solely by the use of the absorbing polarizers typically employed in LCD displays.

2.2.4   Spatial and angular distribution of the light transmitted

The LEDs commercially available for LCD applications emit light within a cone of a given angular range, as illustrated in Figure 2.13 a). To study the effect produced by this angular distribution of the emitted light, small variations in the angle of incidence of the light respective to the normal of the incident plane *A* were considered for the optimal h-CPP-P29-R8 configuration found in Section 2.2.2. In particular, a set of 5 different discrete angles of incidence were studied, centered at the 12 deg angle used for the optimization of the guide structure, as shown in Figure 2.13 b).

Figure 2.14 shows how the angle of the light emitted from the LED relative to the guide axis affects the light distribution alongside the guiding structure, namely in terms of power detected in a plane parallel to the guide, light absorbed at the bottom reflective element and light reaching each of the ends of the guide.

As the figure clearly indicates, for the smallest angle of incidence of 6 deg, the power detected for both polarization components, as well as the light losses by absorption at the bottom reflective element, are considerably smaller than for the remaining cases. This happens because the incident light is practically directed towards the front end of the guide (the one opposed to the plane of incidence, *A*), reaching that interface before performing a significant number of reflections, which is in agreement with the findings from Figure 2.14 c) and d). For the remaining angles of incidence, it is possible to
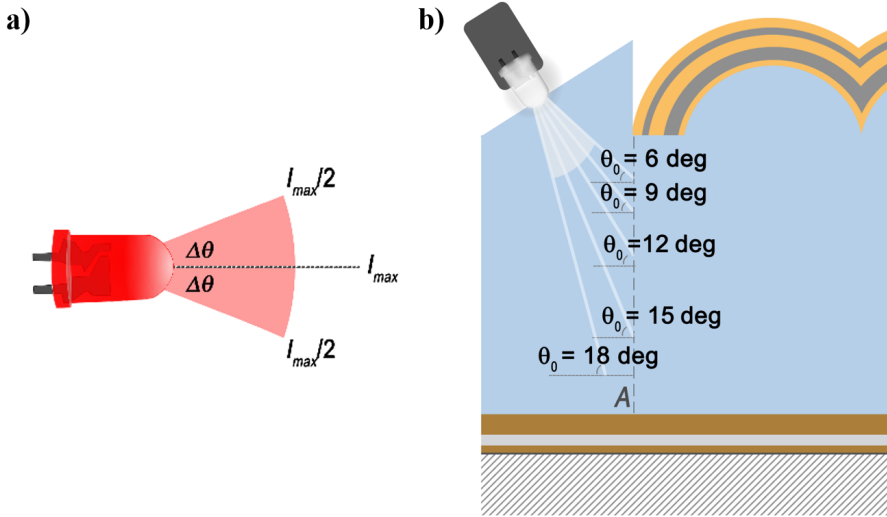
Figure 2.13: a) Schematic representation of the light emission by an LED source, within a cone of angular range $\Delta\theta$. Although the intensity of the light emitted is maximum in the forward direction, there is still substantial light emission for angles deviating up to $\Delta\theta$ relative to the normal to the surface of the LED, which must be taken into account when such sources are used. b) Change in the angle of incidence of the light in the guiding structure due to the emission of the LED within a given angular range, with the indication of the incident angles considered in this section. This scheme is merely illustrative and the dimensions of the different elements, as well as the angles, are not at scale.

observe a decrease in the power detected for both polarizations, together with a very slight increase in the light absorbed at the bottom element and the one reaching the front and back ends of the guide, whenever the angle of the incident light is increased from 9 deg to 18 deg. In particular, when the angle of the LED light emission relative to the normal of the plane of incidence is 12 deg, the value chosen for the optimization of the guiding structure, the polarization extinction ratio obtained is slightly lower and there is a better balance between the light reaching the front and back ends of the guide.

Regardless of that, the light distribution in the guide does not change considerably with the angle of incidence, which confirms that the optimal structure obtained in the previous chapters is very well suited to be used in real devices where the LED emits light within a certain angular range.
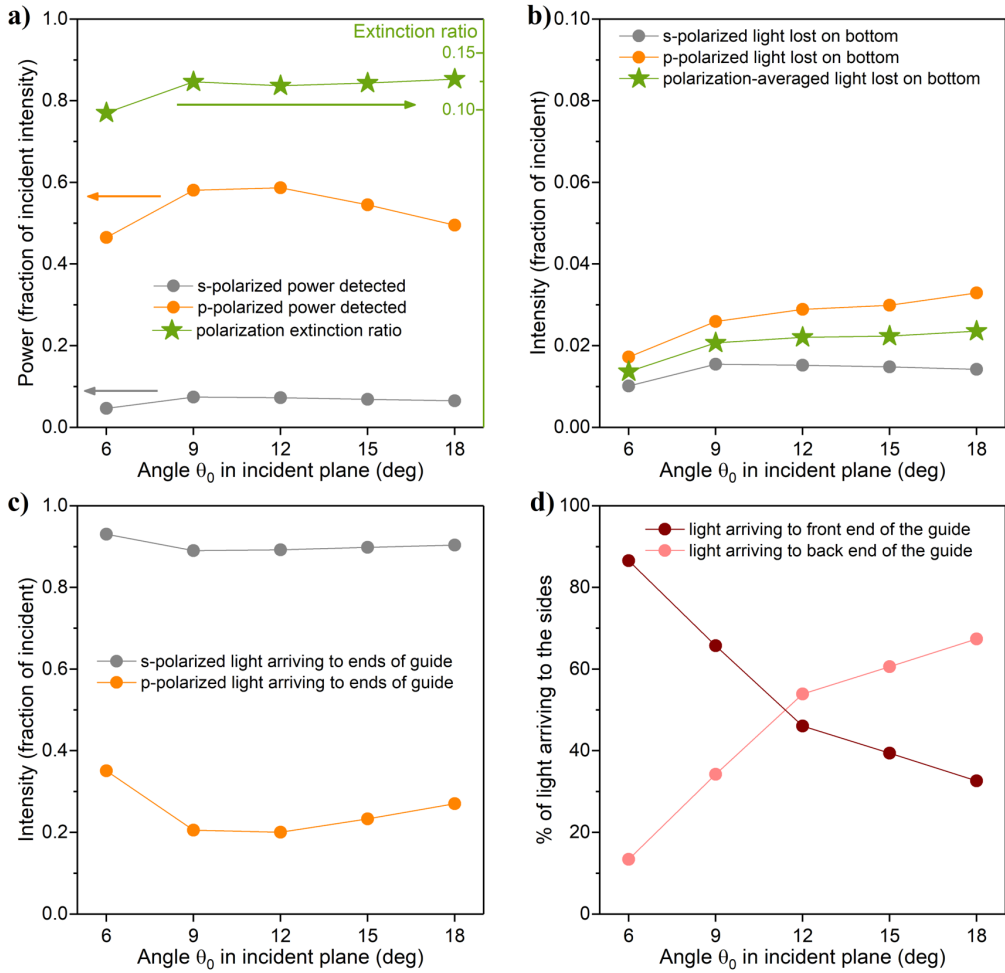
Figure 2.14: a) s- and p-polarized power detected on a plane parallel to the guide (left axis), as well as polarization extinction ratio (right axis), b) light losses on the bottom reflective element, c) light arriving to the ends of the guiding structure for each of the polarization component and d) relative amount of light guided towards each one of the ends of the fiber plate as a function of the angle of incidence relative to the guide axis, θ_0.

To finalize, the properties of the p-polarized light emitted out of the guiding structure from the MRP top interface towards the user of the LCD display must be accessed for the different angles of the incident light under study. In particular, it is important to determine the spatial and angular distribution of the light transmitted, to guarantee that the guiding structure emits homogeneously distributed diffuse polarized light, as required for these applications.

Figure 2.15 shows the spatial distribution along the horizontal position of the guide of the p-polarized light emitted from the MRP, for the different incident angles and the three wavelengths of the light under study. As clearly observed, for the 12 deg angle of incidence considered for the optimization of the guide, light is mostly emitted from the central part of the fiber plate, regardless of the wavelength considered. Shifting towards higher angles of incidence results in a stronger emission closer to the incident plane A (see Figure 2.1), while the use of lower angles shifts the light emission to the front end of the guide. For the limiting case where the light is incident with an angle of 6 deg relative to the incident plane, an emission very close to the front end of the guide is obtained. This is in agreement with the previous findings of Figure 2.14 that, for such an angle of incidence, light is almost directed to the front end of the guide. Nevertheless, when the contributions of all angles of incidence are considered, as in a real LED source, a fairly homogenous light emission is observed along the top surface of the guide.

A similar effect is observed for the angular distribution of the p-polarized light emitted from the guiding structure, as demonstrated in Figure 2.16 for both blue, green, and red light. In this case, regardless of the wavelength of the incident light, a quite narrow angular distribution of the light emitted out of the guide is obtained when a single incident angle is considered, with higher angles of incidence resulting in emissions closer to the direction normal to the guiding structure (0 deg). However, when the contributions of all angles of incidence are considered, a broader emission of the light in an angular range spanning from -40 deg to $+10$ deg is obtained. This partial directionality of the light transmitted, combined with the emission of homogeneously distributed polarized light with reduced losses, should be optimal to increase the efficiency in optoelectronic devices, such as smartphones or tablets, which are typically viewed from a certain angular range.

Figure 2.15: Spatial distribution of the p-polarized light that is emitted from the guiding structure, for different angles of incidence, for 466 nm, 560 nm, and 630 nm wavelengths. The sum of all contributions is also shown (black dashed line).
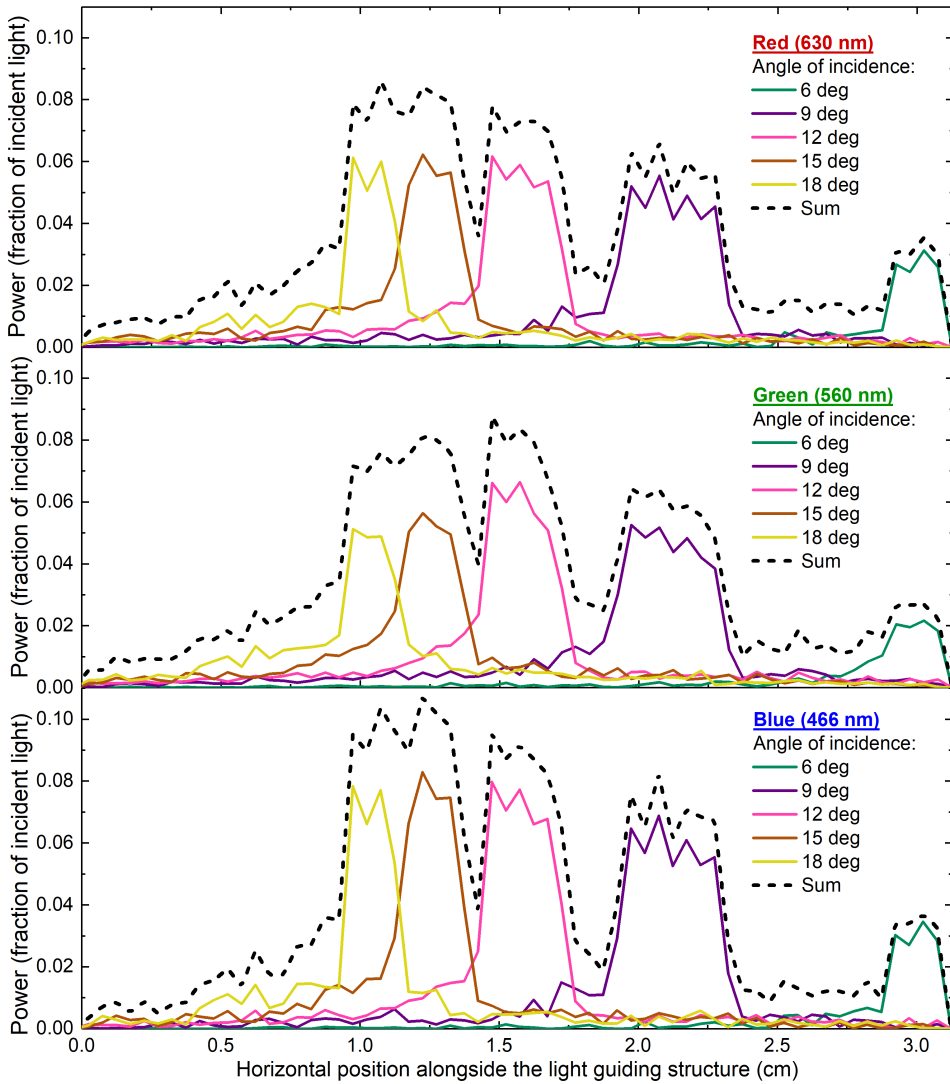
Figure 2.16: Angular distribution of the p-polarized light that is emitted from the guiding structure, for different angles of incidence, for 466 nm, 560 nm, and 630 nm wavelengths. The sum of all contributions is also shown (black dashed line).
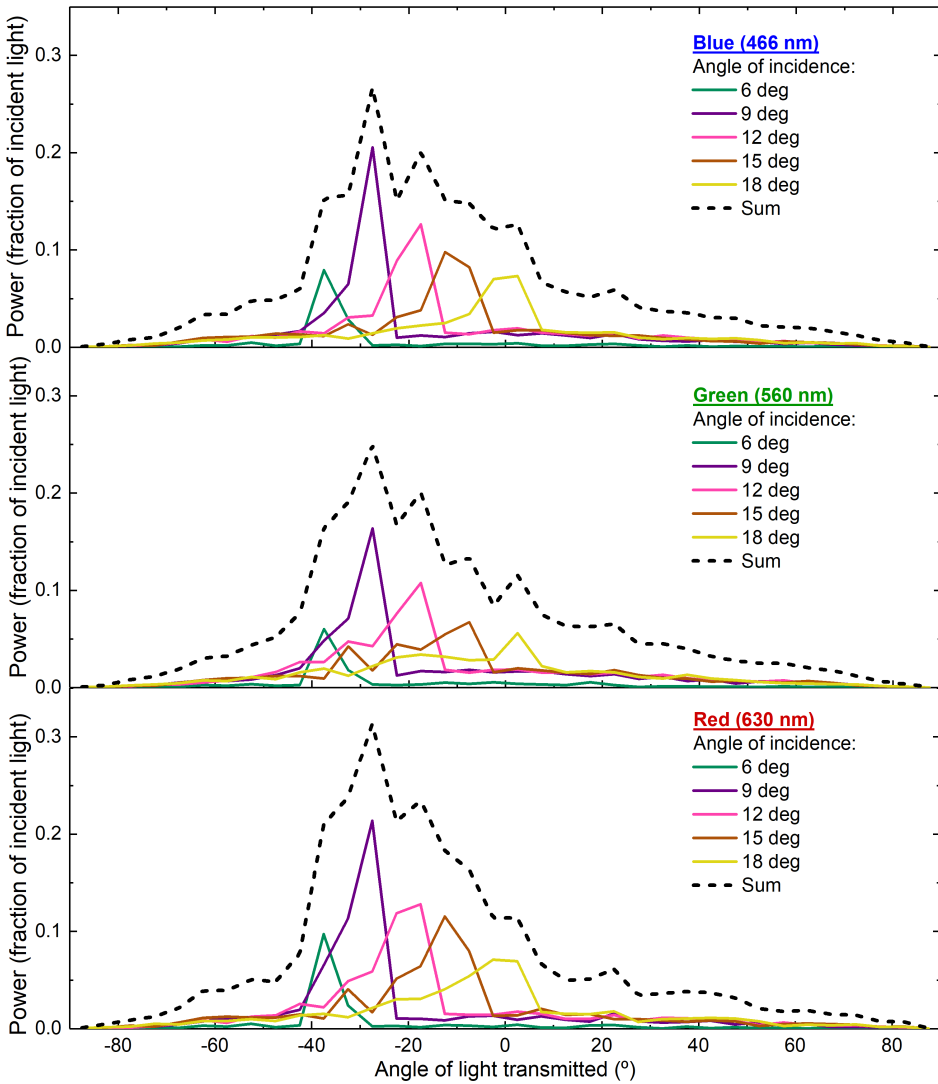
2.3   Experimental fabrication of the guiding structure

In an experimental realization of such light guiding system, the MRP was deposited by magnetron sputtering on top of an h-CPP, fabricated on an Eagle XG glass substrate using a curable polymer with a refractive index of $n = 1.52$ and following the procedure reported in the literature.[14] Note that a combination of TiO$_2$ and SiO$_2$, instead of WO$_3$ and LiF, was chosen for the experimental fabrication of the MRP, as these materials present a high refractive index contrast and are compatible with magnetron sputtering deposition.
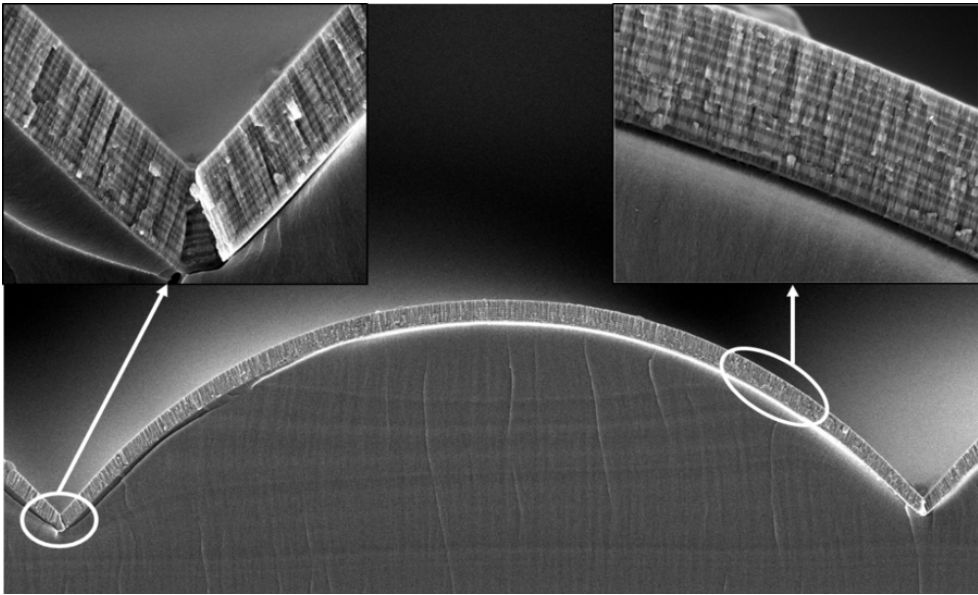
Figure 2.17: Cross-section SEM images of the multilayer reflective polarizer deposited on top of the corrugated h-CPP, where the profile variation alongside one cylindrical fiber can be seen. The inset pictures correspond to the magnified SEM micrographs in the region of intersection between two adjacent fibers (top left corner), showing the good coverage obtained for the multilayer structure, and in the dielectric multilayer (top right corner), emphasizing the irregular distribution of thicknesses deposited. The darker areas are conformed by SiO$_2$ layers and the lighter ones by TiO$_2$. From Reference 14.

SEM micrographs in Figure 2.17 show a high-quality stack, without any signs of cracking and with very good coverage of the h-CPP, including the region of intersection between adjacent half-cylinders. However, a closer look at the cross-section SEM micrograph reveals a variation in the thickness of the MRP layers within a single half-cylinder. Indeed, the central part is covered by thicker layers than the regions close to the intersection between half-cylinders. As can be seen in Figure 2.18, the thickness of the layers linearly decreases in terms of the angle θ_{norm} between the normal to the fiber at a given point P and the normal to the guide axis on the bottom of the h-CPP, as this angle increases from 0 to nearly 60 deg, where the two adjacent cylinders intersect.
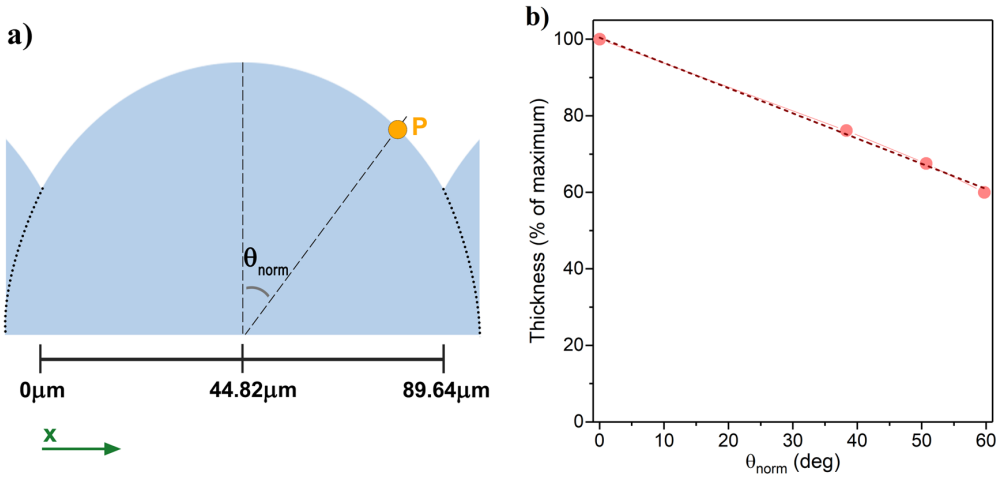
Figure 2.18: a) Schematic representation of a single half-cylinder, with the indication of the dimensions, x axis direction and angle θ_{norm} used for the calculation of the thickness profile. b) Thickness as a function of the angle θ_{norm} for 4 different points extracted from the SEM profile of the MRP, and the corresponding linear fitting of the data (dark dashed line).

By taking this thickness variation into account, we performed a re-optimization of the MRP structure to minimize the polarization extinction ratio. In this case, we considered a total of 25 layers, as this was seen to be sufficient to achieve saturation in the polarization extinction ratio when using the combination of TiO_2 and SiO_2. The wavelengths considered for the optimization of the MRP structure were 450 nm, 532 nm, and 635 nm, which correspond to the emission wavelengths of the lasers used to experimentally irradiate the guide with monochromatic light. The best configuration obtained is presented in Table 2.3.

Table 2.3: Configuration of the multilayer reflective polarizer experimentally deposited by magnetron sputtering.

Top multilayer reflective polarizer
Substrate/TiO$_2$(62nm)/SiO$_2$(128nm)/TiO$_2$(141nm)/SiO$_2$(129nm)/TiO$_2$(164nm)/
SiO$_2$(76nm)/TiO$_2$(65nm)/SiO$_2$(92nm)/TiO$_2$(52nm)/SiO$_2$(134nm)/TiO$_2$(140nm)/
SiO$_2$(125nm)/TiO$_2$(117nm)/SiO$_2$(156nm)/TiO$_2$(82nm)/SiO$_2$(120nm)/TiO$_2$(78nm)/
SiO$_2$(148nm)/TiO$_2$(53nm)/SiO$_2$(92nm)/TiO$_2$(44nm)/SiO$_2$(106nm)/TiO$_2$(85nm)/
SiO$_2$(116nm)/TiO$_2$(63nm)/air

As the results from Table 2.4 indicate, when one accounts for this thickness variation, the polarization extinction ratio increases due to an increase in the s-polarized light emitted out of the multilayer reflective polarizer. Nevertheless, a remarkable separation of the polarization components can still be expected. To experimentally measure such a ratio, an experimental set-up as the one schematically shown in Figure 2.19 a) was used to measure the light transmitted by the fabricated MRP on top of the h-CPP. The T_s and T_p measured spectra are shown in Figure 2.19 b) and compared to the ones determined by the numerical simulations. Note that in this configuration there is no reflective element at the bottom surface of the h-CPP, being the light introduced from this interface.

Table 2.4: Simulated light distribution in the guiding structure for the best 25-layer MRP made of TiO_2 and SiO_2 and optimized by taking into account the thickness variation experimentally observed alongside each half-cylinder.

	450 nm	532 nm	635 nm	Average
Light emitted from MRP (s)	16.8%	21.0%	38.7%	25.5%
Light emitted from MRP (p)	62.7%	70.8%	71.9%	68.5%
Polarization extinction ratio	0.273	0.314	0.543	0.377
Light absorbed at the bottom (s)	1.6%	1.0%	2.4%	1.6%
Light absorbed at the bottom (p)	5.2%	2.2%	2.8%	3.4%
Light reaching the PVK cells (s)	81.4%	77.5%	57.0%	72.0%
Light reaching the PVK cells (p)	29.4%	23.2%	16.6%	23.1%

The results from Figure 2.19 b) reveal a remarkable agreement between the T_s and T_p spectra experimentally measured and the theoretical predictions from the numerical model, for the whole range of wavelengths considered. In particular, the transmittance of the s-polarized light is very low in a broad wavelength range: below 5% for the red and green wavelengths and below 10% for the blue one, while the p-polarized light transmitted out of the MRP is always significantly higher, with values close to 20% for all the wavelengths of interest. This confirms the selectively reflective character of the MRP for the s-polarized light, which provides good separation between the two polarization components, as expected.
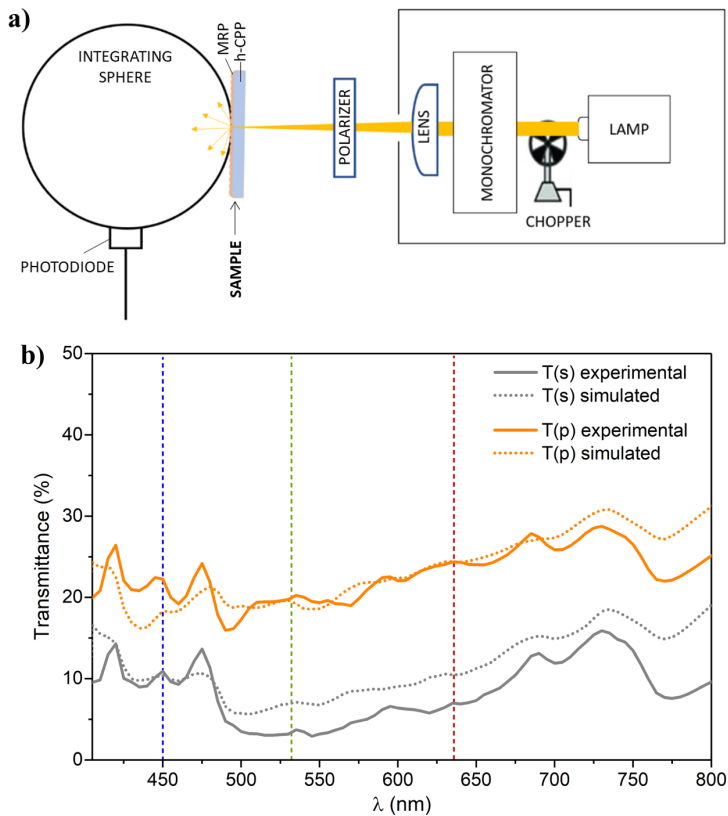
Figure 2.19: a) Optical setup used for the measurement of the total transmittance of the 25-layer reflective polarizer deposited on top of the h-CPP. Adapted from Reference 14. b) Comparison between the experimental measurements (solid lines) and the simulated spectra (dotted lines) for the light transmitted out of the MRP, using the configuration illustrated in a). The three wavelengths of emission of the light considered in this thesis are identified by the colored vertical dashed lines.

2.4 Conclusions

In this chapter, a novel light-guiding structure was proposed to emit diffuse polarized light with low losses while at the same time offering a high potential for light recyclability by converting the discarded light with the unwanted polarization into electrical power by using photovoltaic cells. This structure may find its primary application as the backlight unit of liquid crystal displays, which currently suffer from major energy losses due to the incorporation of absorbing polarizers.

The structure herein introduced relies, on the one hand, on a half-cylinder photonic plate to reach an ergodic propagation of the light, ideal to subsequently obtain a homogeneous light diffusion and, on the other hand, on a multilayer polarizer to achieve a broadband light polarization. To determine the optimal configuration for the MRP, an inverse design approach based on a genetic algorithm and simultaneously combining ray and wave optics propagation was implemented. The result was a structure capable of achieving a low polarization extinction ratio of about 0.1 for a broadband wavelength range spanning from 400 to 650 nm, with very low energy losses. In addition, it was demonstrated that the bandgap tunability and low V_{oc} losses intrinsic to many PVK solar cells make this type of cells ideal to reach a maximum conversion of the discarded light into electricity. Indeed, it was estimated that, by integrating PVK photovoltaic cells with bandgap appropriately tuned to the emission wavelength of the red LED into the front and back ends of the guide, the total light losses in the structure could be reduced to nearly 38%, a value which is significantly lower than the 50% of light lost solely by the use of absorbing polarizers employed in the commercial LCDs. However, this is not the ultimate limit and light power losses may be reduced even more by further optimization of the PVK cell or the geometry of the h-CPP.

Absorption limit in bismuth vanadate photoanodes

The search for energy-efficient designs encompasses, in addition to the minimization of the light losses explored in Chapter 2, the maximization of light absorption in the semiconductor active layers of the energy transformation devices to achieve optimal conversion efficiency.

In this regard, the present chapter aims at exploring the limits of light absorption and conversion in bismuth vanadate photoanodes for PEC water splitting, particularly in the region below the bandgap, where the presence of optical absorption states was recurrently observed,[145–158] but their contribution to the photon-to-current conversion was never explicitly addressed. To do so, high-sensitivity EQE measurements are employed to probe the low photocurrents generated by ultrathin (<100 nm) flat BVO photoanodes in this spectral region, which allows us to estimate in a more realistic way the maximum current density achievable by the BVO material when employed as a photoanode for the water-splitting reaction. To reach such a limit, one may need to combine a scattering mechanism to alter the trajectory of photons away from the incident direction with a light-trapping approach including, for instance, the design of the BVO layer to allow for an ergodic propagation of the light, as previously discussed. Aiming for such a double purpose, in the end of the chapter we propose a preliminary design for the BVO-based photoanode that incorporates a 3-dimensional (3-D) nano-structuration for increased photocurrent in the vicinity of the bandgap.

3.1   Bismuth vanadate used as photoanode in a PEC cell

Bismuth vanadate thin films were spin-coated on top of glass/FTO/SnO_2 substrates, following the procedure reported in the literature.[159]

Cross-section SEM analysis of Figure 3.1 a) reveals the formation of a compact BVO film, that completely covers the surface of the FTO. From this sort of micrograph, it was possible to extract the average thicknesses of the different layers, obtaining 90 nm for the BVO, as shown in Figure 3.1 b), and 600 nm for the FTO, while the SnO_2 layer was not

distinguishable in the SEM micrographs. In addition, from the top-view SEM analysis of Figure 3.1 c) we see that the BVO is composed of a polycrystalline structure with a grain size in the direction parallel to the layer ranging between 100 and 200 nm, as shown in the statistical distribution from Figure 3.1 d). Such small grains ensure negligible light dispersion by scattering, resulting in very transparent yellowish photoanodes, as revealed by the photograph in Figure 3.2 a). Indeed, despite the high absorption observed in the low wavelength range, corresponding to energies higher than the bandgap of the BVO, for the spectral region with a wavelength larger than 500 nm, the photoanode transmittance observed was higher than 60%, as seen in Figure 3.2 b).
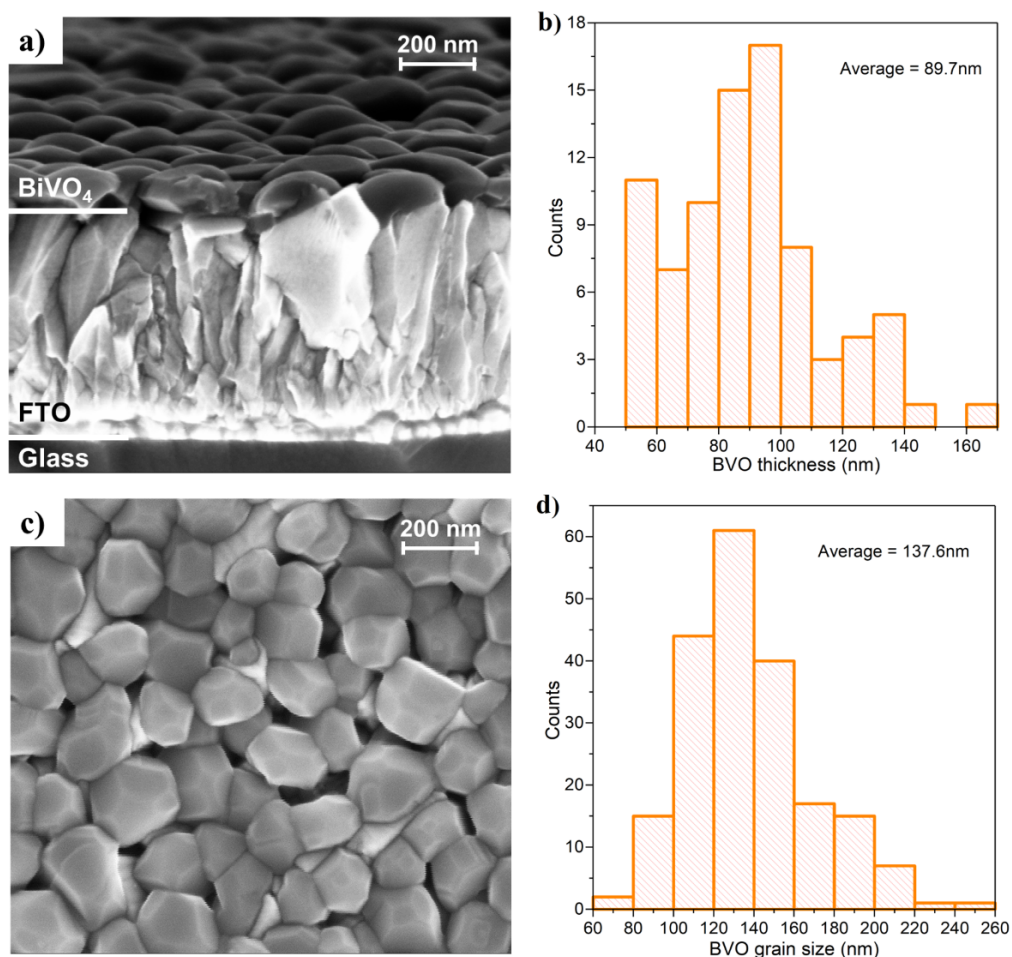

Figure 3.1: a) Cross-section SEM of a BVO photoanode, from which it was possible to extract the b) thickness of the BVO active layer at different positions in the sample and to calculate its average value. c) Top surface SEM of the same photoanode, which provided information about the d) grain size distribution.
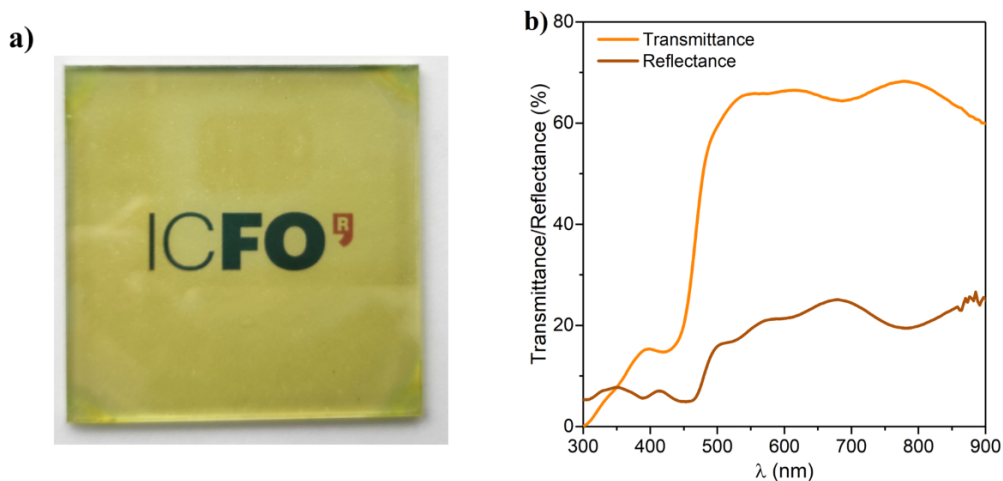
a)

b)

Figure 3.2: a) Photograph of a photoanode experimentally prepared, highlighting its high transparency, visible to the naked eye. b) Optical transmittance and reflectance spectra of the same photoanode.

To facilitate the oxygen evolution reaction, the BVO photoanodes were covered by a FeOOH/NiOOH catalyst deposited by consecutive photo-assisted electrodeposition of $FeSO_4$ and $NiSO_4$.[160] Despite the enhancement it brings in terms of PEC performance, this catalyst does not affect the optical properties of the photoanodes.

3.1.1   EQE from sub-bandgap excitation

To investigate the contribution to the photocurrent from sub-bandgap excitation, derived from the creation of an electron-hole pair after the absorption of a photon with an energy lower than E_g of the BVO, we performed high-sensitivity measurements of the EQE of the 90 nm thick BVO photoanodes mounted in a PEC cell containing a pH 9 electrolyte solution of 1.0 M KBi. A potential of 1.23 V_{RHE} was applied to the photoanodes, which were illuminated from a transparent glass window placed on the cell side opposite to the BVO, as shown in Figure 3.3 a). Detailed information about the EQE measurements can be found in Appendix B. Note that, to avoid interference from the monochromator grating second order lines, which may also contribute to the photocurrent, a series of low-pass optical frequency filters were added in between the monochromator exit and the PEC cell. To increase the signal-to-noise ratio and ensure reproducibility of the results, the EQE was determined from the average spectra of ten different BVO samples fabricated under the same conditions and measured following the same procedure, described in Appendix B.

From the EQE measurements covering the spectral region ranging from 2.0 eV up to 4.0 eV, shown in Figures 3.3 b) and c), one observes that when the effective length of the

BVO layer is doubled by a high reflectivity Ag mirror, which was placed facing the back side of the glass substrate that supports the photoanode, as seen in Figure 3.3 a), the contribution to the photocurrent increases for energies above as well as below the bandgap. For the sub-bandgap excitation (<2.4 eV), it is a clear indication that the contribution to the photocurrent occurs mostly from an excitation in the bulk of the BVO layer instead of a photoexcitation at the interfaces. As can be seen in Figure 3.3 c), for excitation energies in the $\sim 2.20 - 2.55$ eV range, the EQE in a logarithmic scale is increased by the same constant factor when the effective length of the BVO layer is doubled, which is in agreement with a material dependence of the EQE in this spectral range.
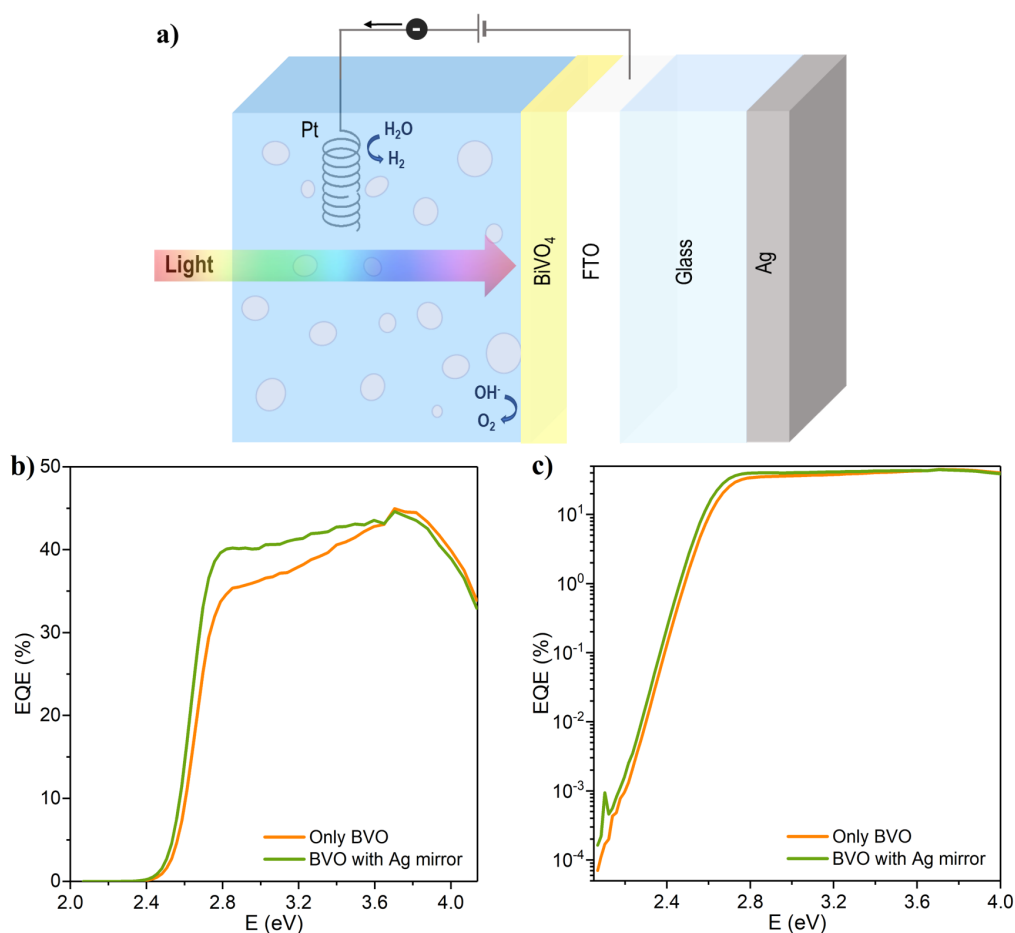
Figure 3.3: a) Configuration used for the EQE measurements of the BVO photoanodes, including a back Ag mirror. The image is not at scale. b), c) EQE of the photoanodes as a function of the photon energy, with and without the introduction of the reflective silver mirror. The curves shown in both plots correspond to the average values of the spectra obtained for ten different BVO photoanodes. In c), the EQE is plotted in a logarithmic scale to emphasize the exponential decay observed in the vicinity of the bandgap.

3.1.2 Effective refractive index

To obtain an accurate estimate of the limit photocurrent that one may expect to reach when illuminating a given BVO crystal, it is necessary to have an accurate numerical prediction of the real and imaginary parts of the BVO effective refractive indexes. For the below-bandgap region it is important to extract such effective refractive indexes also from the EQE measurements, instead of the standard procedure in which one would obtain them solely from reflectance or transmittance measurements. This is so because one is interested in the fraction of absorbed photons that contribute to effective charge transport in the BVO.

The procedure we followed was first to propose an analytical expression that would allow us to compute the imaginary part of the dielectric function as a function of the photon excitation energy. For that, we considered the Lorentz model and its modifications introduced by Tauc and Cody,[161–163] which are commonly used to provide an accurate description of the imaginary part of the refractive index in the neighborhood of the bandgap in semiconductor-type materials. To account for the contribution to charge transport from excitation of below-the-gap states, we modified these models by incorporating in them an Urbach tail term[164, 165] expressed as:

$$\alpha \propto \exp\left(\frac{E - E_\text{t}}{E_\text{U}}\right), \tag{3.1}$$

where α is the absorption coefficient, E_t is the transition energy at which the Urbach tail starts and E_U is the Urbach energy.

The final expressions used for the imaginary part of the dielectric function are given in Appendix A. Starting from there, we applied the Kramers-Kronig relations to numerically obtain the real part of such a dielectric function and to calculate the effective refractive indexes of the BVO. These indexes were used to compute the EQE, using the transfer matrix formalism described in Section 1.5.1. A least means square algorithm, presented in Section 1.5.2, was implemented to optimize the parameters of the models, in order to minimize the difference between the experimental and the simulated EQEs. For the transfer matrix computation, we neglected the contribution from the SnO_2 layer, not distinguishable in the SEM measurements. The best fittings were obtained using a Cody-Lorentz model with two bounded oscillators centered at 2.74 eV and 3.54 eV, together with an Urbach tail starting at an energy E_t of 2.55 eV and with an Urbach energy E_U of 40.6 meV, which is in line with the values reported for other amorphous semiconductor materials, such as amorphous silicon,[166–168] and some PVK compositions.[168–170] The bandgap parameter extracted from the fitting was 2.42 eV, in agreement with previous findings for the BVO material.[145–152, 171–173] The final values for the effective refractive index are shown as a function of the photon energy in Figure 3.4 a).
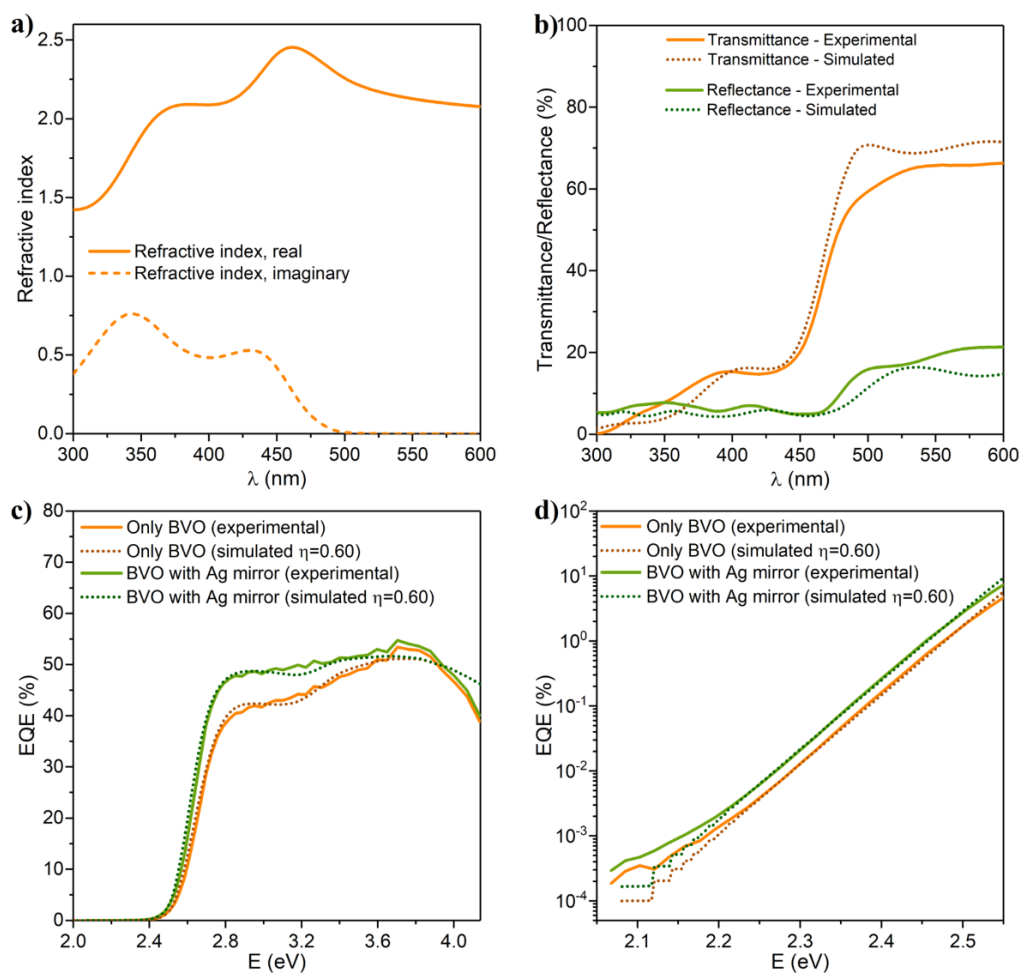
Figure 3.4: a) Real (solid) and imaginary (dashed) parts of the effective refractive index of the BVO, determined from the high sensitivity EQE measurements. b) Comparison between the experimental (solid lines) and the simulated (dotted lines) transmittance and reflectance spectra of the BVO. c) - d) EQE spectra of the BVO photoanodes immersed in a 1.0 M solution of KBi containing 0.2 M of SO_3^-, with and without the introduction of a very reflective back silver mirror. While c) shows the comparison between the experimental and simulated EQE of the BVO for the whole energy range under study, d) describes in detail the behavior in the bandgap and sub-bandgap region.

Using such effective refractive indexes, it was possible to fit with fairly good accuracy the transmittance and reflectance of the BVO photoanodes, as seen in Figure 3.4 b). Note that such fitting should only be approximate provided the effective refractive index we obtained neglects the contribution to photon absorption that does not lead to charge transport. On the other hand, when we performed an additional EQE measurement, this time immersing a BVO photoanode in a KBi electrolyte solution containing 0.2 M of

SO_3^- hole scavenger, we obtained a very good fitting for the EQE response in both configurations, the one with and the one without the highly reflective silver back mirror. As seen in Figure 3.4 c) and d), this fitting was particularly good in the low absorption region below the bandgap. Small deviations observed below 2.2 eV may either be related to the resolution limit of the EQE setup or the presence of deep defect states inside the bandgap, also observed for other materials.[168,174,175]

3.2 Maximize current density of bismuth vanadate

If the BVO layer could be configured in an ergodic geometry similar to the ones discussed in the introduction of this thesis, the contribution of the EQE tail resulting from the excitation below bandgap would most likely play a key role in reaching the ultimate conversion of photons into chemical energy. To achieve such kind of goal, one should implement a scattering mechanism to deviate the photon path from the incident direction and combine it with a photon trapping mechanism. The implementation of both strategies may result in a significant increase of the EQE, which may lead to an increase of the current obtained from the BVO photoanode in the PEC cell, provided that solar irradiance in the sub-bandgap region is higher, as seen in Figure 1.3 b).

This section is divided into two parts. In the first one, we assume light propagating in all directions in a thin BVO layer, which allows us to obtain an estimate of the maximum current density achievable when such a BVO layer is used as a photoanode in a PEC cell. In the second one, we theoretically consider a three-dimensional nano-structuration of the photoanode as a preliminary design leading to an increase in photocurrent.

3.2.1 Model limiting current density of BVO photoanodes

Previous estimations of the maximum photocurrent density generated by BVO photoanodes assumed a perfect light absorption above the semiconductor bandgap and a zero absorption for energies below E_g. This assumption established that the upper limit for the achievable current density from such BVO photoanodes is roughly 7.5 mA/cm^2.[176–178] In this thesis, we attempt to develop a simple theoretical model that considers light propagation in any direction within the tens-of-nanometer thick BVO layer, which would allow us to obtain a more realistic estimate of the maximum photocurrent achievable by such a BVO photoanode when the effective refractive indexes are the ones determined in Section 3.1.2.

In this model, the BVO thin active layer, with a given thickness d, is enclosed between two semi-infinite media, as seen in Figure 3.5. We assume that plane waves propagating in all directions denoted by θ on the xz plane have the same intensity at the point $z = z_0$, which is located in the yz plane at $x = 0$. The point z_0 chosen is equally separated from the interfaces that limit the BVO layer. As indicated above in this sub-section, we will
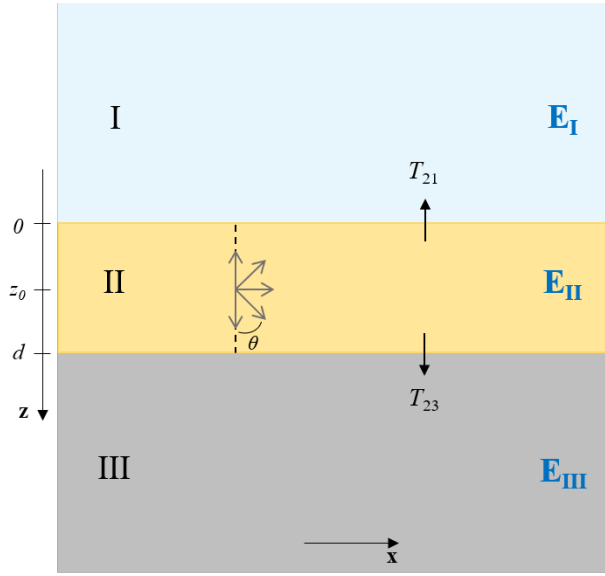
Figure 3.5: Schematic representation of the model considered to estimate the maximum current density in BVO photoanodes.

obviate any discussion on the nano-structuration that one may need to implement on the BVO or surrounding materials to achieve such kind of light propagation. The goal here is just to obtain an upper limit for the current density when excitation below the bandgap is properly accounted for.

To consider the propagation from the set of plane waves described above, we use the transfer matrix formalism introduced in Section 1.5.1. The total electric field at a given medium j is given by the superposition of all angular components, such that

$$\mathbf{E}_j = \int \frac{dk_x}{k_{2z}} \, \mathbf{E}_j(\theta) = E_0 \int \frac{dk_x}{k_{2z}} \, \mathrm{e}^{\mathrm{i}k_x x} \left[\beta_j^+ \left(k_x \right) \mathrm{e}^{\mathrm{i}k_{jz} z} + \beta_j^- \left(k_x \right) \mathrm{e}^{-\mathrm{i}k_{jz} z} \right], \quad (3.2)$$

where k_x is the x component of the wavevector and k_{jz} is the z component of the same wavevector at layer j, while $\beta_j^+ \left(k_x \right)$ and $\beta_j^- \left(k_x \right)$ determine in layer j the fraction of the electric field amplitude propagating in the z- positive and negative directions, respectively.

The time average flux of the electromagnetic field in the z direction at any x position is given by the Poynting vector, $\langle S_j(t) \rangle_z$, while the total flux flowing from $0 \leq x \leq L$ is obtained by the integration of $\langle S_j(t) \rangle_z$ over such an interval.

By calculating the ratio between the total fluxes entering and leaving a given medium, it is possible to obtain the electromagnetic field transmitted from the BVO layer to medium I, T_{21}, and to medium III, T_{23}. Considering that there are no other loss sources, the total electromagnetic field absorption in a portion of the BVO with length L is

$$A = 1 - T_{21} - T_{23}. \tag{3.3}$$

Finally, from such absorption, it is possible to calculate the current density generated by the BVO photoanode, by direct application of equation (1.1).
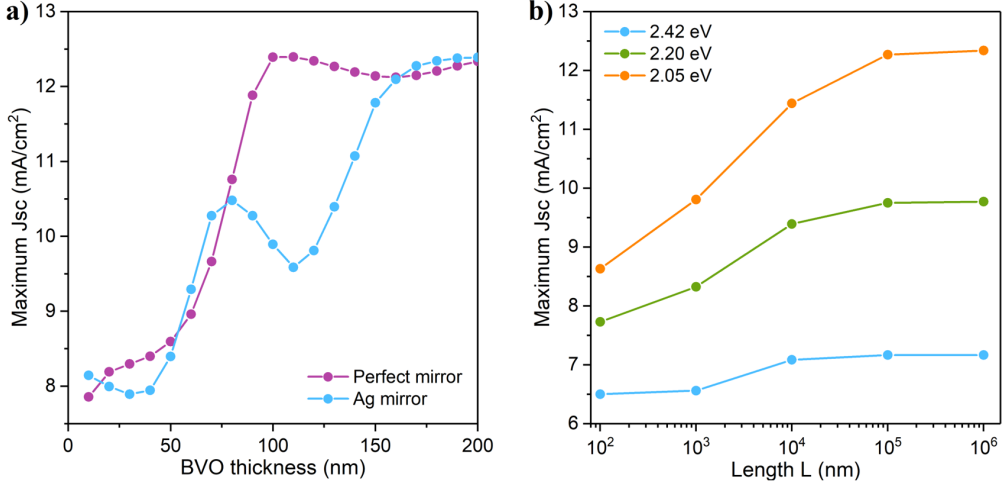

Figure 3.6: a) Maximum J_{sc} calculated as a function of the thickness of the BVO active layer, for the cases where the final medium is either a perfect mirror or a silver mirror. b) Maximum J_{sc} calculated as a function of the lateral dimension, L, for different cutoff energies. A 200 nm thick BVO active layer was considered to be enclosed between water and a semi-infinite silver mirror.

In a numerical application to determine the maximum achievable J_{sc}, we assumed an infinitely long BVO in the x-direction. As seen in Figure 3.6 a), when the BVO thickness in the z-direction is increased and layer III is a perfect mirror, the J_{sc} saturates approximately to 12.4 mA/cm^2 when such BVO thickness exceeds 100 nm. If instead of using a perfect mirror, layer III is an Ag mirror, the J_{sc} saturates roughly to the same value but after the BVO thickness exceeds 150 nm. This J_{sc} is considerably higher than the 7.5 mA/cm^2 currently reported in the literature,[176–178] emphasizing the importance of accounting for the contribution to J_{sc} from below-bandgap excitation to properly estimate the maximum photocurrent that can be extracted from BVO photoanodes. For this latter case, where the bandgap is assumed at 2.42 eV, when applying the model from this subsection to a finite length L in the x-direction, the J_{sc} saturates slightly above 7 mA/cm^2, when L exceeds 100 µm, as seen in Figure 3.6 b). When including excitation below the bandgap, setting a threshold at 2.20 eV where an excellent fitting of the EQE spectra was obtained, the J_{sc} saturates at 9.7 mA/cm^2. Finally, for the case where conversion of light into current is considered to begin at 2.05 eV, the lowest energy for which current is experimentally detected in our setup, the J_{sc} saturates to 12.3 mA/cm^2 when the length L is larger than 100 µm.

3.2.2   Introduce 3-D structures for enhanced current density

From the previous subsection, we conclude that the contribution to the J_{sc} from excitation below the bandgap may be very relevant and lead to photocurrents in BVO photoanode almost doubling the currently accepted maximum. However, this would require a very effective mechanism to deviate the light propagation from the incident direction perpendicular to the layer to a direction along the large dimension of such a layer. To achieve this deviation by light scattering, we first considered, as seen in Figure 3.7 a), incorporating a periodic array of 3-dimensional scatterers shaped as cylinders of radius r, height h, and separation w. To allow for an efficient water-splitting reaction, we limited the surface area covered by such scatterers to less than 40%.
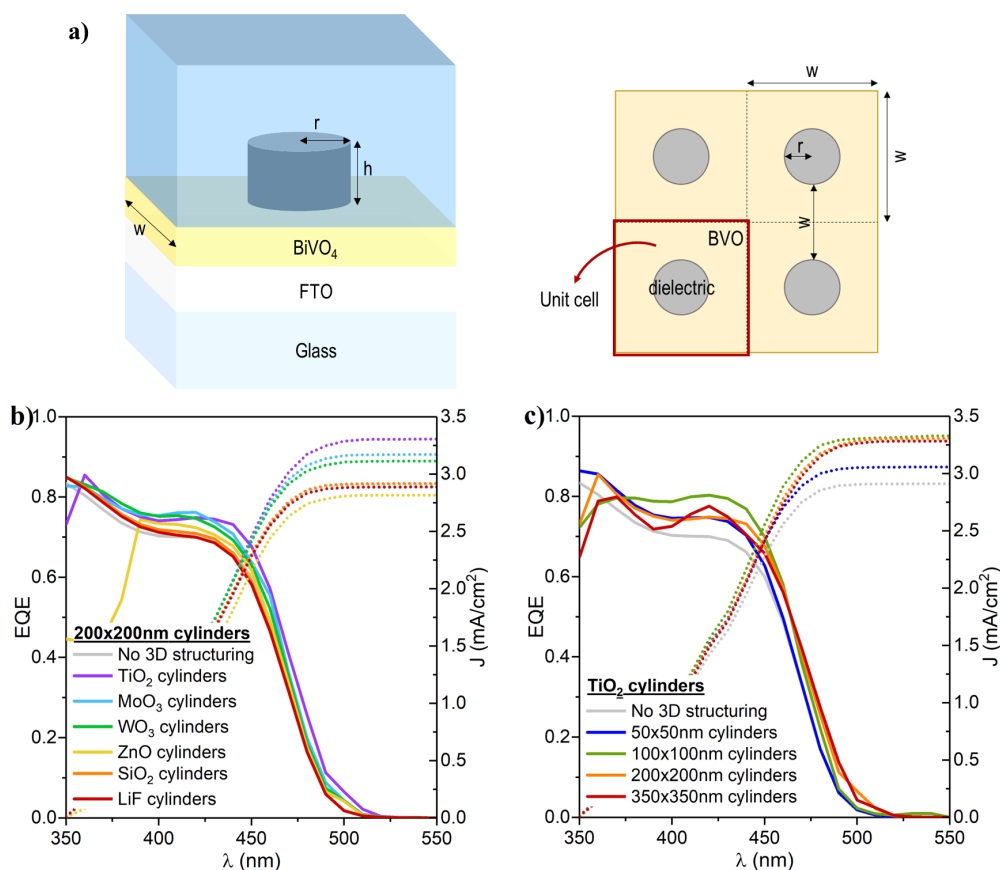

Figure 3.7: a) Side view (left) and top view (right) of a BVO photoanode incorporating an array of 3-D cylindrical scatterers on its top surface. The images are not at scale. b), c) EQE and J_{sc} calculated for a BVO photoanode covered by cylindrical scatterers as a function of b) the material used or c) the cylinder dimensions considered. In both cases, the results are compared with the response of a planar photoanode with the same layer configuration but without the introduction of any 3-D scattering array. The dimensions indicated in the legends of b) and c) correspond to the radius and height of the cylinders studied.
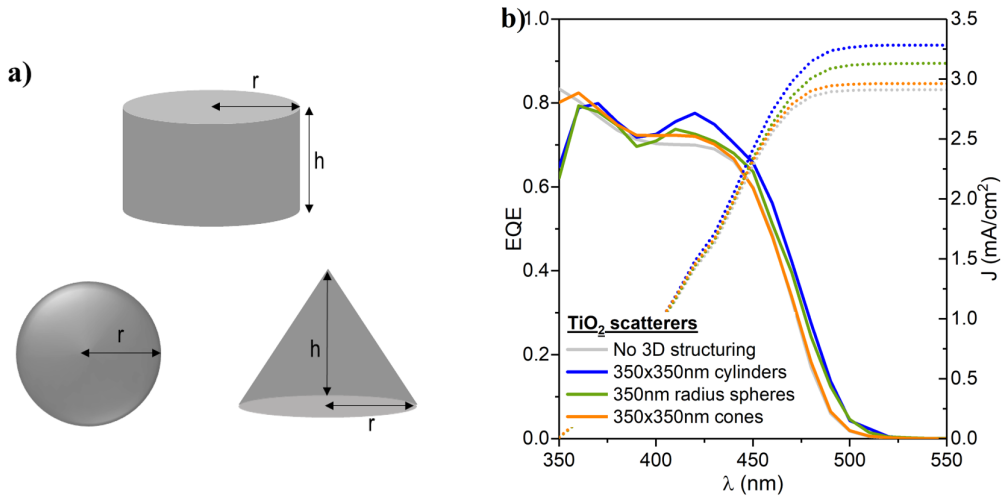
Figure 3.8: a) Different geometries of the scatterers considered in this thesis, which include cylindrical, spherical, and conical shapes, with indication of their main dimensions, r and h. b) EQE and J_{sc} of a BVO photoanode incorporating an array of TiO$_2$ scatterers of different geometries, with 350 nm of radius and 350 nm of height (when applicable), in comparison to the results obtained for planar photoanodes with the same layer configuration.

To computationally solve the 3-D Maxwell equations describing the electromagnetic field propagation in such a system incorporating an array of scatterers, a finite element method was employed through the use of COMSOL Multiphysics® software.[179] The results obtained when considering scattering elements of different dielectric materials, dimensions and shapes are presented in Figure 3.7 and Figure 3.8. As shown in Figure 3.7 b), when the material used for the cylinder exhibited a higher refractive index contrast relative to the electrolyte (see Appendix A), the 3-D scattering structure provided a more significant enhancement in the EQE and J_{sc} of the BVO photoanode. As we expected, this can be attributed to a more effective scattering of the incoming light due to the highest index contrast existent between the cylinder and the incident medium. Based on this, TiO$_2$ appears to be the most suitable material to employ for the scatterers. According to the results of Figure 3.7 c), small TiO$_2$ cylinders show a good capability to enhance light absorption between about 350 nm and 475 nm, but they fail to bring significant improvement in the region where the BVO absorption drops. In contrast, larger cylinders can ensure broadband EQE enhancement, including the bandgap region, with an apparent redshift of the absorption edge observed when the radius and height of the cylinders are either 200 nm or 350 nm. Such an array of big cylinders was the one that ultimately provided higher enhancements in the EQE and J_{sc} of the BVO. The use of spherical or conical scatterers, shown in Figure 3.8 a), with similar dimensions did not bring any significant increase with respect to the cylindrical scatterers, as can be seen in Figure 3.8 b).

3.3 Conclusions

This chapter aimed to explore the light absorption and conversion limits of BVO photoanodes for the water-splitting reaction, through high-sensitivity EQE measurements.

These measurements, performed with and without the presence of a highly reflective silver mirror on the back of the glass substrate, allowed us to resolve very accurately the EQE in the region close to and right below the bandgap of the BVO, from which it was possible to determine with high precision the effective refractive indexes of this material. This was done by modeling light propagation inside the planar photoanode, using a transfer matrix method, and by minimizing the differences between the experimental and simulated EQE spectra, through the use of a least mean squares algorithm.

By taking into account the photocurrent generation observed for energies below the bandgap of the BVO, it was possible to estimate the upper limit for the J_{sc} achievable from this material. To do so, we developed a simple model that considers the effective refractive indexes determined for the different materials, as well as the thickness of the BVO layer, to estimate the photocurrent limit that can be produced by BVO photoanodes when performing the water-splitting reaction. In this regard, current densities of about 12.3 mA/cm^2 were obtained, provided the lateral dimension of the BVO layer is 100 μm or larger, a J_{sc} which is significantly higher than the 7.5 mA/cm^2 currently reported in the literature. To reach such a limit, an effective light scattering and trapping inside the BVO active layer is needed, to maximize light absorption and conversion. The introduction of a periodic array of scatterers with simple geometries led to an enhancement of the EQE of the BVO in the vicinity of the bandgap, but the current densities obtained are still far from the limit. The results from such a preliminary study are a good indication that a route based on introducing scatters may be adequate. However, more powerful approaches, such as inverse design techniques involving the solution to the 3-dimensional Maxwell equations, might be needed to find configurations capable of bringing the J_{sc} closer to the estimated limit.

4

Optimization of BVO-OPV tandem devices

As a first step to approach a highly efficient unassisted water-splitting reaction, in the present chapter we consider the modeling, optimization and assembly of compact tandem PEC devices incorporating a highly transparent BVO photoanode studied in Chapter 3 together with an OPV cell based on a PM6:Y6 polymer with a low bandgap of about 1.3 eV. Such bandgap is selected because it was previously demonstrated to be the theoretically ideal one to achieve maximum STH conversion efficiency in systems that are composed of two distinctive light absorbing elements in a tandem configuration.[75,83–85] To properly balance light absorption among both elements, according to their respective light absorption profiles, an inverse design approach will be applied to determine the optimal configuration of a planar dielectric multilayer (ML) structure introduced in between the BVO and the OPV cell.

4.1   Modeling the optimal bias-free performance of the tandem

To obtain a compact tandem PEC device where a high bias-free STH conversion efficiency can be achieved, in this thesis we propose the design and implementation of a tandem configuration incorporating a highly transparent BVO photoanode and a PM6:Y6-based OPV cell that has a complementary absorption profile to the one of the BVO, as shown in Figure 4.1 a). To achieve an optimal light distribution among the different elements of the tandem and to enhance the limited current density that can be obtained from the BVO layer due to its small thickness, the conventional ITO used in OPV solar cells was replaced by a thin Ag layer as the electrode facing the BVO photoanode. This silver electrode was combined with a dielectric multilayer structure, placed in between the photoanode and the PM6:Y6 photovoltaic cell, as illustrated in Figure 4.1 b), to provide an adequate light distribution among both elements in the tandem.

To find the optimal ML+OPV(Ag) configuration, in terms of the number of layers, material combinations, and thicknesses for these layers, an inverse design approach was
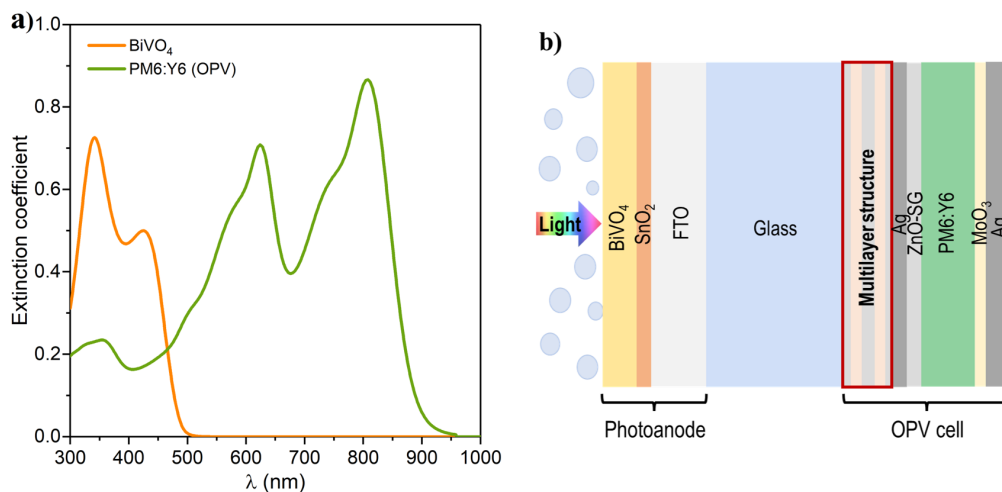
Figure 4.1: a) Comparison between the extinction coefficients of the BVO and of the PM6:Y6 organic polymer. b) Schematic illustration of the compact tandem devices considered in this thesis, which consist of a front BVO photoanode deposited on a SnO_2/FTO/glass substrate and of a back PM6:Y6-based OPV cell fabricated on top of a multilayer structure covered by thin silver.

employed using a genetic algorithm, described in detail in the introduction of this thesis and available at MATLAB®,[137] with the objective of maximizing the bias-free current density flowing through the tandem device. Provided the rather limited *J-V* performance of the BVO photoanode when compared to the OPV cell, illustrated in Figure 4.2 a), and to prevent operation of the tandem in the region where the *J-V* curve of the OPV bends, the above mentioned inverse design approach was implemented in a computational model that combines the general transfer matrix formalism, for the computation of the short circuit current densities, with a diode approximation to describe the *J-V* characteristics of both elements in the tandem.[77, 180–182] A complete description of the model used, together with the experimental relationships found between the electrical parameters for both photoanode and OPV cell can be found in Appendix C.

Among the different combinations of dielectric materials considered in the computation of the ML when applying the inverse design approach, it was found that the highest bias-free current density would be achieved when intercalating TiO_2 and SiO_2, as they show the highest contrast in the refractive index. This is illustrated in Figure 4.2 b), where it is clearly visible that the other two combinations considered, MoO_3/LiF and TiO_2/ZnO, exhibited a lower performance. Here, it may be noted that the material combinations chosen were limited to materials that can be deposited by the same physical deposition method, to reduce the fabrication complexity: MoO_3 and LiF are both deposited by thermal evaporation, while TiO_2, SiO_2, and ZnO are all deposited by magnetron sputtering.
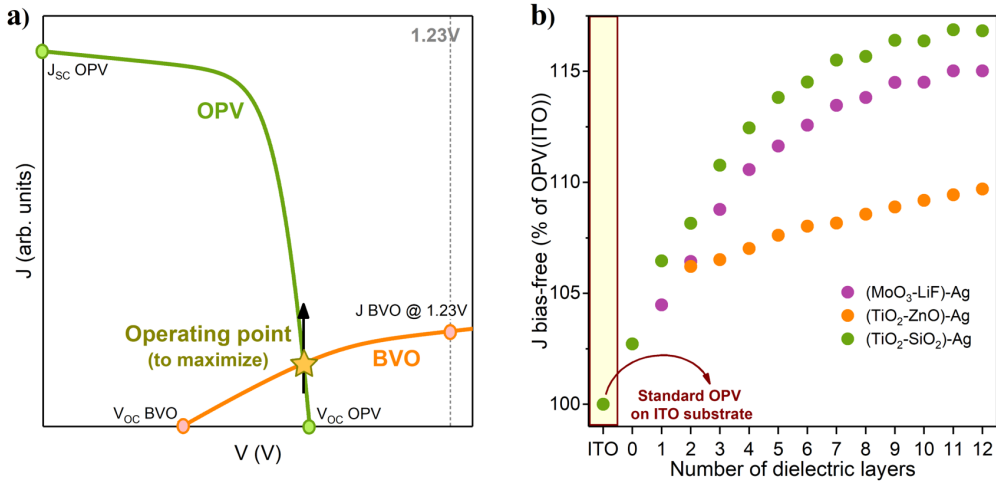
Figure 4.2: a) Schematic representation of the *J-V* curves of a BVO photoanode (orange) and of an OPV cell (green). The point where both curves intersect (signaled with a star) relates to the bias-free performance of the tandem device and was considered as the target to maximize by the inverse design approach. b) Predicted increase in bias-free current density of the tandem device with the number of dielectric layers in the multilayer structure, for a different combination of dielectric materials. The ITO cell with no ML, OPV(ITO), is considered as reference, so the values presented correspond to the percentage increases in bias-free current density comparatively to the OPV(ITO) tandem device.

In the simulations, the FTO and BVO layer thicknesses were kept fixed to the experimentally determined values, of 600 nm and 90 nm, respectively, while the SnO_2 layer was not included in the computation due to its negligible optical role. To limit charge recombination and to prevent large losses in charge collection in the OPV cell, its active layer was allowed to have a maximum thickness of 120 nm,[183] while to maintain a high conductivity for the front electrode of that same cell, the minimum thickness of the Ag was set to 7 nm.[47,48] The refractive indexes used for the BVO are the ones determined in Chapter 3, while the indexes of all other materials are plotted in Appendix A.

As demonstrated in Figure 4.2 b), for the optimal combination of TiO_2 and SiO_2, $J_{bias-free}$ tends to saturate as the number of layers in the ML increases, and only small gains are achieved beyond the 8-layer ML. When the ML+OPV(Ag) tandems are compared to a tandem incorporating an ITO-based OPV cell, OPV(ITO), the maximum predicted gain is close to 20%.

Table 4.1 shows the optimal configurations found for a set of ML+OPV photovoltaic cells with different numbers of layers in the ML, together with the nomenclatures used to identify them. As seen in the table, the inverse design approach led to MLs that deviate from the periodic $\lambda/4$ configuration to better distribute the light within the tandem device, by simultaneously enhancing reflectivity and transparency for wavelengths within the BVO and PM6:Y6 absorption bands, respectively.

Table 4.1: Optimal configurations obtained for different multilayer structures. The layers of the OPV cell in all cases are ZnO-SG(10nm)/PM6:Y6/MoO$_3$(5nm)/Ag(100nm).

Sample name	ML+OPV electrode	PM6:Y6 thickness
OPV(ITO)	ITO(135nm)	100nm
OPV(Ag)	Ag(10nm)	110nm
ML1+OPV(Ag)	TiO$_2$(58nm)/Ag(14nm)	119nm
ML2+OPV(Ag)	TiO$_2$(40nm)/SiO$_2$(37nm)/Ag(9nm)	113nm
ML4+OPV(Ag)	TiO$_2$(40nm)/SiO$_2$(74nm)/TiO$_2$(41nm)/SiO$_2$(44nm)/Ag(7nm)	112nm
ML8+OPV(Ag)	TiO$_2$(33nm)/SiO$_2$(74nm)/TiO$_2$(40nm)/SiO$_2$(74nm)/ TiO$_2$(42nm)/SiO$_2$(81nm)/TiO$_2$(43nm)/SiO$_2$(32nm)/Ag(7nm)	109nm

4.2   Experimental fabrication of the multilayer structures

Multilayer structures with the configurations indicated in Table 4.1 were fabricated on top of Eagle XG glass substrates by reactive magnetron sputtering, using Ti and n-type Si targets, and O$_2$ as reactive gas. This method allowed for the deposition of very flat layers, as demonstrated in the cross-section SEM micrograph of Figure 4.3 a), with optical properties that strongly depend on the number of dielectric layers deposited, as evidenced by the color shift towards orange clearly visible at naked eye and seen in Figure 4.3 b).

All five ML structures fabricated were covered by very thin Ag layers, ranging from 7 nm to 14 nm, which served as electrodes for the OPV cells. To achieve a high optical and electrical quality for this thin silver, a small flux of oxygen was added during its deposition, by magnetron sputtering, to facilitate the uniform and continuous growth of such an ultrathin layer.[48] In addition, two very thin ($\sim$ 5 nm) ZnO layers were introduced, below and above the silver. While the first played the role of flattening the roughness and increasing the wettability of the TiO$_2$/SiO$_2$ surfaces, the latter was added to prevent any degradation when in contact with the air or the organic materials of the OPV cell.[47] Despite these many beneficial effects, such layers do not play any relevant optical role and therefore they do not affect the final performance of the tandem devices. As a result, sheet resistances ranging between 9.3 Ω/sq and 23.5 Ω/sq, and comparable to the one of the commercial ITO-covered substrates, were measured for the thin and semi-transparent silver layers deposited on top of the different dielectric multilayers, as shown in Figure 4.3 c).
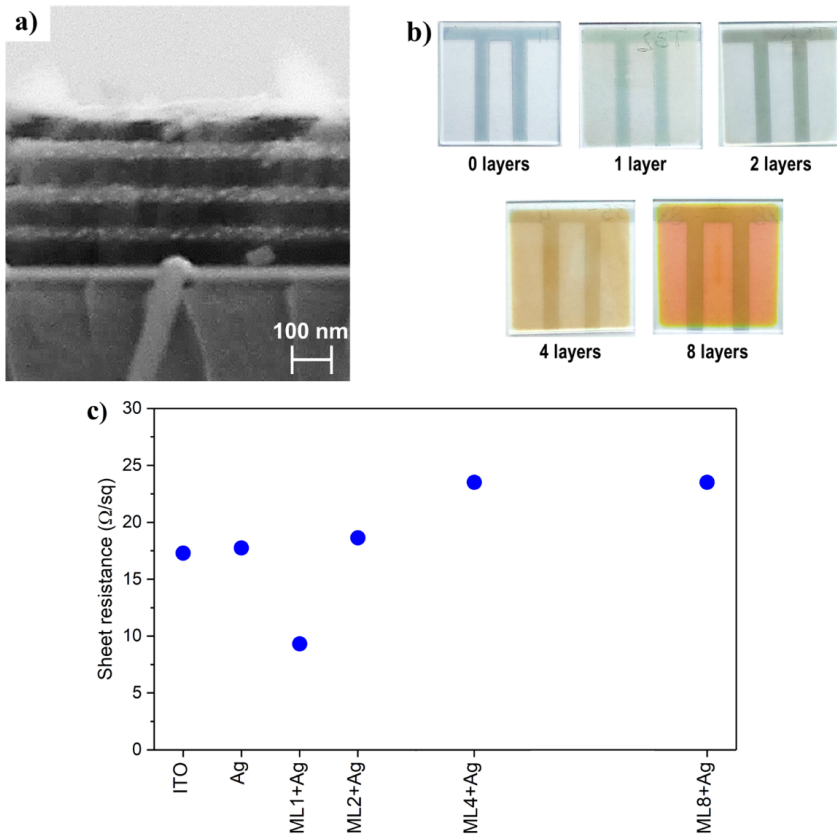
Figure 4.3: a) Cross-section SEM of a ML structure containing 8 dielectric layers. b) Photographs of the ML structures with different numbers of dielectric layers, covered by the (striped) thin silver, where a clear change in color is visible with the variation in the number of dielectric layers. c) Sheet resistance measured for the different Ag electrodes used for the OPV cells, in comparison to the standard commercial ITO. These measurements were performed on fully covered substrates with dimensions 2.5 cm × 2.5 cm.

4.2.1 Performance of the OPV cells deposited on different multilayers

OPV cells with ZnO-SG(10nm)/PM6:Y6/MoO$_3$(5nm)/Ag(100nm) configuration and variable active layer thickness were deposited on top of all electrodes, following the method described in the literature.[184] Experimentally measured reflectances are shown in Figure 4.4 a). According to the results, in the low wavelength region where the BVO absorbs, the reflectivities can be seen to broaden and to increase gradually up to above 90% as the number of layers in the ML increases, while they are roughly maintained in a 10% to 40% range in the spectral region where the OPV cell is expected to contribute. Note the measured reflectances are in very good agreement with the numerical predictions shown in Figure 4.4 b). The light with lower wavelengths that is not ini-

tially absorbed by the thin BVO ends up being strongly reflected by the ML+OPV(Ag) cell. When the number of layers in the such ML is high, the effective absorption length in the photoanode doubles. On the contrary, the light with higher wavelengths is very weakly reflected regardless of the ML structure considered, being instead absorbed in the PM6:Y6 active layer of the OPV.
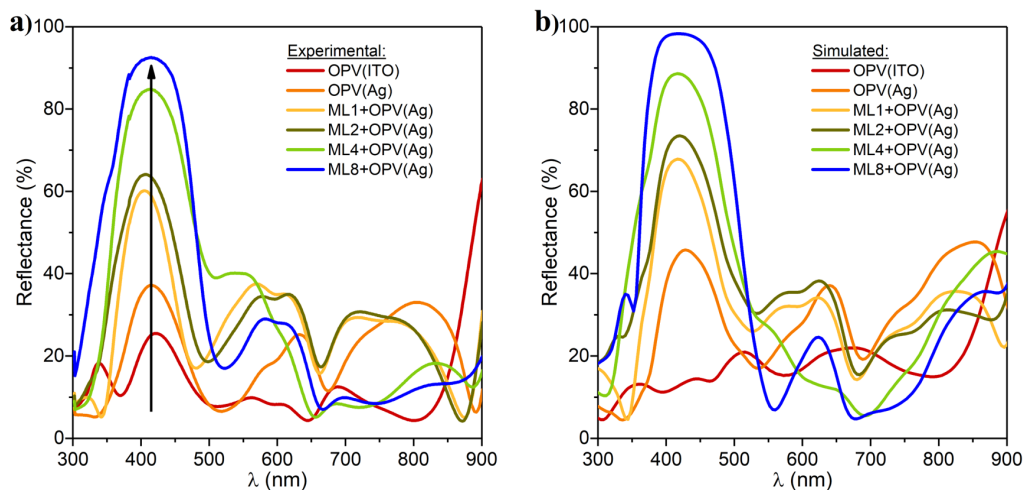

Figure 4.4: a) Experimental and b) simulated reflectance spectra of the OPV(Ag) cells deposited on top of different multilayer structures. A strong increase in reflectance between 400 nm and 450 nm is observed as the number of dielectric layers increases and is signalled by an arrow in a).
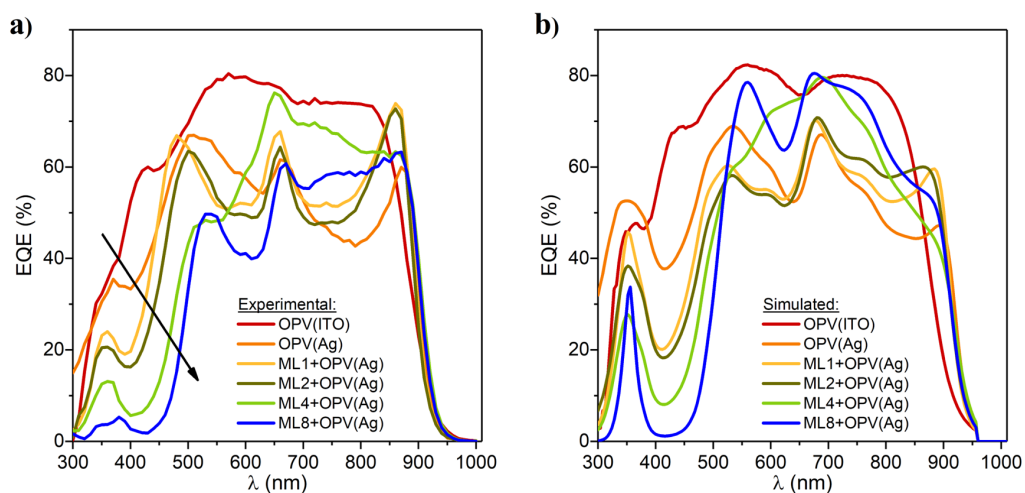

Figure 4.5: a) Experimental and b) simulated EQE spectra of the OPV cells deposited on top of different multilayer structures.

The changes in optical reflectance reported in Figures 4.4 a) and b) for the OPV cells with varying numbers of layers in the ML have a clear effect on the EQE of these OPV cells, as illustrated in Figure 4.5. As clearly observed, for the ML8-based structure, the EQE of the OPV is practically zero in the spectral region ranging from 300 to 450 nm. When the number of layers in the ML is increased, the UV side of the EQE of the OPV is reduced as predicted by the theoretical computation of the EQEs shown in Figure 4.5 b). Correspondingly, the resulting J_{sc} decreases as seen in Figure 4.6 and Table 4.2. The J_{sc} for the OPV cell still remains much larger than the one from the photoanode, so there is a negligible negative effect on the OPV when the ML is used.
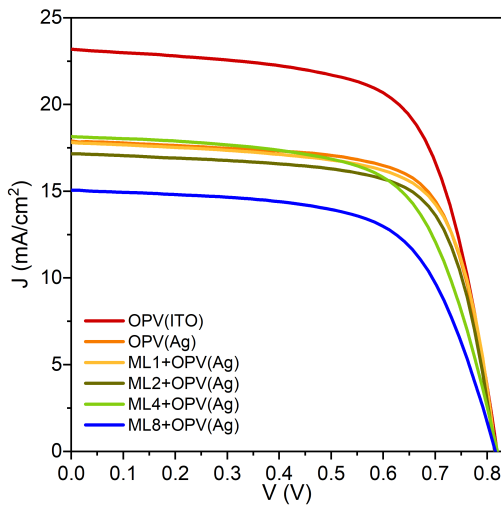

Figure 4.6: *J-V* curves of the OPV cells deposited on top of different multilayer structures.

The *J-V* response of the OPV cells deposited on ML structures with a varying number of dielectric layers is plotted in Figure 4.6, while the main photovoltaic parameters are presented in Table 4.2. According to the results, some variations in J_{sc} are observed for the different samples, which are explained by the changes in EQE previously reported. No consistent decrease in the V_{oc} is observed as the number of layers in the ML increases. A larger change is seen in the FF, which for the ML8+OPV(Ag) sample is reduced down to 63.6% relative to the 71% FF of the OPV(Ag) cell without the ML, that is deposited directly onto the glass substrate. In the tandem operation this will imply that the operating point shown in Figure 4.2 a) is slightly shifted to lower potentials.

Table 4.2: Photovoltaic parameters of the PM6:Y6 solar cells prepared on top of the different ML.

Sample name	J_{sc} (mA/cm^2)	V_{oc} (mV)	FF (%)	PCE (%)
OPV(ITO)	23.18	819	66.4	12.61
OPV(Ag)	17.90	815	71.0	10.36
ML1+OPV(Ag)	17.82	815	70.1	10.18
ML2+OPV(Ag)	17.16	814	70.3	9.82
ML4+OPV(Ag)	18.16	819	64.2	9.55
ML8+OPV(Ag)	15.07	816	63.6	7.82

4.2.2 Performance of the BVO in front of the different OPV cells

The BVO photoanodes described and used in Chapter 3 were also employed here when assembling the tandem PEC devices. To investigate the role of the different ML structures and their capacity to enhance the J_{sc} (current density at 1.23 V$_{RHE}$) extracted from the photoanode, which is what actually sets the limit performance for the bias-free PEC, the same BVO photoanode was placed in front of the different electrode-OPV cells and its photoelectrochemical response was assessed. To clearly separate the ML contribution to the J_{sc} enhancement from a more or less effective catalysis, these experiments were performed using a pH 9 electrolyte solution of 1.0 M KBi with 0.2 M of an SO$_3^-$ hole scavenger. The results obtained for the EQE spectra of the BVO at 1.23 V$_{RHE}$ and for the J-V response of the photoanode are plotted in Figure 4.7 a) and c), respectively.

As observed, the experimentally measured EQEs are progressively enhanced in the mid to long wavelength side of the BVO absorption band and apparently infrared shifted, as the number of TiO$_2$/SiO$_2$ bi-layers increases, in agreement with the predicted behavior simulated and shown in Figure 4.7 b). This apparent IR shift of the EQE clearly indicates that the conversion of absorbed photons to collected holes to feed the hydrogen evolution reaction has not reached its limits in BVO-based PECs, as discussed in Chapter 3. On the other hand, there is a clear saturation of the EQE on the short wavelength side, even when the number of layers in the ML is small, which results from a short exciton diffusion and low minority carrier mobility in the BVO, indicating that the main limitation in this low wavelength range is the poor electrical performance of photoanode instead of a deficient light absorption, as also observed in Chapter 3.

When the number of layers in the ML approaches its maximum, the saturation in the EQE spectra extends to longer wavelengths, which proves that the light absorption enhancement provided by the multilayer structure is very effective, even when BVO layers less than 100 nm thick are being used. This saturation in the light absorption is in agreement with the increase and subsequent saturation of the reflectance of the ML+OPV(Ag) observed in Figure 4.4 when the number of layers in the multilayer structure approaches
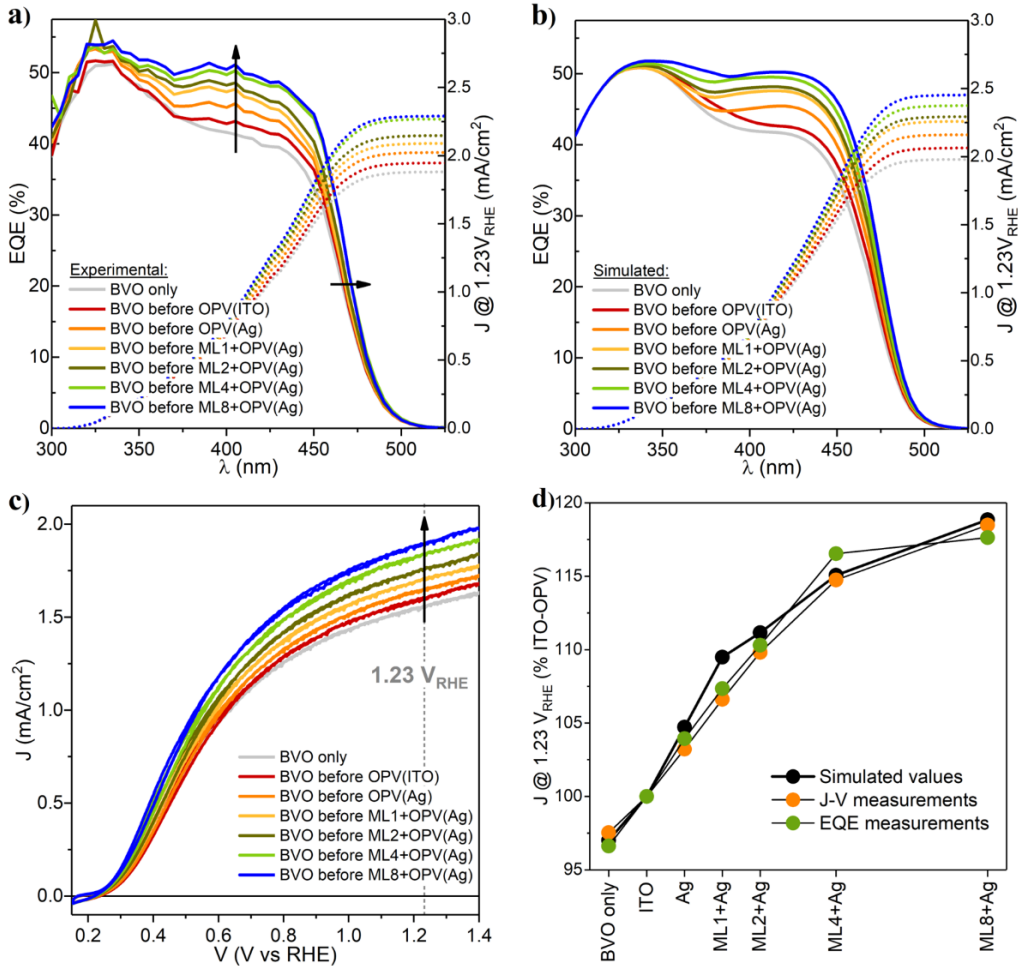
Figure 4.7: a) Experimental and b) simulated EQE spectra of the BVO photoanode when placed in front of different ML+OPV(Ag) cells, measured at 1.23 V_{RHE}. c) Current density as a function of the voltage in reversible hydrogen electrode, RHE, scale (details in Appendix B) for the photoanode placed in front of different OPV cells with varying number of layers in the ML. d) Percentual change in the photoanode J_{sc} when placed before the different ML+OPV(Ag) solar cells, in comparison with the theoretical predictions.

eight, and clearly demonstrates the importance of the inverse design considered in the current thesis to find optimal configurations that bring the light absorption in tandem PEC devices towards its maximum limit.

The increase in BVO light absorption with the number of layers in the ML is directly translated to a better photocatalytic performance of the photoanode, as demonstrated by the *J-V* responses of Figure 4.7 c). A sequential enhancement in the J_{sc} of the photoanode with the number of dielectric layers is demonstrated, in agreement with the current density enhancement obtained from the integration of the experimental EQE spectra of Figure 4.7 a). For both cases, the percentual increase in the photoanode J_{sc} in comparison to the use of a standard OPV(ITO) solar cell was in good agreement with the computational predictions, as seen in Figure 4.7 d) and Table 4.3, reaching almost 19% for the ML8-based structure.

Table 4.3: Current density of the photoanode at 1.23 V_{RHE}. Comparison of the experimental values obtained through the integration of the EQE and measured *J-V* response, to the simulated values. The photoanode placed in front of the OPV(ITO) solar cell is considered as the reference.

Sample name	Experimental J_{sc} change from EQE	Experimental J_{sc} change from *J-V*	Simulated J_{sc} change
OPV(ITO)	100.0	100.0	100.0
OPV(Ag)	103.9	103.2	104.7
ML1+OPV(Ag)	107.3	106.6	109.5
ML2+OPV(Ag)	110.3	109.8	111.2
ML4+OPV(Ag)	116.5	114.8	115.1
ML8+OPV(Ag)	117.6	118.5	118.9

4.3   Assembling of the tandem devices

Tandem devices were mounted at the back of the PEC cell, where the photoanode was in contact with the electrolyte solution and illuminated from the front side, while the OPV solar cell was placed outside. For the photoelectrochemical measurements, the BVO photoanode, the photovoltaic cell, and the cathode were connected in series, as shown in Figure 4.8. Additional technical details about the PEC cell used and the assembly of tandem devices can be found in Appendix B.

The *J-V* response of the device was evaluated by applying an external voltage to the PEC cell, both in the case where the electrical circuit was closed by the OPV cell, as shown in Figure 4.8, and when the OPV cell was electrically by-passed.
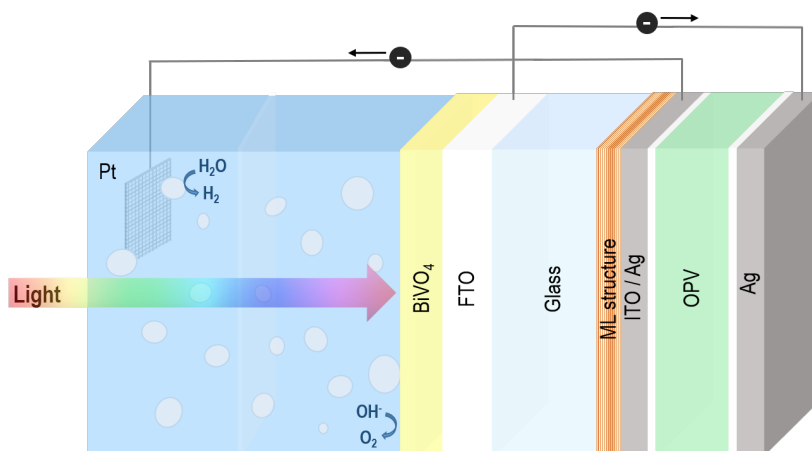
Figure 4.8: Schematic illustration of the tandem device experimentally assembled, consisting of a BVO photoanode, an OPV cell and a Pt mesh cathode connected in series by external cables.

4.3.1 Bias-free behavior for the water-splitting reaction

To properly measure the solar-to-hydrogen efficiency of the water splitting reaction for a photoelectrochemical tandem device exposed to an AM1.5G illumination under zero bias conditions, a 2-electrode configuration must be used and the electrolyte solution should not contain any hole scavengers.[78, 185, 186] For this reason, tandem devices comprising OPV(ITO) or ML8+OPV(Ag) solar cells together with BVO photoanodes incorporating a FeOOH/NiOOH catalyst on their surfaces were tested as described in the previous section, using a pH 9 solution of 1.0 M KBi, in a 2-electrode system where the cathode used for the HER was a Pt mesh. To guarantee that the differences in performance observed for the tandem devices are due to a better distribution of the light, promoted by the multilayer structure, two BVO photoanodes with very similar J-V response were chosen for the assembly of the tandems, as illustrated in Figure 4.9.

The J-V response of the tandem devices was studied for the case where the photoanode, the OPV cell, and the Pt mesh were connected in series, as described in Figure 4.8, and compared to the case where the OPV cell was not electrically connected and only contributed to provide light reflectivity. The results obtained for both tandems are presented in Figure 4.10 a). As clearly observed, when the OPV were connected in series in between the photoanode and the cathode, the J-V curves were down shifted by approximately the open circuit voltage of the solar cells relative to the ones where the OPV were not connected. This shift was kept practically unaltered regardless of the photocurrent generated, which indicates that the photovoltaic cells are not limiting the performance of the tandem for any of the configurations studied. As depicted in Figure 4.6 and Table 4.2, the high-performing parameters of the PM6:Y6 OPV cells used to assemble the tandem devices guarantee that the potential J_{sc} obtainable from both cells is several times higher than the one provided by the photoanodes, while the V_{oc} and fill factor remain quite high
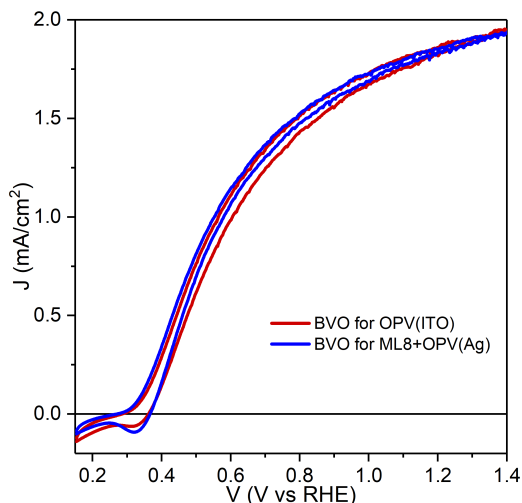
Figure 4.9: *J-V* curves of the BVO photoanodes scanned in the forward and reverse direction before using the BVO for the tandem assemblies with OPV(ITO) and with ML8+OPV(Ag) solar cells, illustrating how similar the behavior of the photoanodes chosen is initially. The difference in photocurrent for a given potential was always lower than 0.1 mA/cm^2.

with the addition of the ML structure, which explains why in both cases the *J-V* behavior of the tandem is not affected by the performance of the OPV cell.

At 0 V of applied voltage, a completely bias-free H$_2$ production is obtained, resulting in a photocurrent density increase from 1.26 mA/cm^2 for the photoanode/OPV(ITO) to 1.57 mA/cm^2 for the photoanode/ML8+OPV(Ag) tandem, which represents a 25% increase in $J_{bias-free}$ when an 8-layer ML is combined with an OPV incorporating a transparent Ag electrode. These results are supported by the changes observed in the crossing point between the individual *J-V* responses of the photoanode and the PV cell in a tandem assembly, shown in Figure 4.10 b), which is related to the bias-free operating point. As observed, an increase in current density at the crossing point is obtained when the ML8+OPV(Ag) solar cell is considered, due to the reflective character of the ML+OPV structure used, while the voltage only suffers a minimal shift towards lower values. This confirms that a proper distribution of the light absorption among the two sides of the tandem is key in the implementation of an efficient bias-free STH conversion.

Further confirmation of the relevance of a proper distribution of the light in terms of the wavelength to match the absorption bands of the different elements of the tandem is seen in the EQE spectra shown in Figure 4.10 c). According to the data, the EQE of the photoanode is enhanced in a wavelength range spanning almost the entire absorption band of the BVO, while the EQE of the OPV is correspondingly reduced in the UV side, but is clearly less affected in the IR side of the absorption band, to ensure a sufficiently high current in the photovoltaic cell to effectively perform the bias-free water splitting reaction.
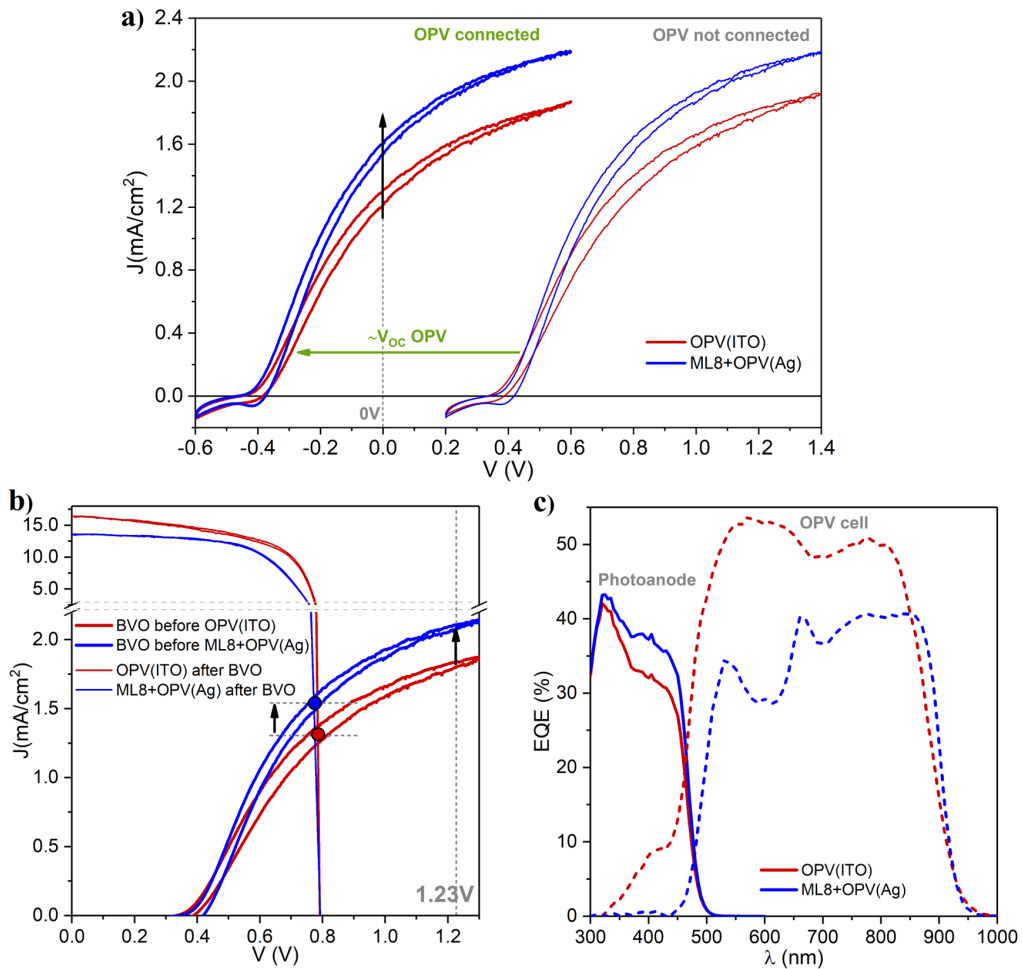
Figure 4.10: a) *J-V* response of the photoanode/OPV(ITO) (in red) and of the photoanode/ML8+OPV(Ag) (in blue) tandems when the OPV cell is connected to the electrical circuit (curves on the left) and when it is electrically by-passed. b) *J-V* response of the OPV cells behind the BVO (thinner lines) and of the photoanodes placed in front of the OPV cells (thicker lines), for the cases where an OPV(ITO) and a ML8+OPV(Ag) solar cells were used. The crossing points between the two curves, related to the operating current density, are signaled by the colored bullet points. For both cases, the forward and reverse scans were plotted and the average curve was used to determine the crossing point. c) EQE spectra of the BVO and OPV individually measured when an external voltage was provided to simulate the bias-free conditions for the photoanode.

4.3.2 Hydrogen evolution

The hydrogen production for the two different tandem BVO-OPV devices was evaluated as described in Appendix B, using a PEC cell with a double compartment, separated by a transparent ion exchange membrane. From the amount of H_2 experimentally measured, faradaic efficiencies were determined as explained in Section 1.3.2.
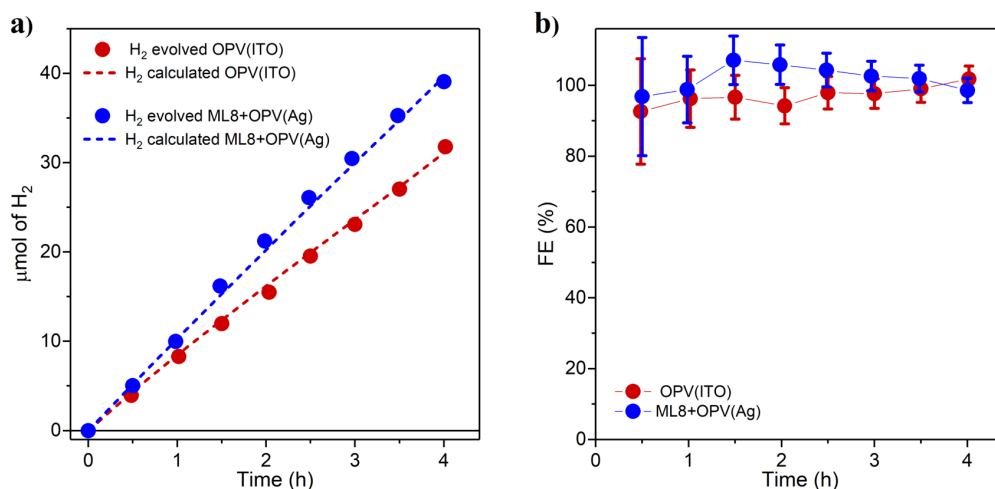
Figure 4.11: a) Experimentally measured H_2 production (closed circles), compared to the theoretical production rate (dashed lines), for the photoanode/OPV(ITO) (red) and for the photoanode/ML8+OPV(Ag) (blue) tandem devices and b) corresponding faradaic efficiencies.

The experimental measurements of the hydrogen evolution, shown in Figure 4.11 a), confirm an increase in gas production of about 25% when the 8-layer ML structure is used to improve light management, in strong agreement with the results from the previous section. These results are also in accordance with the H_2 production estimated from the bias-free current density measured during the gas evolution studies, assuming 100% FE, and which is represented by the dashed lines.

The faradaic efficiencies determined for both tandems were very close to 100%, corresponding to STH efficiencies of 1.55% and 1.93% for the photoanode/OPV(ITO) and the photoanode/8ML/OPV(Ag), respectively. Note that, at the beginning of the reaction, the error in the measurement of the FE is a bit large, as seen by the error bars in Figure 4.11 b), provided the volume readings for the very small amounts of produced hydrogen were not extremely precise.

4.3.3 Stability of the tandem devices

The stability of the different tandem devices was evaluated by carrying out long-term operation studies, for 12 hours, at bias-free conditions, using a single-compartment PEC cell, and considering the assembly illustrated in Figure 4.8.

The results are shown in Figure 4.12 a) and reveal that, in the first couple of hours, the photocurrent decreased quite fast until reaching nearly 60% of the initial value, after which it became stable for the remaining time of the study, with some oscillations attributed to the formation and release of bubbles.
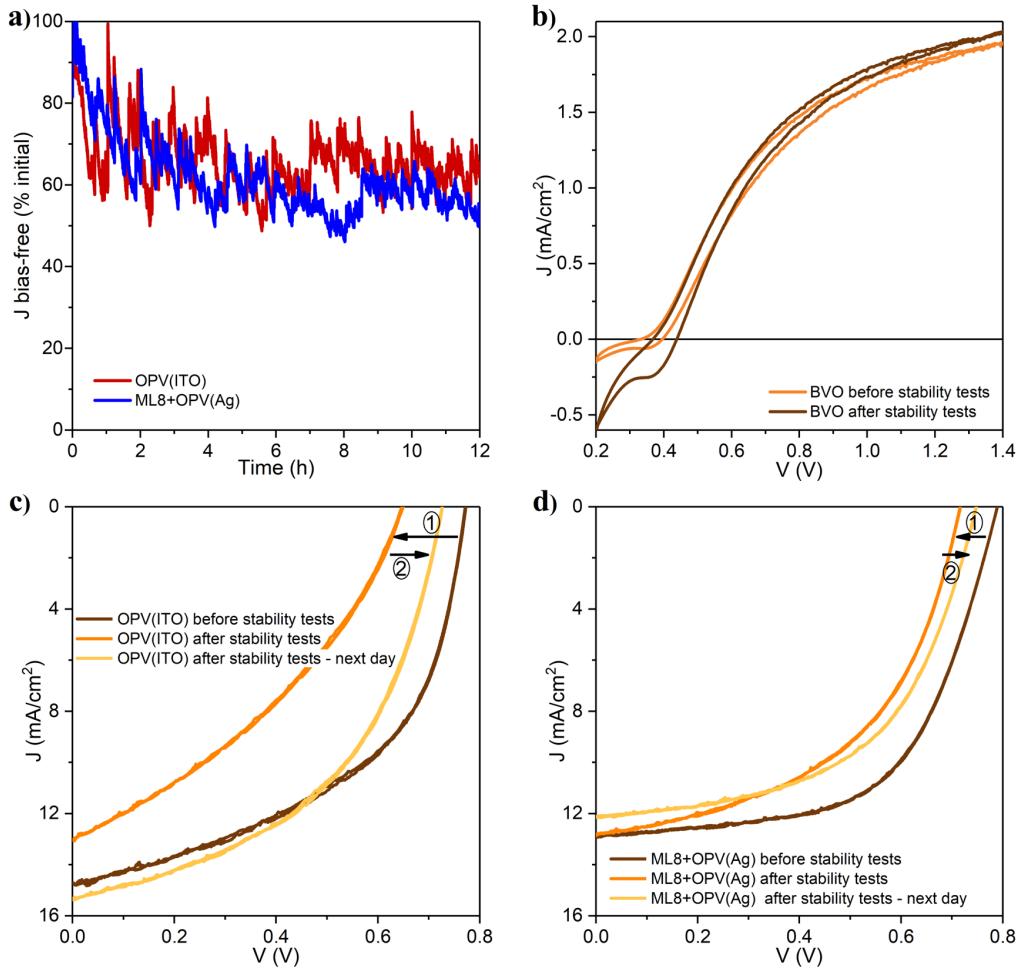
Figure 4.12: a) Long-term operation studies, carried out for 12 hours at bias-free conditions, of the photoanode/OPV(ITO) (in red) and of the photoanode/ML8+OPV(Ag) (in blue) tandem devices. b) *J-V* response of the BVO photoanode measured before and after the 12-hour long-term operation, which illustrates the small changes in performance that occurred during the stability studies. *J-V* behavior of the c) OPV(ITO) and d) ML8+OPV(Ag) solar cells before and after the long-term operation studies (1), showing the decrease in V_{oc} suffered, as well as the *J-V* curves measured after storing in dark for one day (2), emphasizing the partial recovery in V_{oc} observed.

An analysis of the BVO and OPV performances made right before and after these stability measurements, shown in Figure 4.12 b), c), and d), revealed that the photoanode is very stable and its response is largely unaffected after 12 hours of constant operation. On the other hand, the OPV cells under continuous illumination suffer a visible reduction in V_{oc} and FF, which are the main causes for the reduction in $J_{bias-free}$ observed in Figure 4.12 a). This happens irrespective of the OPV(ITO) or ML8+OPV(Ag) cell

configuration used. However, it is worth noting that part of this performance can be recovered after storing for one day in dark and dry conditions, as seen in Figure 4.12 c) and d).

4.4 Conclusions

From Chapter 3 we concluded that, to enhance the photocurrent in PEC devices incorporating a BVO photoanode, one must introduce any kind of light handling mechanism to increase the effective length for light absorption in the BVO. Although 3-dimensional configurations may eventually lead to a large light absorption enhancement and an effective reduction of the BVO bandgap, the nano-structuration that may lead to it needs further study. In contrast, optimal 1-dimensional nano-structures can be designed using an inverse integration approach. In this chapter, we implemented such 1-dimensional structures in tandem PEC cells combining high and low bandgap materials to achieve a water-splitting reaction using sunlight as the energy source. As the high bandgap element, a light dispersion-free BVO photoanode was implemented, while the low bandgap element considered was a PM6:Y6-based organic solar cell.

To accurately balance the light absorption among the two elements of the tandem according to their respective absorption profiles, the ITO electrode used in conventional OPV solar cells was replaced by thin silver, which was combined with a TiO_2/SiO_2 multilayer structure, placed in between the photoanode and the photovoltaic cell. An inverse design approach using a genetic algorithm was implemented to determine the optimal layer configuration for the ML structure, in order to maximize the bias-free current density flowing through the tandem device. To do so, a computational model that combines the general transfer matrix method for the J_{sc} calculation with a single-diode approximation to describe the J-V characteristics of both tandem elements, which takes into account the experimentally observed relationships between the electrical parameters of both the BVO photoanode and OPV cell, was considered.

From the theoretical predictions, an increase in bias-free performance of the tandem devices was expected with the increasing number of dielectric layers in the ML. This increase, experimentally observed, occurred mainly due to a very effective reflection of the light with low wavelengths back into the BVO photoanode, therefore improving its absorption and enhancing its photocurrent. In particular, by using an optimal 8-layer ML structure, a 25% increase in bias-free current density and in solar-to-hydrogen conversion efficiency were observed in comparison to the case employing a commercial ITO electrode for the OPV solar cell.

Chapter 5

Concluding remarks

The present thesis was dedicated to the modeling of light propagation and to the optimization of light transformation and utilization in different systems aiming for maximal energy efficiency. In particular, two different routes were explored to obtain optimal configurations, which included minimizing the light losses of devices incorporating light sources on them or maximizing the conversion efficiency of existent energy transformation systems. We demonstrated that the use of ergodic geometries and the search for configurations providing maximal light absorption are key to design energy-efficient devices.

In this regard, Chapter 2 focused on the design of a novel guiding structure for the emission of diffuse and polarized light, with an efficient conversion of the unwanted polarization back to electricity by means of PV cells. Such guide was designed based on the ergodic propagation of the light occurring inside a h-CPP, that was combined with a multilayer reflective polarizer, a highly reflective bottom element, and two PVK solar cells. An inverse design approach was used to optimize the configurations of the MRP and of the bottom reflector, to selectively transmit the desired p-polarization, while trapping and guiding the s-polarization component towards the PVK cells. As we demonstrate, this guide presents minimal energy losses and finds a potential application in LCD displays, that traditionally use absorbing polarizers to cut half of the incident radiation.

Chapter 3 approached the challenge of optimizing energy efficiency by exploring the limiting performance of BVO photoanodes for water-splitting applications. Through high-sensitivity EQE characterization, the absorption and conversion of light in the vicinity of the bandgap were probed with great precision, which allowed us to accurately compute the effective refractive indexes of the BVO, especially in the bandgap and below the bandgap spectral region. A simple model was developed to estimate the limiting current density attainable by these photoanodes, yielding values as high as 12.39 mA/cm^2. This stands well above the 7.5 mA/cm^2 currently reported in the literature and demonstrates the importance of accurate modeling the energy transformation systems to achieve limiting performances. To reach this maximal photocurrent density for BVO photoanodes, optimal trapping of the light inside the semiconductor layer is necessary. Initial studies involving the incorporation of periodic arrays of 3-dimensional scatterers with simpler

geometries helped on improving the EQE in the bandgap region but did not allowed for such a strong trapping of the light. Therefore, an inverse design approach involving the 3-D wave propagation in structured photoanodes is required to find optimal configurations, with non-trivial geometries, for maximized energy conversion.

Finally, Chapter 4 explored the use of the previously described BVO photoanodes for optimized sunlight-powered water splitting in planar tandem PEC devices. Such tandem devices incorporated OPV solar cells with complementary absorption to the one of the BVO, and different multilayer structures to manage light distribution among the tandem elements. By relying once again on an inverse design approach, the configuration of the ML structures was optimized to guarantee a balanced light absorption, towards optimal unassisted water splitting. Indeed, when using an optimized 8-layer ML structure, a 25% enhancement in bias-free current density and in hydrogen production was achieved for the tandem devices, approaching the highest performance attainable for planar configurations.

A

Refractive indexes

The wavelength-dependent complex refractive index of a medium, $n = n_{\mathrm{r}} + in_{\mathrm{i}}$, describes how the speed of light changes and how strongly the light is absorbed when it passes through such a medium. It provides important information about the optical bandgap and absorption coefficient and is necessary to fully describe the optical properties of the material.[187, 188] Therefore, accurate determination of the refractive indexes is crucial to model light propagation in optical devices.

Refractive indexes are usually obtained by measuring one or more optical properties of the material, such as transmittance, reflectance, or spectroscopic ellipsometry. Analytic expressions for the wavelength-dependent refractive index are obtained by fitting the experimental results using an appropriate dispersion relation, that describes the relationship between the wavelength (λ) or energy (E) of light and its velocity in the medium. This last depends on the refractive index of the material ($v = c/n$), which is related to the complex dielectric function, $\varepsilon = \varepsilon_{\mathrm{r}} + i\varepsilon_{\mathrm{i}}$, by[189, 190]

$$\begin{cases} n_{\mathrm{r}} = \sqrt{\dfrac{\sqrt{\varepsilon_{\mathrm{r}}{}^2 + \varepsilon_{\mathrm{i}}{}^2} + \varepsilon_{\mathrm{r}}}{2}} \\[4mm] n_{\mathrm{i}} = \sqrt{\dfrac{\sqrt{\varepsilon_{\mathrm{r}}{}^2 + \varepsilon_{\mathrm{i}}{}^2} - \varepsilon_{\mathrm{r}}}{2}} \end{cases}. \tag{A.1}$$

Since the refractive and absorptive properties of a material must be causally related to one another, the corresponding dielectric function should comply with the Kramers-Kronig relations, given by[190, 191]

$$\begin{cases} \varepsilon_{\mathrm{r}}(E) = 1 + \dfrac{2}{\pi} \mathcal{P} \displaystyle\int_0^\infty \dfrac{E' \varepsilon_{\mathrm{i}}(E')}{E'^2 - E^2} dE' \\[4mm] \varepsilon_{\mathrm{i}}(E) = -\dfrac{2E}{\pi} \mathcal{P} \displaystyle\int_0^\infty \dfrac{\varepsilon_{\mathrm{r}}(E') - 1}{E'^2 - E^2} dE' \end{cases}. \tag{A.2}$$

This means that only one of the components of ε needs to be determined to fully describe the optical properties of a material, by applying the principle of causality.

A.1   Dispersion relations

In this thesis, the refractive indexes of some semiconductor materials (FTO and BVO) were determined as described previously in this Appendix. The models considered for the dispersion relations of such kind of materials are presented next.

- Lorentz model

This model describes the dielectric function of a material in the presence of interband transitions and resonances by treating the electrons as harmonic oscillators that are driven by the electromagnetic field of the nuclei, such that[188–190]

$$\varepsilon_{\mathrm{i}}(E) = \sum_i \frac{A_i E_{0i} \gamma_i E}{\left(E_{0_i}^2 - E^2\right)^2 + E^2 \gamma_i^2}, \tag{A.3}$$

where E_{0_i} are the central energies, A_i the amplitudes and γ_i the damping factors of the i different harmonic oscillators.

The Lorentz model is widely used to determine the optical properties of dielectric materials such as glass, quartz, and crystals.[192–194] In many cases, however, it fails to describe accurately the optical response in the vicinity of the bandgap. To overcome such issues, more complete models combining the Lorentz oscillators with Tauc or Cody band edge functions are often considered.

- Tauc-Lorentz model

This model is very commonly used to determine the dielectric function of amorphous semiconductor materials. It assumes that the valence and conduction bands are parabolic and the momentum matrix element is constant, so[161–163,195–198]

$$\varepsilon_{\mathrm{i}}(E) = \begin{cases} \left(\displaystyle\sum_i \frac{A_i E_{0i} \gamma_i E}{\left(E_{0_i}^2 - E^2\right)^2 + E^2 \gamma_i^2} \right) \dfrac{(E - E_{\mathrm{g}})^2}{E^2} & \text{for } E > E_{\mathrm{g}} \\ 0 & \text{for } E \leq E_{\mathrm{g}} \end{cases}. \tag{A.4}$$

- Cody-Lorentz model

Similar to the Tauc-Lorentz model, the Cody-Lorentz model is also well suited to describe the optical response of amorphous semiconductor materials. Particular examples include amorphous hydrogenated silicon (a-Si:H)[199] and amorphous germanium (a-Ge).[200] The dielectric function in this case is obtained by assuming a constant dipole matrix element and is given by[162,163]

$$\varepsilon_{\mathrm{i}}(E) = \begin{cases} \left(\displaystyle\sum_i \frac{A_i E_{0i} \gamma_i E}{\left(E_{0_i}^2 - E^2\right)^2 + E^2 \gamma_i^2} \right) \dfrac{(E - E_{\mathrm{g}})^2}{(E - E_{\mathrm{g}})^2 + E_{\mathrm{p}}^2} & \text{for } E > E_{\mathrm{g}} \\ 0 & \text{for } E \le E_{\mathrm{g}} \end{cases} , \quad \text{(A.5)}$$

where E_{p} represents a transition energy that separates the absorption onset behavior from the Lorentz oscillator behavior.

- Urbach tail

Although the previous models work fairly well for a wide range of materials, they neglect any absorption below the bandgap and therefore they sometimes fail to describe the optical response in the region of the absorption edge. To account for such subgap absorption, an exponential Urbach tail is typically combined with any of the previous models.[161, 162, 164, 165] It is described as

$$\varepsilon_{\mathrm{i}}(E) = \frac{E_1}{E} \exp\left(\frac{E - E_{\mathrm{t}}}{E_{\mathrm{U}}} \right), \text{ for } 0 < E < E_{\mathrm{t}}, \quad \text{(A.6)}$$

where E_{U} is the Urbach energy, E_{t} is the demarcation energy between the Urbach tail and the band-to-band transitions, while E_1 is defined such that $\varepsilon_{\mathrm{i}}(E)$ is continuous at $E = E_{\mathrm{t}}$.

A.2 Refractive indexes used for the optical simulations

The refractive indexes of the FTO and BVO were determined as part of this thesis work. The optical constants of the BVO were calculated and shown in Chapter 3, while the derivation of the FTO refractive indexes from the dispersion relations of Section A.1 is presented next.

- FTO

The refractive indexes of the FTO were calculated by fitting the transmittance and reflectance spectra obtained for a glass/FTO substrate. This was done by combining the transfer matrix formalism with a least mean squares algorithm to minimize the differences between the experimental and the simulated values. The best fitting was obtained using a double Lorentz oscillator model, with oscillators centered at 267 nm and 1789 nm. The refractive indexes obtained are presented in Figure A.1.

For the remaining materials considered for the optical simulations carried out in this thesis, the refractive indexes used were obtained from previous works. Their real and imaginary parts are presented next in this section.
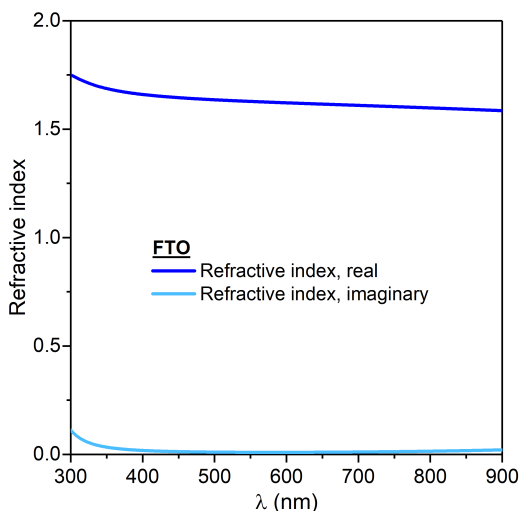
Figure A.1: Refractive indexes calculated for the FTO.

- Silver

Thick silver, deposited by thermal evaporation, was used in the fabrication of highly reflective mirrors and for the electric contacts of the OPV cells, while thin silver, deposited by magnetron sputtering, was considered for the semi-transparent electrodes of the solar cells employed in the BVO-OPV tandem.
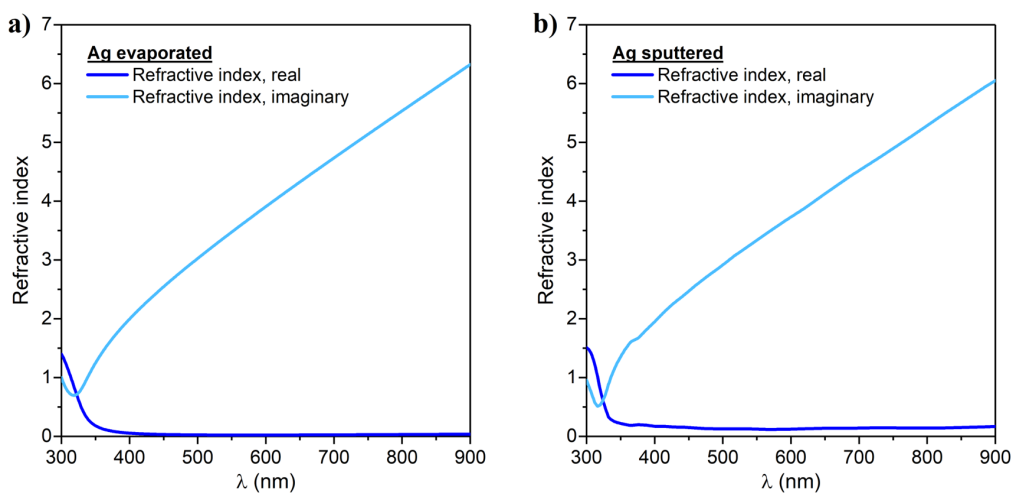

Figure A.2: Refractive indexes of the silver considered in this thesis: a) thick silver deposited by thermal evaporation and b) thin silver deposited by magnetron sputtering.

- Dielectric materials

Dielectric materials were used throughout this thesis to properly manage the light distribution for the different structures herein studied.
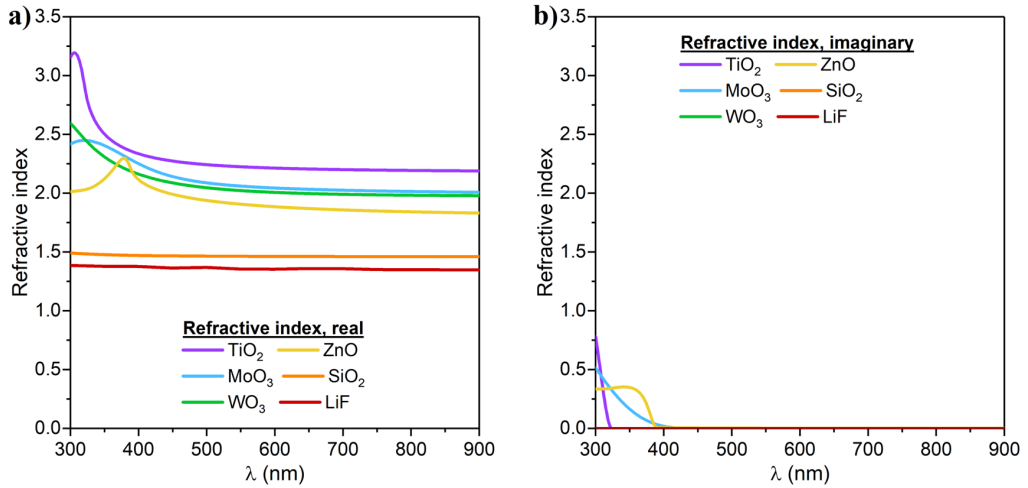
Figure A.3: Refractive indexes of all dielectric materials considered in this thesis: a) real and b) imaginary parts.

- Photovoltaic cells

OPV cells with PM6:Y6 active layer and structure: ITO/ZnO-SG/PM6:Y6/MoO$_3$/Ag were considered for the assembly of the tandem BVO-OPV devices.

High bandgap perovskite solar cells with a structure ITO/SnO$_2$/PVK/Spiro/Au, with an active layer composition of Cs$_y$FA$_{(1-y)}$Pb(I$_x$Cl$_{(1-x)}$)$_3$ and a CsCl to PbI$_2$ ratio of 0.17 were used to recycle the light with unwanted polarization trapped inside the guiding plate proposed in Chapter 2 of this thesis.
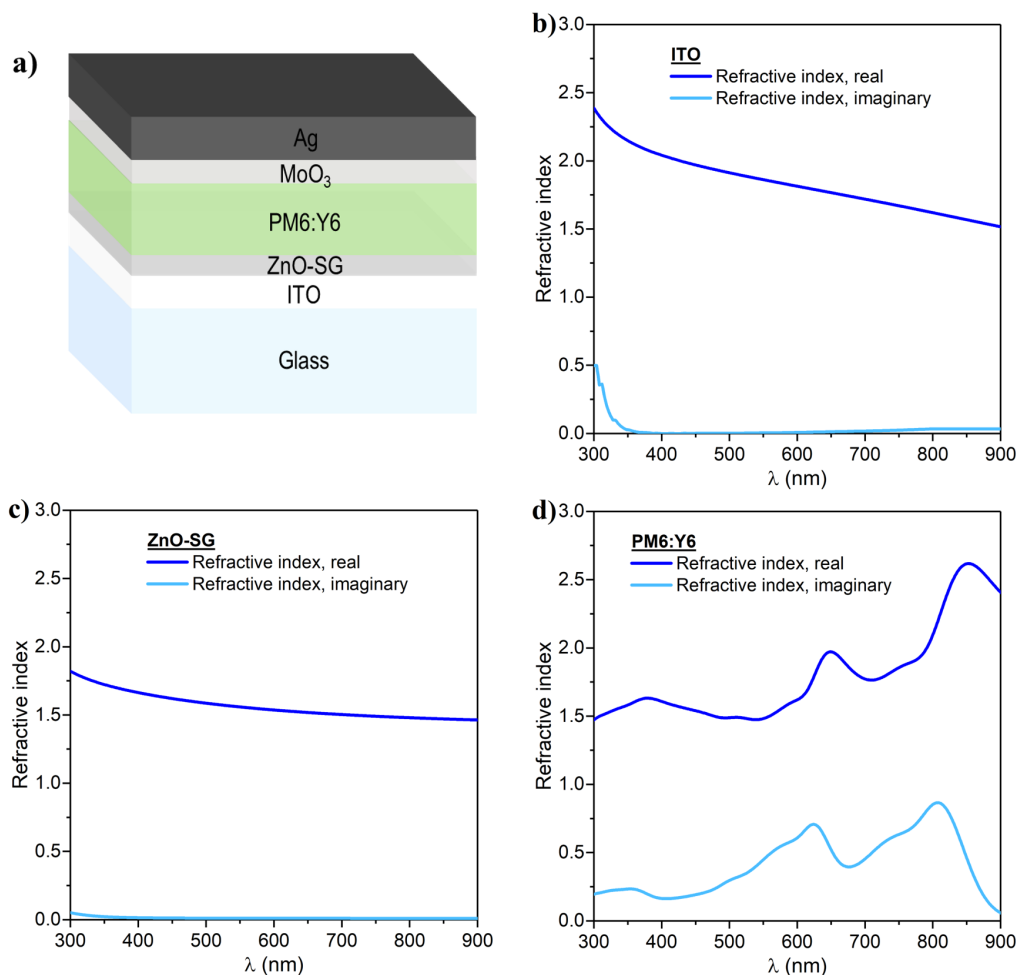
Figure A.4: Refractive indexes of the OPV cells. a) Structure of the OPV cell considered in this thesis. b) - d) Real and imaginary parts of the refractive indexes of the different layers: b) ITO, c) ZnO-SG, and d) PM6:Y6 organic blend. The refractive indexes of the MoO$_3$ and evaporated Ag contact are shown in the previous figures.
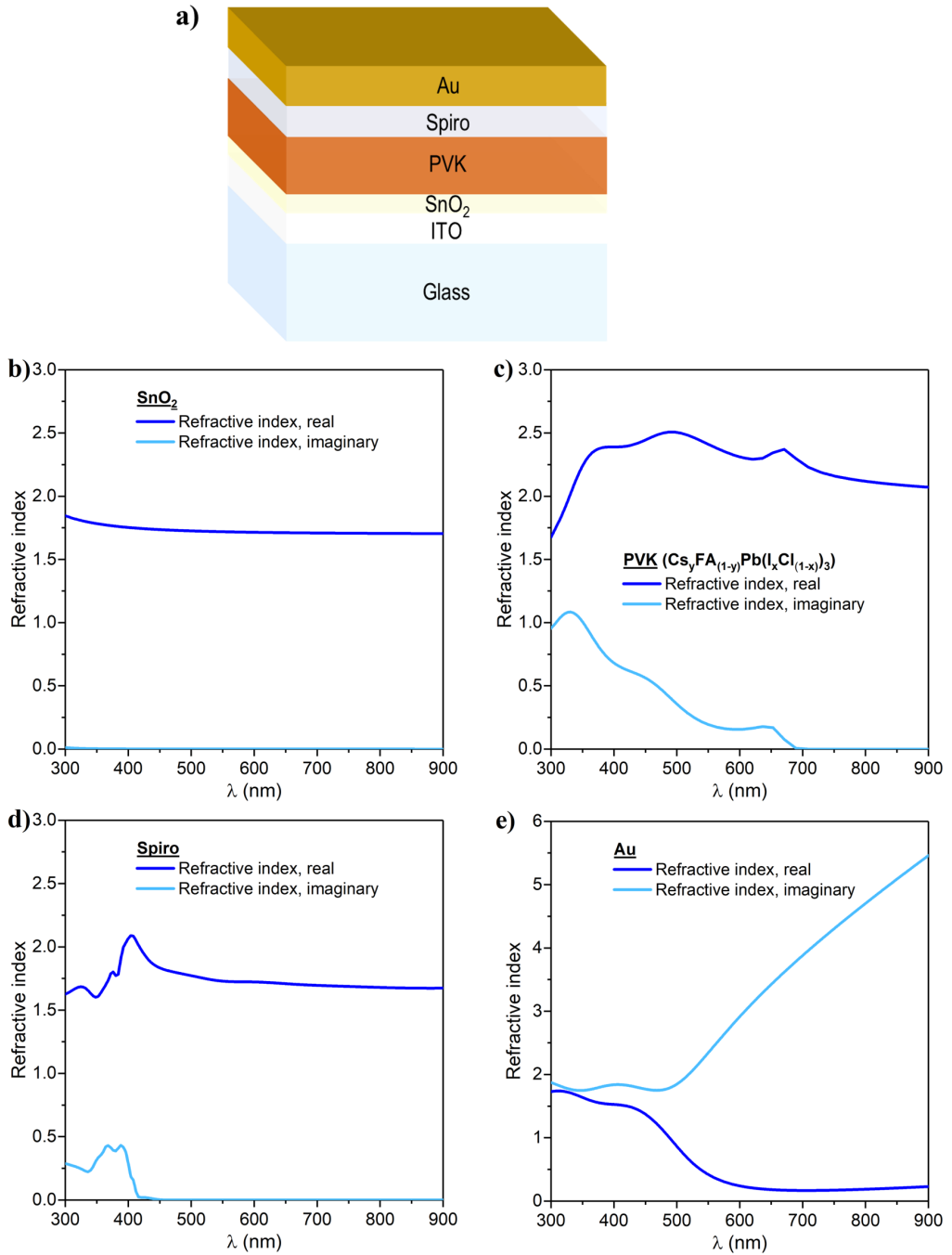
Figure A.5: Refractive indexes of the PVK cells. a) Structure of the perovskite PV cell considered in this thesis. b) - e) Real and imaginary parts of the refractive indexes of the different layers: b) SnO_2, c) PVK with a $Cs_yFA_{(1-y)}Pb(I_xCl_{(1-x)})_3$ composition, d) spiro, and e) gold..

Photoelectrochemical measurements

The present chapter intends to provide an insight on the photoelectrochemical measurements performed in this thesis to evaluate the water-splitting capability of the different BVO photoanodes. After a first introduction on the PEC cell configurations required for each kind of measurement, specific details on the experimental measurements will be given.

B.1 2- and 3-electrode configurations

Depending on the PEC device under study and on the type of measurement performed, different electrode configurations, illustrated in Figure B.1, must be chosen.
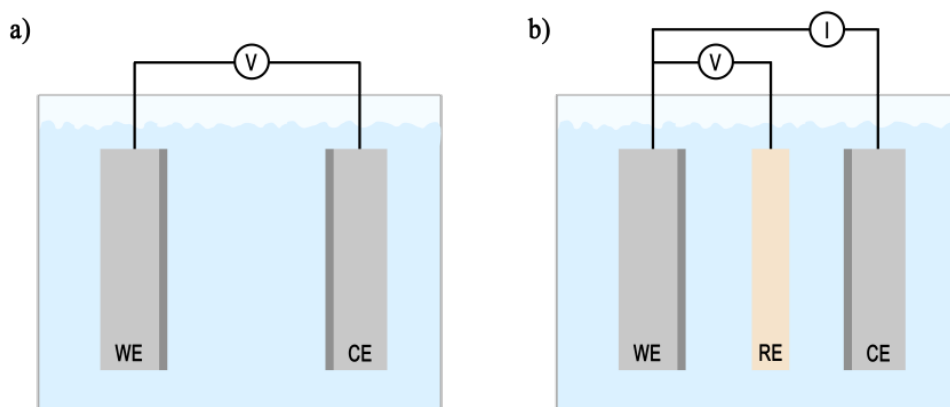
Figure B.1: Comparison between a) 2-electrode and b) 3-electrode configurations for PEC cells. In the images, WE stands for the working electrode, CE the counter electrode, and RE the reference electrode.

To appropriately calculate the STH conversion efficiency of a certain PEC system operating at bias-free conditions, as is the case of the BVO-OPV tandem devices explored in Chapter 4, the measurements must be performed in a 2-electrode configuration, schemat-

ically represented in Figure B.1 a), in which the photoelectrode (working electrode) is simply connected to a counter electrode and a bias source.[78, 185, 186] In this case, the full PEC system is considered and the *J-V* curve obtained is influenced not only by the response of the photoelectrode but also by the behavior of the counter electrode, which can suffer significant polarization losses when current passes. For this reason, a 3-electrode configuration, illustrated in Figure B.1 b), is typically considered in studies focusing on the capacity of an individual photoelectrode to perform the corresponding half-reaction, as in the case of the BVO photoanodes studied in Chapter 3. In this configuration, the contribution of the counter electrode is eliminated by adding to the PEC cell a reference electrode, which is at a fixed well-defined potential. A potentiostat is then used to supply to the counter electrode the current necessary to maintain the potential between the working electrode and the reference electrode at a desired value. In this case, there is no current flowing through the reference electrode, so the polarization losses are avoided and the response measured corresponds solely to the photoelectrode under study.[70, 71, 78, 186]

In order to compare the results experimentally obtained for half-cell measurements in a 3-electrode configuration with the ones reported by other authors, standard scales for the potential are typically used. In this thesis, results are reported in relation to the reversible hydrogen electrode (RHE) potential, which is independent of the pH. To convert the values measured in a 3-electrode configuration, V_{exp}, to the corresponding ones in the RHE scale, V_{RHE}, the Nernst equation should be applied as follows

$$V_{\mathrm{RHE}} = V_{\mathrm{exp}} + V_{\mathrm{RE}} \times 0.059 \times \mathrm{pH}, \tag{B.1}$$

where V_{RE} is a tabulated value, corresponding to the potential of the reference electrode used relative to the standard hydrogen potential.

B.2 Experimental details on PEC measurements

The water-splitting performance of both BVO photoanodes and tandem BVO-OPV devices was accessed in this thesis by means of *J-V*, EQE and hydrogen evolution measurements, made on a PEC cell filled with electrolyte solution and illuminated from a transparent quartz window placed on the cell side opposite to the BVO.

For the *J-V* measurements, an Abet Sun 2000 solar simulator, incorporating a 550 W xenon lamp from Ushio, was used to simulate 1-sun solar light AM1.5G illumination, and its intensity was calibrated with a silicon photodiode prior to each measurement. Bias voltages were applied by a Biologic SP-300 potentiostat, and scanned at a rate of 50 mV/s. For the single BVO photoanodes studied in Chapter 3, the measurements were performed in a 3-electrode configuration, with a platinum wire serving as the counter electrode and an Ag/AgCl electrode in 1.0 M KCl acting as reference electrode. For the BVO-OPV tandem devices studied in Chapter 4, 2-electrode measurements were per-

formed, using a platinum mesh that served as the counter electrode.

EQE measurements were carried out in a setup equipped with an Oriel 260 Cornerstone monochromator, from Newport Instruments, illuminated with a 300 W xenon lamp. The monochromatic power intensity was recorded with a calibrated S120VC silicon photodiode, from Thorlabs. A Biologic SP-300 potentiostat was used to apply a fixed voltage of 1.23 V_{RHE}, in a 3-electrode configuration, and to record the photocurrent density for each individual wavelength. To improve the sensitivity of the measurements, the aperture of the monochromator slits was adjusted such that the irradiance of the light on the BVO surface was maximized, and the acquisition times were increased to 5 seconds per wavelength point. In addition, these measurements were performed inside a black box to avoid possible side effects caused by the presence of ambient light.

Hydrogen evolution measurements were performed for the tandem BVO-OPV devices in a completely sealed PEC cell with double compartment, separated by a transparent Nafion 117 ion-exchange membrane to ensure that all the H_2 produced would remain in the corresponding compartment. A hydrogen microsensor from Unisense was used to constantly monitor the concentration of H_2 over time, generated by the tandem devices at bias-free conditions inside a burette which was inserted into one of the PEC cell apertures. Prior to each measurement, the microsensor was calibrated using known concentrations of hydrogen in air. Volume readings were taken every 30 minutes, from which the amount of H_2 and faradaic efficiency were determined.

B.3 PEC cell used

In this thesis, we used custom-made photoelectrochemical cells, designed at ICFO, that could have either one or two separate 7 mL volume cylindrical compartments, with several inlets that allow the introduction of a counter electrode, reference electrode, and hydrogen sensor, as illustrated in Figure B.2 a).

For the *J-V* and EQE measurements, a single-compartment configuration, shown in Figure B.2 b), was used. On the other hand, a double-compartment PEC cell as the one in Figure B.2 c) was considered for the hydrogen evolution measurements and consequently for the calculation of the STH conversion efficiency.
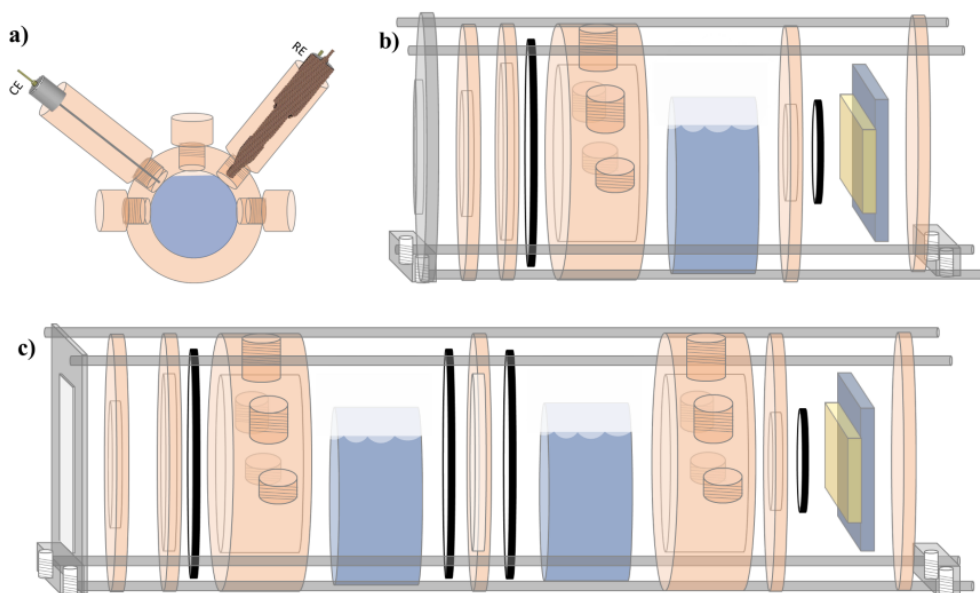
Figure B.2: a) Front view of one of the electrolyte compartments, showing the available inlets and the introduction of the counter electrode, CE, and reference electrode, RE. Side view of the b) single compartment PEC used for the J-V and EQE measurements and of the c) double compartment PEC (separated by a Nafion membrane) considered to study the H_2 gas evolution.

B.4   Assembly of the BVO-OPV tandem devices

The tandem devices were assembled as shown in Figure B.3, by placing the OPV cells on the back side of the BVO photoanodes, using a UV curable index-matching resin to fix the two glasses together. The active area of the devices was limited by the photovoltaic cell to 0.06 cm^2, which was obtained by the use of a black vinyl sticker to partially cover the surface of the BVO. Electric connections were created using Ag conductive tape connected with silver paste to the evaporated Ag contacts of the OPV cell and the FTO layer of the BVO photoanode. An external wire was used to electrically connect the BVO photoanode to the cathode of the OPV cell, while the anode of the photovoltaic cell was used as the working electrode for the tandem configuration. The installation of a tandem device into the custom-made PEC cell is illustrated in Figure B.4.
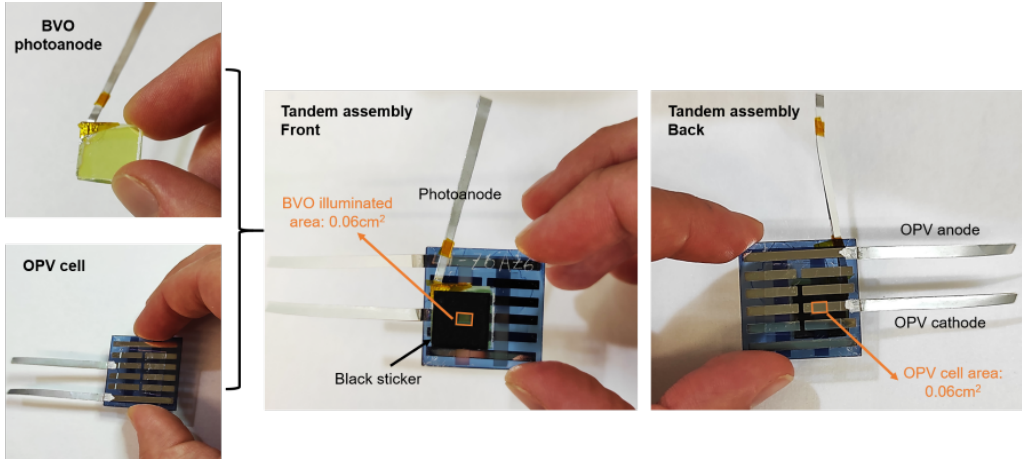
Figure B.3: Assembly of the BVO-OPV tandem devices.
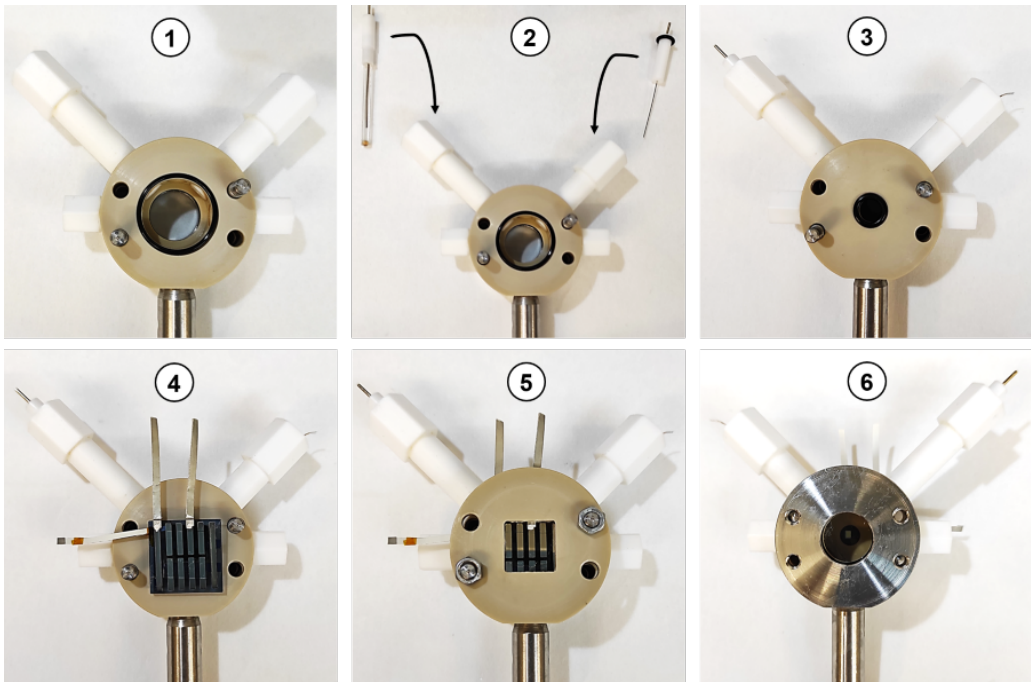
Figure B.4: Steps performed to install the tandem devices in the single-compartment custom-made PEC cell used for J-V and EQE measurements. In the 2-electrode measurements of BVO-OPV tandem devices, the Pt wire counter electrode (top right side in step 2) was replaced by a Pt mesh, and the Ag/AgCl reference electrode (top left side in step 2) was not introduced.

Diode model to describe *J-V* curves of the OPV and BVO

Typically, the current-voltage characteristics of PV[3,67,181] and PEC[54,75,77,180,201,202] cells can be described using an equivalent circuit like the one depicted in Figure C.1, which integrates a photocurrent source, a diode, and two parasitic resistances. While the photocurrent source represents the free charges generated after the light absorption, the diode accounts for the electron-hole recombination happening at the semiconductor material. A series resistance R_s describes the internal resistance across the cell, including the contacts, and a shunt resistance R_sh models the power losses due to the presence of defects in the materials. The current flowing through a PV or PEC cell upon illumination, based on such an equivalent circuit, can be described as

$$I = I_L - I_0 \exp\left[\frac{q\left(V + IR_\mathrm{s}\right)}{n_\mathrm{id}k_\mathrm{B}T}\right] - \frac{V + IR_\mathrm{s}}{R_\mathrm{sh}}, \tag{C.1}$$

where the first term on the right-hand side represents the light-generated current, the second corresponds to the current lost by recombination and the last term describes the current losses due to the shunt resistance. In this expression, I_0 is the dark saturation current, q the electron charge, k_B is the Boltzmann constant, T the temperature in Kelvin, and n_id is the ideality factor of the diode.

The *J-V* behavior of the BVO photoanodes and OPV cells considered in this thesis can therefore be simulated by the single-diode model described by equation (C.1), where the light-generated current I_L was obtained at open circuit condition as

$$I_L = I_0 \exp\left[\frac{qV_\mathrm{oc}}{n_\mathrm{id}k_\mathrm{B}T}\right] + \frac{V_\mathrm{oc}}{R_\mathrm{sh}}, \tag{C.2}$$
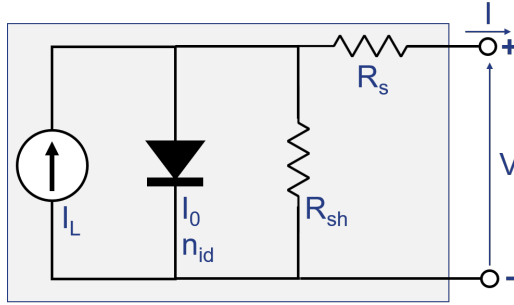
Figure C.1: Equivalent circuit typically used to model the *J-V* response of a PV or PEC cell.

while the dark saturation current I_0 was determined at short circuit condition, such that

$$I_0 = \frac{-\dfrac{V_{oc}}{R_{sh}} + I_{sc}\left(1 + \dfrac{R_s}{R_{sh}}\right)}{\exp\left[\dfrac{qV_{oc}}{n_{id}k_BT}\right] - \exp\left[\dfrac{qI_{sc}R_s}{n_{id}k_BT}\right]} \, . \tag{C.3}$$

As can be easily seen, after performing these substitutions, the *J-V* relations of equation (C.1) will only depend on the ideality factor n_{id} and on the electrical parameters of the photoanode and photovoltaic cell, such as short circuit current, open circuit voltage, and series and shunt resistances.

The short circuit current for the OPV cell (or the current at 1.23 V$_{RHE}$ for the case of the BVO photoanode) can be determined using the general transfer matrix method described in Section 1.5.1 of this thesis, which considers coherent light propagation in the multilayer thin film stacks (photoanode and OPV cell), as well as the incoherency introduced by the millimeter-thick glasses. On the other hand, the V_{oc}, R_s and R_s can be related to the I_{sc} (or J_{sc}) with fairly good accuracy by experimentally measuring the *J-V* curves obtained under different illumination intensities and by analyzing the relationships observed between the electrical parameters.

For the case of the PM6:Y6 photovoltaic cell, presented in Figure C.2, the V_{oc} increased logarithmically with the J_{sc}, while R_s and R_{sh} decreased exponentially. As for the BVO photoanode, illustrated in Figure C.3, the V_{oc} remained practically constant for the reaction in 1.0 M KBi at pH 9, with R_s and R_{sh} decreasing exponentially with the short circuit current density. The specific relationships found between all the parameters are written inside the different plots.
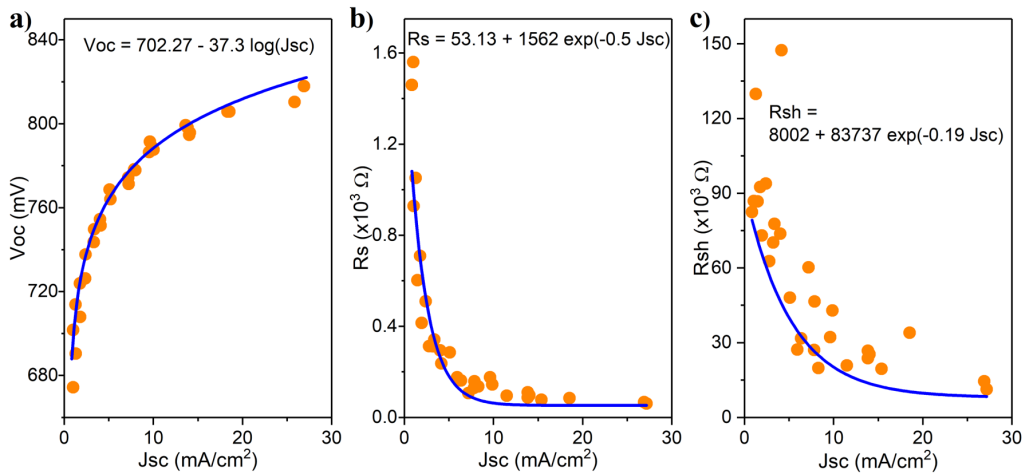
Figure C.2: Relationship between the electrical parameters of the PM6:Y6 photovoltaic cells experimentally measured under different illumination intensities: a) V_{oc} vs J_{sc}, b) R_s vs J_{sc} and c) R_{sh} vs J_{sc}.
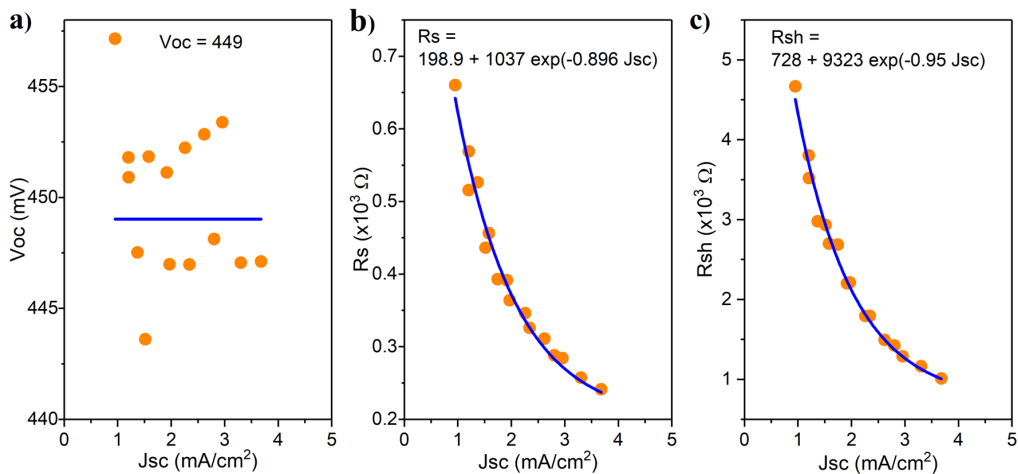

Figure C.3: Relationship between the electrical parameters of the BVO photoanode experimentally measured under different illumination intensities: a) V_{oc} vs J_{sc}, b) R_s vs J_{sc} and c) R_{sh} vs J_{sc}. In this case, a 2-electrode configuration was considered for the water-splitting reaction in 1.0 M KBi at pH 9. A FeOOH/NiOOH catalyst was electrodeposited on the surface of the BVO to facilitate the oxygen evolution reaction.

To get the most suitable ideality factors, the *J-V* curves of each element were fitted to the experimental results obtained under different illumination intensities, considering the relationships between the electrical parameters shown in Figure C.2 and Figure C.3. The best-fitting ideality factors were 2.0 for the photoanode and 1.75 for the photovoltaic cell, and the comparison between the different simulated and experimental curves is illustrated in Figure C.4, where a very good agreement can be seen for the whole range of values considered, which proves the viability of this method to describe with accuracy the behavior of both elements of the tandem.
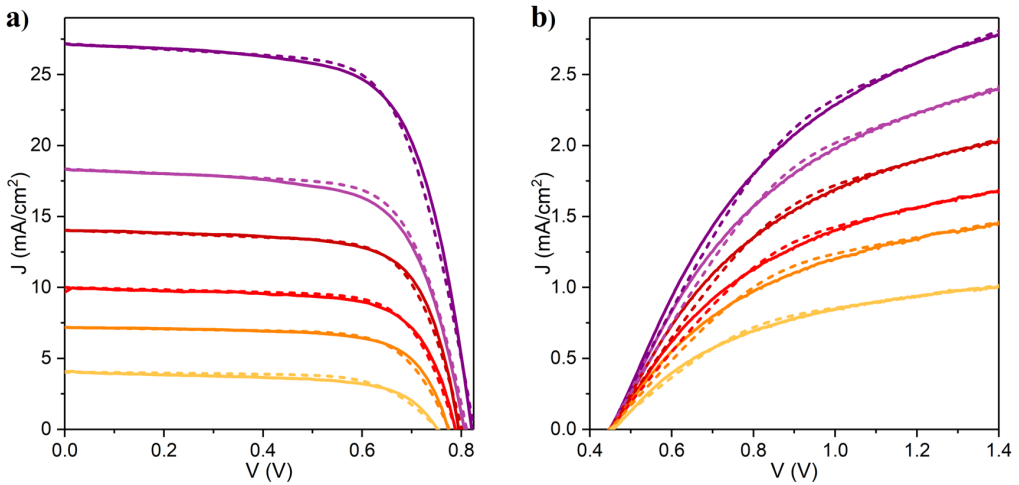
Figure C.4: Comparison between the simulated (dashed lines) and experimental (solid lines) *J-V* curves of the a) OPV cell and b) BVO photoanode, for different values of short circuit current density (obtained by measuring under different illumination intensities), illustrating the good agreement between the single-diode model used to simulate the curves and the experimental *J-V* response obtained. For all experimental curves, the average between the forward and the reverse scans was considered.

From these fittings, it is possible to estimate the bias-free current density of a tandem device incorporating a BVO photoanode and an OPV cell, by calculating the *J-V* coordinates of the intersection point between the two curves.

Bibliography

[1] *BP statistical review of world energy 71st edition*. Technical report, British Petroleum (2022). (cited on pp. 1 and 2)

[2] *Renewables 2022: Global status report*. Technical report, REN21 (2022). (cited on p. 1)

[3] J. Klaus-Dieter, I. Olindo, A. H. M. Smets, R. A. C. M. M. V. Swaaij, and M. Zeman. *Solar energy: Fundamentals, technology and systems*. Cambridge. (2016). (cited on pp. 1 and 93)

[4] R. B. Jackson, P. Friedlingstein, C. L. Quéré, S. Abernethy, R. M. Andrew, J. G. Canadell, P. Ciais, S. J. Davis, Z. Deng, Z. Liu, J. I. Korsbakken, and G. P. Peters. *Global fossil carbon emissions rebound near pre-COVID-19 levels*. Environmental Research Letters **17** (2022), 031001. doi:10.1088/1748-9326/ac55b6. (cited on pp. 1 and 2)

[5] J. Hansen, M. Sato, and R. Ruedy. *Global temperature in 2022*. Technical report (2023). (cited on pp. 1 and 2)

[6] *Inventory of U.S. greenhouse gas emissions and sinks - 1990 to 2020*. Technical report, United States Environmental Protection Agency (2020). (cited on p. 1)

[7] *Climate science: A summary for actuaries*. Technical report, International Actuarial Association (2022). (cited on p. 1)

[8] J. Kimmel. *Diffractive backlight technologies for mobile applications*. Journal of the Society for Information Display **20** (2012), 245. doi:10.1889/JSID20.5.245. (cited on pp. 1 and 2)

[9] G.-W. Yoon, S.-W. Bae, Y.-B. Lee, and J.-B. Yoon. *Edge-lit LCD backlight unit for 2D local dimming*. Optics Express **26** (2018), 20802. doi:10.1364/OE.26.020802. (cited on p. 1)

[10] C. G. Ferreira, G. Martínez-Denegri, M. Kramarenko, J. Toudert, and J. Martorell. *Light recycling using perovskite solar cells in a half-cylinder photonic plate for an energy efficient broadband polarized light emission*. Advanced Photonics Research **2** (2021), 2100077. doi:10.1002/adpr.202100077. (cited on p. 2)

[11] J.-W. Pan and C.-W. Fan. *High luminance hybrid light guide plate for backlight module application*. Optics Express **19** (2011), 20079. doi:10.1364/OE.19.020079. (cited on p. 2)

[12] T. C. Teng and C. H. Sun. *Integrating backlight with color-filter-free panel for enhancing performance of LCD*. IEEE Photonics Journal **12** (2020), 1. doi:10.1109/JPHOT.2019.2957385. (cited on p. 2)

[13] Y. Li, S. T. Wu, and T. X. Wu. *Design optimization of reflective polarizers for LCD backlight recycling*. IEEE/OSA Journal of Display Technology **5** (2009), 335. doi:10.1109/JDT.2009.2027033. (cited on pp. 2 and 3)

[14] G. Martínez-Denegri, C. G. Ferreira, M. A. Ruiz-Preciado, P. Fassl, M. Kramarenko, U. W. Paetzold, and J. Martorell. *Wide bandgap perovskite photovoltaic cells for stray light recycling in a system emitting broadband polarized light*. Advanced Energy Materials **12** (2022), 2201473. doi:10.1002/aenm.202201473. (cited on pp. 2, 43, and 46)

[15] T. Okumura, A. Tagaya, Y. Koike, M. Horiguchi, and H. Suzuki. *Highly-efficient backlight for liquid crystal display having no optical films*. Applied Physics Letters **83** (2003), 2515. doi:10.1063/1.1613051. (cited on p. 2)

[16] M. F. Weber, C. A. Stover, L. R. Gilbert, T. J. Nevitt, and A. J. Ouderkirk. *Giant birefringent optics in multilayer polymer mirrors*. Science **287** (2000), 2451. doi:10.1126/science.287.5462.245. (cited on p. 3)

[17] M. Y. Yu, B. W. Lee, J. H. Lee, and J. H. Ko. *Correlation between the optical performance of the reflective polarizer and the structure of LCD backligeht*. Journal of the Optical Society of Korea **13** (2009), 256. doi:10.3807/JOSK.2009.13.2.256. (cited on p. 3)

[18] K. W. Chien and H. P. D. Shieh. *Design and fabrication of an integrated polarized light guide for liquid-crystal-display illumination*. Applied Optics **43** (2004), 1830. doi:10.1364/ao.43.001830. (cited on p. 3)

[19] M. Suzuki. *Two approaches to the luminance enhancement of backlighting units for LCDs*. Journal of the Society for Information Display **7** (1999), 157. doi:10.1889/1.1984469. (cited on p. 3)

[20] S. Castelletto and A. Boretti. *Luminescence solar concentrators: A technology update*. Nano Energy **109** (2023), 108269. doi:10.1016/j.nanoen.2023.108269. (cited on p. 3)

[21] M. G. Debije and P. P. Verbunt. *Thirty years of luminescent solar concentrator research: Solar energy for the built environment*. Advanced Energy Materials **2** (2012), 12. doi:10.1002/aenm.201100554. (cited on p. 3)

[22] C. L. Mulder, P. D. Reusswig, A. M. Velázquez, H. Kim, C. Rotschild, and M. A. Baldo. *Dye alignment in luminescent solar concentrators: I vertical*

alignment for improved waveguide coupling. Optics Express **18** (2010), A79. doi:10.1364/OE.18.000A79. (cited on p. 3)

[23] C. L. Mulder, P. D. Reusswig, A. P. Beyler, H. Kim, C. Rotschild, and M. A. Baldo. *Dye alignment in luminescent solar concentrators: II horizontal alignment for energy harvesting in linear polarizers*. Optics Express **18** (2010), A91. doi:10.1364/oe.18.000a91. (cited on p. 3)

[24] M. Rafiee, S. Chandra, H. Ahmed, and S. J. McCormack. *An overview of various configurations of luminescent solar concentrators for photovoltaic applications*. Optical Materials **91** (2019), 212. doi:10.1016/j.optmat.2019.01.007. (cited on p. 3)

[25] C. L. Mulder, L. Theogarajan, M. Currie, J. K. Mapel, M. A. Baldo, M. Vaughn, P. Willard, B. D. Bruce, M. W. Moss, C. E. McLain, and J. P. Morseman. *Luminescent solar concentrators employing phycobilisomes*. Advanced Materials **21** (2009), 3181. doi:10.1002/adma.200900148. (cited on p. 3)

[26] P. P. Verbunt, A. Kaiser, K. Hermans, C. W. Bastiaansen, D. J. Broer, and M. G. Debije. *Controlling light emission in luminescent solar concentrators through use of dye molecules aligned in a planar manner by liquid crystals*. Advanced Functional Materials **19** (2009), 2714. doi:10.1002/adfm.200900542. (cited on p. 3)

[27] Y. Zhao, G. A. Meek, B. G. Levine, and R. R. Lunt. *Near-infrared harvesting transparent luminescent solar concentrators*. Advanced Optical Materials **2** (2014), 606. doi:10.1002/adom.201400103. (cited on p. 3)

[28] J. Bomm, A. Büchtemann, A. J. Chatten, R. Bose, D. J. Farrell, N. L. Chan, Y. Xiao, L. H. Slooff, T. Meyer, A. Meyer, W. G. Van Sark, and R. Koole. *Fabrication and full characterization of state-of-the-art quantum dot luminescent solar concentrators*. Solar Energy Materials and Solar Cells **95** (2011), 2087. doi:10.1016/j.solmat.2011.02.027. (cited on p. 3)

[29] N. D. Bronstein, Y. Yao, L. Xu, E. O'Brien, A. S. Powers, V. E. Ferry, A. P. Alivisatos, and R. G. Nuzzo. *Quantum dot luminescent concentrator cavity exhibiting 30-fold concentration*. ACS Photonics **2** (2015), 1576. doi:10.1021/acsphotonics.5b00334. (cited on p. 3)

[30] A. Menéndez-Velázquez, C. L. Mulder, N. J. Thompson, T. L. Andrew, P. D. Reusswig, C. Rotschild, and M. A. Baldo. *Light-recycling within electronic displays using deep red and near infrared photoluminescent polarizers*. Energy and Environmental Science **6** (2013), 72. doi:10.1039/C2EE23265K. (cited on p. 3)

[31] B. Park, Y. H. Huh, and J. C. Shin. *In-plane anisotropy of photovoltaic effects in aligned polymer solar cells*. Solar Energy Materials and Solar Cells **95** (2011), 3543. doi:10.1016/j.solmat.2011.08.023. (cited on p. 3)

[32] R. Zhu, A. Kumar, and Y. Yang. *Polarizing organic photovoltaics*. Advanced Materials **23** (2011), 4193. doi:10.1002/adma.201101514. (cited on p. 3)

[33] S. Gharibzadeh, I. M. Hossain, P. Fassl, B. A. Nejand, T. Abzieher, M. Schultes, E. Ahlswede, P. Jackson, M. Powalla, S. Schäfer, M. Rienäcker, T. Wietler, R. Peibst, U. Lemmer, B. S. Richards, and U. W. Paetzold. *2D/3D heterostructure for semitransparent perovskite solar cells with engineered bandgap enables efficiencies exceeding 25% in four-terminal tandems with silicon and CIGS*. Advanced Functional Materials **30** (2020). doi:10.1002/adfm.201909919. (cited on p. 3)

[34] N. J. Jeon, J. H. Noh, W. S. Yang, Y. C. Kim, S. Ryu, J. Seo, and S. I. Seok. *Compositional engineering of perovskite materials for high-performance solar cells*. Nature **517** (2015), 476. doi:10.1038/nature14133. (cited on p. 3)

[35] T. J. Jacobsson, J. P. Correa-Baena, M. Pazoki, M. Saliba, K. Schenk, M. Grätzel, and A. Hagfeldt. *Exploration of the compositional space for mixed lead halogen perovskites for high efficiency solar cells*. Energy and Environmental Science **9** (2016), 1706. doi:10.1039/C6EE00030D. (cited on p. 3)

[36] F. Meier, S. N. Schumann, M. Streiter, and C. Deibel. *Charge carrier dynamics of multiple-cation mixed-halide perovskite thin films*. Journal of Physical Chemistry C **125** (2021), 17411. doi:10.1021/acs.jpcc.1c04302. (cited on p. 3)

[37] C. M. Sutter-Fella, Y. Li, M. Amani, J. W. Ager, F. M. Toma, E. Yablonovitch, I. D. Sharp, and A. Javey. *High photoluminescence quantum yield in band gap tunable bromide containing mixed halide perovskites*. Nano Letters **16** (2016), 800. doi:10.1021/acs.nanolett.5b04884. (cited on p. 3)

[38] H. Zhang, M. Kramarenko, G. Martínez-Denegri, J. Osmond, J. Toudert, and J. Martorell. *Formamidinium incorporation into compact lead iodide for low band gap perovskite solar cells with open-circuit voltage approaching the radiative limit*. ACS Applied Materials and Interfaces **11** (2019), 9083. doi:10.1021/acsami.8b20899. (cited on p. 3)

[39] M. Kramarenko, C. G. Ferreira, G. Martínez-Denegri, C. Sansierra, J. Toudert, and J. Martorell. *Relation between fluorescence quantum yield and open-circuit voltage in complete perovskite solar cells*. Solar RRL **4** (2020), 1. doi:10.1002/solr.201900554. (cited on pp. 3 and 6)

[40] Z. Liu, L. Krückemeier, B. Krogmeier, B. Klingebiel, J. A. Márquez, S. Levcenko, S. Öz, S. Mathur, U. Rau, T. Unold, and T. Kirchartz. *Open-circuit voltages exceeding* 1.26 *V in planar methylammonium lead iodide perovskite solar cells*. ACS Energy Letters **4** (2019), 110. doi:10.1021/acsenergylett.8b01906. (cited on p. 3)

[41] W. Tress. *Perovskite solar cells on the way to their radiative efficiency limit – insights into a success story of high open-circuit voltage and low recombination*. Advanced Energy Materials **7** (2017). doi:10.1002/aenm.201602358. (cited on p. 3)

[42] A. Riquelme, F. E. Gálvez, L. Contreras-Bernal, H. Míguez, and J. A. Anta. *Internal quantum efficiency and time signals from intensity-modulated photocurrent spectra of perovskite solar cells*. Journal of Applied Physics **128** (2020). doi:10.1063/5.0013317. (cited on p. 3)

[43] A. P. Amalathas and M. M. Alkaisi. *Nanostructures for light trapping in thin film solar cells*. Micromachines **10** (2019), 1. doi:10.3390/mi10090619. (cited on p. 4)

[44] C. Chen, S. Zheng, and H. Song. *Photon management to reduce energy loss in perovskite solar cells*. Chemical Society Reviews **50** (2021), 7250. doi:10.1039/d0cs01488e. (cited on p. 4)

[45] S. Haque, M. J. Mendes, O. Sanchez-Sobrado, H. Águas, E. Fortunato, and R. Martins. *Photonic-structured TiO$_2$ for high-efficiency, flexible and stable perovskite solar cells*. Nano Energy **59** (2019), 91. doi:10.1016/j.nanoen.2019.02.023. (cited on p. 4)

[46] R. Lampande, G. W. Kim, M. J. Park, B. Y. Kang, and J. H. Kwon. *Efficient light harvesting in inverted polymer solar cells using polymeric 2D-microstructures*. Solar Energy Materials and Solar Cells **151** (2016), 162. doi:10.1016/j.solmat.2016.03.005. (cited on pp. 4 and 12)

[47] Q. Liu, P. Romero-gomez, P. Mantilla-perez, S. Colodrero, J. Toudert, and J. Martorell. *A two-resonance tapping cavity for an optimal light trapping in thin-film solar cells*. Advanced Energy Materials **7** (2017), 1700356. doi:10.1002/aenm.201700356. (cited on pp. 4, 63, and 64)

[48] Q. Liu, J. Toudert, T. Li, M. Kramarenko, G. Martínez-Denegri, L. Ciammaruchi, X. Zhan, and J. Martorell. *Inverse optical cavity design for ultrabroadband light absorption beyond the conventional limit in low-bandgap non-fullerene acceptor–based solar cells*. Advanced Energy Materials **9** (2019), 1. doi:10.1002/aenm.201900463. (cited on pp. 4, 63, and 64)

[49] Z. Tang, W. Tress, and O. Inganäs. *Light trapping in thin film organic solar cells*. Materials Today **17** (2014), 389. doi:10.1016/j.mattod.2014.05.008. (cited on p. 4)

[50] Y. Wang, P. Wang, X. Zhou, C. Li, H. Li, X. Hu, F. Li, X. Liu, M. Li, and Y. Song. *Diffraction-grated perovskite induced highly efficient solar cells through nanophotonic light trapping*. Advanced Energy Materials **8** (2018), 1702960. doi:10.1002/aenm.201702960. (cited on p. 4)

[51] H. Zhang, M. Kramarenko, J. Osmond, J. Toudert, and J. Martorell. *Natural random nanotexturing of the Au interface for light backscattering enhanced performance in perovskite solar cells*. ACS Photonics **5** (2018), 2243. doi:10.1021/acsphotonics.8b00099. (cited on p. 4)

[52] A. R. Bielinski, A. J. Gayle, S. Lee, and N. P. Dasgupta. *Geometric optimization of bismuth vanadate core-shell nanowire photoanodes using atomic layer deposition*. ACS Applied Materials and Interfaces **13** (2021), 52063. doi:10.1021/acsami.1c09236. (cited on p. 4)

[53] Y. Chen, W. Zheng, S. Murcia-López, F. Lv, J. R. Morante, L. Vayssieres, and C. Burda. *Light management in photoelectrochemical water splitting - from materials to device engineering*. Journal of Materials Chemistry C **9** (2021), 3726. doi:10.1039/d0tc06071b. (cited on p. 4)

[54] D. V. Esposito, Y. Lee, H. Yoon, P. M. Haney, N. Y. Labrador, T. P. Moffat, A. A. Talin, and V. A. Szalai. *Deconvoluting the influences of 3D structure on the performance of photoelectrodes for solar-driven water splitting*. Sustainable Energy and Fuels **1** (2017), 154. doi:10.1039/c6se00073h. (cited on pp. 4 and 93)

[55] I. Khan, A. Jalilov, K. Fujii, and A. Qurashi. *Quasi-1D aligned nanostructures for solar-driven water splitting applications: Challenges, promises, and perspectives*. Solar RRL **5** (2021), 2000741. doi:10.1002/solr.202000741. (cited on p. 4)

[56] J. Liu, J. Li, M. Shao, and M. Wei. *Directed synthesis of SnO₂@BiVO₄/Co-Pi photoanode for highly efficient photoelectrochemical water splitting and urea oxidation*. Journal of Materials Chemistry A **7** (2019), 6327. doi:10.1039/c8ta11573g. (cited on p. 4)

[57] Y. Pihosh, I. Turkevych, K. Mawatari, J. Uemura, Y. Kazoe, S. Kosar, K. Makita, T. Sugaya, T. Matsui, D. Fujita, M. Tosa, M. Kondo, and T. Kitamori. *Photocatalytic generation of hydrogen by core-shell WO₃/BiVO₄ nanorods with ultimate water splitting efficiency*. Scientific Reports **5** (2015), 1. doi:10.1038/srep11141. (cited on p. 4)

[58] Y. Qiu, W. Liu, W. Chen, G. Zhou, P. C. Hsu, R. Zhang, Z. Liang, S. Fan, Y. Zhang, and Y. Cui. *Efficient solar-driven water splitting by nanocone BiVO₄-perovskite tandem cells*. Science Advances **2** (2016). doi:10.1126/sciadv.1501764. (cited on p. 4)

[59] T. G. Vo, J. M. Chiu, Y. Tai, and C. Y. Chiang. *Turnip-inspired BiVO₄/CuSCN nanostructure with close to 100% suppression of surface recombination for solar water splitting*. Solar Energy Materials and Solar Cells **185** (2018), 415. doi:10.1016/j.solmat.2018.05.054. (cited on p. 4)

[60] S. Xiao, C. Hu, H. Lin, X. Meng, Y. Bai, T. Zhang, Y. Yang, Y. Qu, K. Yan, J. Xu, Y. Qiu, and S. Yang. *Integration of inverse nanocone array based bismuth vanadate photoanodes and bandgap-tunable perovskite solar cells for efficient self-powered solar water splitting*. Journal of Materials Chemistry A **5** (2017), 19091. doi:10.1039/c7ta06309a. (cited on p. 4)

[61] L. Han, F. F. Abdi, R. V. D. Krol, R. Liu, Z. Huang, H. J. Lewerenz, B. Dam, M. Zeman, and A. H. Smets. *Efficient water-splitting device based on a bismuth vanadate photoanode and thin-film silicon solar cells*. ChemSusChem **7** (2014), 2832. doi:10.1002/cssc.201402456. (cited on p. 4)

[62] X. Li, M. Jia, Y. Lu, N. Li, Y. Z. Zheng, X. Tao, and M. Huang. *Co(OH)₂/BiVO₄ photoanode in tandem with a carbon-based perovskite solar cell for solar-driven overall water splitting*. Electrochimica Acta **330** (2020). doi:10.1016/j.electacta.2019.135183. (cited on p. 4)

[63] D. Xue, M. Kan, X. Qian, and Y. Zhao. *A tandem water splitting cell based on nanoporous BiVO₄ photoanode cocatalyzed by ultrasmall cobalt borate sandwiched with conformal TiO₂ layers*. ACS Sustainable Chemistry and Engineering **6** (2018), 16228. doi:10.1021/acssuschemeng.8b03078. (cited on p. 4)

[64] Y. Peng, G. V. Govindaraju, D. K. Lee, K. S. Choi, and T. L. Andrew. *Integrating a semitransparent, fullerene-free organic solar cell in tandem with a BiVO₄ photoanode for unassisted solar water splitting*. ACS Applied Materials and Interfaces **9** (2017), 22449. doi:10.1021/acsami.7b04486. (cited on p. 4)

[65] S. Zhang, L. Shen, T. Ye, K. Kong, H. Ye, H. Ding, Y. Hu, and J. Hua. *Noble-metal-free perovskite-BiVO₄ tandem device with simple preparation method for unassisted solar water splitting*. Energy and Fuels **34** (2020), 5016. doi:10.1021/acs.energyfuels.0c00432. (cited on p. 4)

[66] C. Hu and R. M. White. *Solar cells: From basic to advanced systems*. McGraw-Hill. (1983). (cited on p. 5)

[67] A. Luque and S. Hegedus. *Handbook of photovoltaic science and engineering*. John Wiley & Sons. (2011). doi:10.1002/9780470974704. (cited on pp. 5 and 93)

[68] U. Rau, U. W. Paetzold, and T. Kirchartz. *Thermodynamics of light management in photovoltaic devices*. Physical Review B - Condensed Matter and Materials Physics **90** (2014), 1. doi:10.1103/PhysRevB.90.035211. (cited on p. 6)

[69] W. Shockley and H. J. Queisser. *Detailed balance limit of efficiency of p-n junction solar cells*. Journal of Applied Physics **32** (1961), 510. doi:10.1063/1.1736034. (cited on pp. 6, 10, and 36)

[70] R. V. D. Krol and M. Grätzel. *Photoelectrochemical hydrogen production*. Springer. (2012). doi:10.1007/978-1-4614-1380-6. (cited on pp. 8 and 88)

[71] C. Ros, T. Andreu, and J. R. Morante. *Photoelectrochemical water splitting: A road from stable metal oxides to protected thin film solar cells*. Journal of Materials Chemistry A **8** (2020), 10625. doi:10.1039/d0ta02755c. (cited on pp. 8, 9, and 88)

[72] I. Holmes-Gentle and K. Hellgardt. *A versatile open-source analysis of the limiting efficiency of photo electrochemical water-splitting*. Scientific Reports **8** (2018), 1. doi:10.1038/s41598-018-30959-9. (cited on p. 8)

[73] C. H. Liao, C. W. Huang, and J. C. Wu. *Hydrogen production from semiconductor-based photocatalysis via water splitting*. Catalysts **2** (2012), 490. doi:10.3390/catal2040490. (cited on p. 8)

[74] M. G. Walter, E. L. Warren, J. R. McKone, S. W. Boettcher, Q. Mi, E. A. Santori, and N. S. Lewis. *Solar water splitting cells*. Chemical Reviews **110** (2010), 6446. doi:10.1021/cr1002326. (cited on p. 8)

[75] K. T. Fountaine, H. J. Lewerenz, and H. A. Atwater. *Efficiency limits for photoelectrochemical water-splitting*. Nature Communications **7** (2016), 1. doi:10.1038/ncomms13706. (cited on pp. 8, 10, 61, and 93)

[76] S. Hu, C. Xiang, S. Haussener, A. D. Berger, and N. S. Lewis. *An analysis of the optimal band gaps of light absorbers in integrated tandem photoelectrochemical water-splitting systems*. Energy and Environmental Science **6** (2013), 2984. doi:10.1039/c3ee40453f. (cited on p. 8)

[77] M. R. Shaner, K. T. Fountaine, and H. J. Lewerenz. *Current-voltage characteristics of coupled photodiode-electrocatalyst devices*. Applied Physics Letters **103** (2013). doi:10.1063/1.4822179. (cited on pp. 8, 62, and 93)

[78] Z. Chen, H. N. Dinh, and E. Miller. *Photoelectrochemical water splitting: Standards, experimental methods, and protocols*. Springer. (2013), 126. doi:10.1007/978-1-4614-8298-7. (cited on pp. 9, 71, and 88)

[79] X. Elias, Q. Liu, C. Gimbert-Suriñach, R. Matheu, P. Mantilla-Perez, A. Martinez-Otero, X. Sala, J. Martorell, and A. Llobet. *Neutral water splitting catalysis with a high FF triple junction polymer cell*. ACS Catalysis **6** (2016), 3310. doi:10.1021/acscatal.6b01036. (cited on p. 9)

[80] S. Ye, W. Shi, Y. Liu, D. Li, H. Yin, H. Chi, Y. Luo, N. Ta, F. Fan, X. Wang, and C. Li. *Unassisted photoelectrochemical cell with multimediator modulation for solar water splitting exceeding 4% solar-to-hydrogen efficiency*. Journal of the American Chemical Society **143** (2021), 12499. doi:10.1021/jacs.1c00802. (cited on p. 9)

[81] V. Andrei, R. L. Hoye, M. Crespo-Quesada, M. Bajada, S. Ahmad, M. De Volder, R. Friend, and E. Reisner. *Scalable triple cation mixed halide perovskite–BiVO$_4$ tandems for bias-free water splitting*. Advanced Energy Materials **8** (2018), 1. doi:10.1002/aenm.201801403. (cited on p. 9)

[82] S. Rühle. *Tabulated values of the Shockley-Queisser limit for single junction solar cells*. Solar Energy **130** (2016), 139. doi:10.1016/j.solener.2016.02.015. (cited on p. 10)

[83] B. A. Pinaud, J. D. Benck, L. C. Seitz, A. J. Forman, Z. Chen, T. G. Deutsch, B. D. James, K. N. Baum, G. N. Baum, S. Ardo, H. Wang, E. Miller, and T. F. Jaramillo. *Technical and economic feasibility of centralized facilities for solar hydrogen production via photocatalysis and photoelectrochemistry*. Energy and Environmental Science **6** (2013), 1983. doi:10.1039/c3ee40831k. (cited on pp. 10 and 61)

[84] M. S. Prévot and K. Sivula. *Photoelectrochemical tandem cells for solar water splitting*. The Journal of Physical Chemistry C **117** (2013), 17879. doi:10.1021/jp405291g. (cited on pp. 10 and 61)

[85] L. C. Seitz, Z. Chen, A. J. Forman, B. A. Pinaud, J. D. Benck, and T. F. Jaramillo. *Modeling practical performance limits of photoelectrochemical water splitting based on the current state of materials research*. ChemSusChem **7** (2014), 1372. doi:10.1002/cssc.201301030. (cited on pp. 10 and 61)

[86] H. Helmers, E. Lopez, O. Höhn, D. Lackner, J. Schön, M. Schauerte, M. Schachtner, F. Dimroth, and A. W. Bett. *68.9% efficient GaAs-based photonic power conversion enabled by photon recycling and optical resonance*. Physica Status Solidi - Rapid Research Letters **15** (2021), 1. doi:10.1002/pssr.202100113. (cited on p. 10)

[87] S. Fafard and D. P. Masson. *Perspective on photovoltaic optical power converters*. Journal of Applied Physics **130** (2021). doi:10.1063/5.0070860. (cited on p. 10)

[88] N. Nouri, C. E. Valdivia, M. N. Beattie, J. J. Krich, and K. Hinzer. *Light management in ultra-thin photonic power converters for* 1310 *nm laser illumination*. Optics Express **30** (2022), 23417. doi:10.1364/oe.459680. (cited on p. 10)

[89] R. Kimovec and M. Topic. *Comparison of measured performance and theoretical limits of GaAs laser power converters under monochromatic light.* Facta universitatis - series: Electronics and Energetics **30** (2017), 93. doi:10.2298/fuee1701093k. (cited on p. 10)

[90] E. Yablonovitch. *Statistical ray optics.* Optical Society of America **72** (1982), 899. doi:10.1364/JOSA.72.000899. (cited on pp. 11 and 13)

[91] E. Yablonovitch and G. Cody. *Intensity enhancement in textured optical sheets for solar cells.* IEEE Transactions on Electron Devices **29** (1982), 300. doi:10.1109/T-ED.1986.22753. (cited on pp. 11 and 13)

[92] C. Cho, H. Kim, S. Jeong, S. W. Baek, J. W. Seo, D. Han, K. Kim, Y. Park, S. Yoo, and J. Y. Lee. *Random and V-groove texturing for efficient light trapping in organic photovoltaic cells.* Solar Energy Materials and Solar Cells **115** (2013), 36. doi:10.1016/j.solmat.2013.03.014. (cited on p. 11)

[93] J. D. Myers, W. Cao, V. Cassidy, S. H. Eom, R. Zhou, L. Yang, W. You, and J. Xue. *A universal optical approach to enhancing efficiency of organic-based photovoltaic devices.* Energy and Environmental Science **5** (2012), 6900. doi:10.1039/c2ee21254d. (cited on p. 11)

[94] K. Tvingstedt, S. D. Zilio, O. Inganäs, and M. Tormen. *Trapping light with micro lenses in thin film organic photovoltaic cells.* Optics Express **16** (2008), 21608. doi:10.1364/oe.16.021608. (cited on p. 11)

[95] S. D. Zilio, K. Tvingstedt, O. Inganäs, and M. Tormen. *Fabrication of a light trapping system for organic solar cells.* Microelectronic Engineering **86** (2009), 1150. doi:10.1016/j.mee.2009.02.006. (cited on p. 11)

[96] S. Esiner, T. Bus, M. M. Wienk, K. Hermans, and R. A. J. Janssen. *Quantification and validation of the efficiency enhancement reached by application of a retroreflective light trapping texture on a polymer solar cell.* Advanced Energy Materials **3** (2013), 1013. doi:10.1002/aenm.201300227. (cited on p. 12)

[97] C. Ulbrich, A. Gerber, K. Hermans, A. Lambertz, and U. Rau. *Analysis of short circuit current gains by an anti-reflective textured cover on silicon thin film solar cells.* Progress in Photovoltaics: Research and Applications **21** (2013), 1672. doi:10.1002/pip.2249. (cited on p. 12)

[98] E. Seim, A. Kohler, R. Lukacs, M. A. Brandsrud, E. S. Marstein, E. Olsen, and R. Blümel. *Chaos: A new mechanism for enhancing the optical generation rate in optically thin solar cells.* Chaos **29** (2019), 093132. doi:10.1063/1.5111042. (cited on p. 12)

[99] R. E. Alsaigh, R. Bauer, and M. P. Lavery. *Multi-element lenslet array for efficient solar collection at extreme angles of incidence*. Scientific Reports **10** (2020), 8741. doi:10.1038/s41598-020-65437-8. (cited on p. 12)

[100] R. E. Alsaigh, R. Bauer, and M. P. J. Lavery. *Multi-layer light trapping structures for enhanced solar collection*. Optics Express **28** (2020), 31714. doi:10.1364/oe.403990. (cited on p. 12)

[101] M. Mariano, G. Kozyreff, L. Gerling, P. Romero-Gomez, J. Puigdollers, J. Bravo-Abad, and J. Martorell. *Intermittent chaos for ergodic light trapping in a photonic fiber plate*. Light: Science & Applications **5** (2016), e16216. doi:10.1038/lsa.2016.216. (cited on p. 12)

[102] M. Mariano, F. J. Rodríguez, P. Romero-Gomez, G. Kozyreff, and J. Martorell. *Light coupling into the whispering gallery modes of a fiber array thin film solar cell for fixed partial sun tracking*. Scientific Reports **4** (2014). doi:10.1038/srep04959. (cited on p. 12)

[103] G. Martínez-Denegri, S. Colodrero, Q. Liu, J. Toudert, G. Kozyreff, and J. Martorell. *Ergodic light propagation in a half-cylinder photonic plate for optimal absorption in perovskite solar cells*. Advanced Optical Materials **7** (2019), 1900018. doi:10.1002/adom.201900018. (cited on pp. 12, 23, and 24)

[104] A. Bozzola, M. Liscidini, and L. C. Andreani. *Photonic light-trapping versus lambertian limits in thin film silicon solar cells with 1D and 2D periodic patterns*. Optics Express **20** (2012), 224. doi:10.1364/OE.20.00A224. (cited on p. 13)

[105] T. K. Chong, J. Wilson, S. Mokkapati, and K. R. Catchpole. *Optimal wavelength scale diffraction gratings for light trapping in solar cells*. Journal of Optics **14** (2012), 024012. doi:10.1088/2040-8978/14/2/024012. (cited on p. 13)

[106] S. E. Han and G. Chen. *Toward the Lambertian limit of light trapping in thin nanostructured silicon solar cells*. Nano Letters **10** (2010), 4692. doi:10.1021/nl1029804. (cited on p. 13)

[107] S. B. Mallick, M. Agrawal, and P. Peumans. *Optimal light trapping in ultra-thin photonic crystal crystalline silicon solar cells*. Optics Express **18** (2010), 5691. doi:10.1364/oe.18.005691. (cited on p. 13)

[108] K. X. Wang, Z. Yu, V. Liu, Y. Cui, and S. Fan. *Absorption enhancement in ultrathin solar cells with antireflection and light-trapping nanocone gratings*. Nano letters **12** (2012), 1616. doi:10.1364/pv.2012.pt2c.2. (cited on p. 13)

[109] Y. Yu, L. Huang, and L. Cao. *Semiconductor solar superabsorbers*. Scientific Reports **4** (2014), 4107. doi:10.1038/srep04107. (cited on p. 13)

[110] S. Bhattacharya and S. John. *Beyond 30% conversion efficiency in silicon solar cells: A numerical demonstration*. Scientific Reports **9** (2019), 12482. doi:10.1038/s41598-019-48981-w. (cited on p. 13)

[111] M. S. Branham, W. C. Hsu, S. Yerci, J. Loomis, S. V. Boriskina, B. R. Hoard, S. E. Han, and G. Chen. *15.7% efficient 10-µm-thick crystalline silicon solar cells using periodic nanostructures*. Advanced Materials **27** (2015), 2182. doi:10.1002/adma.201405511. (cited on p. 13)

[112] M. L. Hsieh, A. Kaiser, S. Bhattacharya, S. John, and S. Y. Lin. *Experimental demonstration of broadband solar absorption beyond the Lambertian limit in certain thin silicon photonic crystals*. Scientific Reports **10** (2020), 11857. doi:10.1038/s41598-020-68704-w. (cited on p. 13)

[113] A. Mavrokefalos, S. E. Han, S. Yerci, M. S. Branham, and G. Chen. *Efficient light trapping in inverted nanopyramid thin crystalline silicon membranes for solar cell applications*. Nano Letters **12** (2012), 2792. doi:10.1021/nl2045777. (cited on p. 13)

[114] N. Tavakoli, R. Spalding, A. Lambertz, P. Koppejan, G. Gkantzounis, C. Wan, R. Röhrich, E. Kontoleta, A. F. Koenderink, R. Sapienza, M. Florescu, and E. Alarcon-Llado. *Over 65% sunlight absorption in a 1µm si slab with hyperuniform texture*. ACS Photonics **9** (2022), 1206. doi:10.1021/acsphotonics.1c01668. (cited on p. 13)

[115] D. M. Callahan, J. N. Munday, and H. A. Atwater. *Solar cell light trapping beyond the ray optic limit*. Nano Letters **12** (2012), 214. doi:10.1021/nl203351k. (cited on p. 13)

[116] E. R. Martins, J. Li, Y. Liu, V. Depauw, Z. Chen, J. Zhou, and T. F. Krauss. *Deterministic quasi-random nanostructures for photon control*. Nature Communications **4** (2013), 2665. doi:10.1038/ncomms3665. (cited on p. 13)

[117] O. D. Miller, E. Yablonovitch, and S. R. Kurtz. *Strong internal and external fluorescence as solar cell approach the Shockley-Queisser efficiency limit*. IEEE Journal of Photovoltaics **2** (2012), 303. doi:10.1109/JPHOTOV.2012.2198434. (cited on p. 13)

[118] V. Ganapati, O. D. Miller, and E. Yablonovitch. *Light trapping textures designed by electromagnetic optimization for subwavelength thick solar cells*. IEEE Journal of Photovoltaics **4** (2014), 175. doi:10.1109/JPHOTOV.2013.2280340. (cited on p. 13)

[119] Z. Yu, A. Raman, and S. Fan. *Fundamental limit of nanophotonic light trapping in solar cells*. Proceedings of the National Academy of Sciences **107** (2010), 17491. doi:10.1073/pnas.1008296107. (cited on p. 13)

[120] P. N. Saeta, V. E. Ferry, D. Pacifici, J. N. Munday, and H. A. Atwater. *How much can guided modes enhance absorption in thin solar cells?* Optics Express **17** (2009), 20975. doi:10.1364/oe.17.020975. (cited on p. 13)

[121] Z. Yu, A. Raman, and S. Fan. *Fundamental limit of light trapping in grating structures*. Optics Express (2010), A366. doi:10.1073/pnas.1008296107. (cited on p. 13)

[122] J. Kim, S. Jung, and I. Jeong. *Optical modeling for polarization-dependent optical power dissipation of thin-film organic solar cells at oblique incidence*. Journal of the Optical Society of Korea **16** (2012), 6. doi:10.3807/JOSK.2012.16.1.006. (cited on p. 15)

[123] L. A. A. Pettersson, L. S. Roman, and O. Inganäs. *Modeling photocurrent action spectra of photovoltaic devices based on organic thin films*. Journal of Applied Physics **86** (1999), 487. doi:10.1063/1.370757. (cited on p. 15)

[124] P. Peumans, A. Yakimov, and S. R. Forrest. *Small molecular weight organic thin-film photodetectors and solar cells*. Journal of Applied Physics **93** (2003), 3693. doi:10.1063/1.1534621. (cited on p. 15)

[125] C. C. Katsidis and D. I. Siapkas. *General transfer-matrix method for optical multilayer systems with coherent, partially coherent, and incoherent interference*. Applied Optics **41** (2002), 3978. doi:10.1364/AO.41.003978. (cited on p. 18)

[126] C. L. Mitsas and D. I. Siapkas. *Generalized matrix method for analysis of coherent and incoherent reflectance and transmittance of multilayer structures with rough surfaces, interfaces, and finite substrates*. Applied Optics **34** (1995), 1678. doi:10.1364/AO.34.001678. (cited on p. 18)

[127] J. Thijssen. *Computational physics*. Cambridge University Press. (2007), 638. doi:10.1017/CBO9781139171397. (cited on p. 20)

[128] S. Boyd and L. Vandenberghe. *Convex optimization*. Cambridge University Press. (2004). doi:10.1017/CBO9780511804441. (cited on p. 20)

[129] M. J. Kochenderfer and T. A. Wheeler. *Algorithms for optimization*. The MIT Press. (2019). (cited on pp. 20 and 21)

[130] S. Luke. *Essentials of metaheuristics*. Lulu. (2016). doi:10.1007/s10710-011-9139-0. (cited on pp. 20 and 21)

[131] A. P. Engelbrecht. *Computational intelligence: An introduction*. John Wiley & Sons. (2002). doi:10.1007/978-3-540-78293-3_1. (cited on pp. 20 and 21)

[132] J. Watt, R. Borhani, and A. K. Katsaggelos. *Machine learning refined: Foundations, algorithms, and applications*. Cambridge University Press. (2016). doi:10.1017/CBO9781316402276. (cited on p. 20)

[133] R. H. Landau and M. J. Páez. *Computational physics problem solving with computers*. John Wiley & Sons. (2007). doi:10.1002/9783527618835. (cited on p. 20)

[134] J. Nocedal and S. J. Wright. *Numerical optimization*. Springer. (2006). doi:10.1007/978-0-387-40065-5. (cited on p. 20)

[135] J. D. Pintér. *Global optimization in action*. Springer. (1996). doi:10.1007/978-1-4757-2502-5. (cited on p. 21)

[136] J. H. Holland. *Adaptation in natural and artificial systems*. The MIT Press. (1975). doi:10.7551/mitpress/1090.001.0001. (cited on p. 21)

[137] The MathWorks Inc. *MATLAB version: 9.7.1 (R2019b)* (2019). (cited on pp. 26 and 62)

[138] J. Werner, G. Nogay, F. Sahli, T. C. J. Yang, M. Bräuninger, G. Christmann, A. Walter, B. A. Kamino, P. Fiala, P. Löper, S. Nicolay, Q. Jeangros, B. Niesen, and C. Ballif. *Complex refractive indices of cesium-formamidinium-based mixed-halide perovskites with optical band gaps from 1.5 to 1.8 eV*. ACS Energy Letters **3** (2018), 742. doi:10.1021/acsenergylett.8b00089. (cited on p. 33)

[139] *Vishay blue LEDs*. https://www.vishay.com/en/leds/blue/. Accessed: 2023-05-22. (cited on pp. 35 and 36)

[140] *Vishay green LEDs*. https://www.vishay.com/en/leds/green/. Accessed: 2023-05-22. (cited on pp. 35 and 36)

[141] *Vishay red LEDs*. https://www.vishay.com/en/leds/red/. Accessed: 2023-05-22. (cited on pp. 35 and 36)

[142] B. Li, V. Ferguson, S. R. P. Silva, and W. Zhang. *Defect engineering toward highly efficient and stable perovskite solar cells*. Advanced Materials Interfaces **5** (2018), 1. doi:10.1002/admi.201800326. (cited on p. 36)

[143] P. Roy, N. K. Sinha, S. Tiwari, and A. Khare. *A review on perovskite solar cells: Evolution of architecture, fabrication techniques, commercialization issues and status*. Solar Energy **198** (2020), 665. doi:10.1016/j.solener.2020.01.080. (cited on p. 36)

[144] P. Tonui, S. O. Oseni, G. Sharma, Q. Yan, and G. T. Mola. *Perovskites photovoltaic solar cells: An overview of current status*. Renewable and Sustainable Energy Reviews **91** (2018), 1025. doi:10.1016/j.rser.2018.04.069. (cited on p. 36)

[145] S. S. Dunkle, R. J. Helmich, and K. S. Suslick. *BiVO₄ as a visible-light photocatalyst prepared by ultrasonic spray pyrolysis*. Journal of Physical Chemistry C **113** (2009), 11980. doi:10.1021/jp903757x. (cited on pp. 49 and 53)

[146] A. Iwase and A. Kudo. *Photoelectrochemical water splitting using visible-light-responsive BiVO₄ fine particles prepared in an aqueous acetic acid solution*. Journal of Materials Chemistry **20** (2010), 7536. doi:10.1039/c0jm00961j. (cited on pp. 49 and 53)

[147] K. P. S. Parmar, H. J. Kang, A. Bist, P. Dua, J. S. Jang, and J. S. Lee. *Photocatalytic and photoelectrochemical water oxidation over metal-doped monoclinic BiVO₄ photoanodes*. ChemSusChem **5** (2012), 1926. doi:10.1002/cssc.201200254. (cited on pp. 49 and 53)

[148] D. J. Payne, M. D. Robinson, R. G. Egdell, A. Walsh, J. McNulty, K. E. Smith, and L. F. Piper. *The nature of electron lone pairs in BiVO₄*. Applied Physics Letters **98** (2011), 1. doi:10.1063/1.3593012. (cited on pp. 49 and 53)

[149] S. M. Thalluri, C. M. Suarez, M. Hussain, S. Hernandez, A. Virga, G. Saracco, and N. Russo. *Evaluation of the parameters affecting the visible-light-induced photocatalytic activity of monoclinic BiVO₄ for water oxidation*. Industrial and Engineering Chemistry Research **52** (2013), 17414. doi:10.1021/ie402930x. (cited on pp. 49 and 53)

[150] R. Venkatesan, S. Velumani, and A. Kassiba. *Mechanochemical synthesis of nanostructured BiVO₄ and investigations of related features*. Materials Chemistry and Physics **135** (2012), 842. doi:10.1016/j.matchemphys.2012.05.068. (cited on pp. 49 and 53)

[151] J. Yu and A. Kudo. *Effects of structural variation on the photocatalytic performance of hydrothermally synthesized BiVO₄*. Advanced Functional Materials **16** (2006), 2163. doi:10.1002/adfm.200500799. (cited on pp. 49 and 53)

[152] L. Zhou, W. Wang, S. Liu, L. Zhang, H. Xu, and W. Zhu. *A sonochemical route to visible-light-driven high-activity BiVO₄ photocatalyst*. Journal of Molecular Catalysis A: Chemical **252** (2006), 120. doi:10.1016/j.molcata.2006.01.052. (cited on pp. 49 and 53)

[153] J. K. Cooper, S. Gul, F. M. Toma, L. Chen, Y. S. Liu, J. Guo, J. W. Ager, J. Yano, and I. D. Sharp. *Indirect bandgap and optical properties of mono-*

clinic bismuth vanadate. Journal of Physical Chemistry C **119** (2015), 2969. doi:10.1021/jp512169w. (cited on p. 49)

[154] H. Gong, N. Freudenberg, M. Nie, R. V. D. Krol, and K. Ellmer. *BiVO₄ photoanodes for water splitting with high injection efficiency, deposited by reactive magnetron co-sputtering*. AIP Advances **6** (2016). doi:10.1063/1.4947121. (cited on p. 49)

[155] G. Li, Y. Bai, and W. F. Zhang. *Difference in valence band top of BiVO₄ with different crystal structure*. Materials Chemistry and Physics **136** (2012), 930. doi:10.1016/j.matchemphys.2012.08.023. (cited on p. 49)

[156] O. F. Lopes, K. T. Carvalho, A. E. Nogueira, W. Avansi, and C. Ribeiro. *Controlled synthesis of BiVO₄ photocatalysts: Evidence of the role of heterojunctions in their catalytic performance driven by visible-light*. Applied Catalysis B: Environmental **188** (2016), 87. doi:10.1016/j.apcatb.2016.01.065. (cited on p. 49)

[157] P. Madhusudan, M. V. Kumar, T. Ishigaki, K. Toda, K. Uematsu, and M. Sato. *Hydrothermal synthesis of meso/macroporous BiVO₄ hierarchical particles and their photocatalytic degradation properties under visible light irradiation*. Environmental Science and Pollution Research **20** (2013), 6638. doi:10.1007/s11356-013-1694-x. (cited on p. 49)

[158] R. Mirabal-Rojas, O. Depablos-Rivera, S. M. Thalluri, J. C. Medina, M. Bizarro, J. Perez-Alvarez, S. E. Rodil, and A. Zeinert. *Effect of the KOH chemical treatment on the optical and photocatalytic properties of BiVO₄ thin films*. Applied Physics A: Materials Science and Processing **122** (2016). doi:10.1007/s00339-016-9821-4. (cited on p. 49)

[159] F. M. Toma, J. K. Cooper, V. Kunzelmann, M. T. McDowell, J. Yu, D. M. Larson, N. J. Borys, C. Abelyan, J. W. Beeman, K. M. Yu, J. Yang, L. Chen, M. R. Shaner, J. Spurgeon, F. A. Houle, K. A. Persson, and I. D. Sharp. *Mechanistic insights into chemical and photochemical transformations of bismuth vanadate photoanodes*. Nature Communications **7** (2016), 12012. doi:10.1038/ncomms12012. (cited on p. 49)

[160] T. W. Kim and K. S. Choi. *Nanoporous BiVO₄ photoanodes with dual-layer oxygen evolution catalysts for solar water splitting*. Science **343** (2014), 990. doi:10.1126/science.1246913. (cited on p. 51)

[161] D. V. Likhachev, N. Malkova, and L. Poslavsky. *Modified Tauc-Lorentz dispersion model leading to a more accurate representation of absorption features below the bandgap*. Thin Solid Films **589** (2015), 844. doi:10.1016/j.tsf.2015.07.035. (cited on pp. 53, 80, and 81)

[162] A. S. Ferlauto, G. M. Ferreira, J. M. Pearce, C. R. Wronski, R. W. Collins, X. Deng, and G. Ganguly. *Analytical model for the optical functions of amorphous semiconductors from the near-infrared to ultraviolet: Applications in thin film photovoltaics*. Journal of Applied Physics **92** (2002), 2424. doi:10.1063/1.1497462. (cited on pp. 53, 80, and 81)

[163] M. Di, E. Bersch, A. C. Diebold, S. Consiglio, R. D. Clark, G. J. Leusink, and T. Kaack. *Comparison of methods to determine bandgaps of ultrathin HfO_2 films using spectroscopic ellipsometry*. Journal of Vacuum Science & Technology A: Vacuum, Surfaces, and Films **29** (2011), 041001. doi:10.1116/1.3597838. (cited on pp. 53 and 80)

[164] F. Urbach. *The long-wavelength edge of photographic sensitivity and of the electronic absorption of solids*. Physical Review **92** (1953), 1324. doi:10.1103/PhysRev.92.1324. (cited on pp. 53 and 81)

[165] N. Bacalis, E. N. Economou, and M. H. Cohen. *Simple derivation of exponential tails in the density of states*. Physical Review B **37** (1988), 2714. doi:10.1103/PhysRevB.37.2714. (cited on pp. 53 and 81)

[166] J. Jean, T. S. Mahony, D. Bozyigit, M. Sponseller, J. Holovský, M. G. Bawendi, and V. Bulović. *Radiative efficiency limit with band tailing exceeds 30% for quantum dot solar cells*. ACS Energy Letters **2** (2017), 2616. doi:10.1021/acsenergylett.7b00923. (cited on p. 53)

[167] S. D. Wolf, J. Holovsky, S. J. Moon, P. Löper, B. Niesen, M. Ledinsky, F. J. Haug, J. H. Yum, and C. Ballif. *Organometallic halide perovskites: Sharp optical absorption edge and its relation to photovoltaic performance*. Journal of Physical Chemistry Letters **5** (2014), 1035. doi:10.1021/jz500279b. (cited on p. 53)

[168] C. M. Sutter-Fella, D. W. Miller, Q. P. Ngo, E. T. Roe, F. M. Toma, I. D. Sharp, M. C. Lonergan, and A. Javey. *Band tailing and deep defect states in $CH_3NH_3Pb(I_{(1-x)}Br_x)_3$ perovskites as revealed by sub-bandgap photocurrent*. ACS Energy Letters **2** (2017), 709. doi:10.1021/acsenergylett.6b00727. (cited on pp. 53 and 55)

[169] A. Sadhanala, F. Deschler, T. H. Thomas, S. E. Dutton, K. C. Goedel, F. C. Hanusch, M. L. Lai, U. Steiner, T. Bein, P. Docampo, D. Cahen, and R. H. Friend. *Preparation of single-phase films of $CH_3NH_3Pb(I_{1-x}Br_x)_3$ with sharp optical band edges*. The Journal of Physical Chemistry Letters **5** (2014), 2501. doi:10.1021/jz501332v. (cited on p. 53)

[170] E. Ugur, M. Ledinský, T. G. Allen, J. Holovský, A. Vlk, and S. D. Wolf. *Life on the Urbach edge*. Journal of Physical Chemistry Letters **13** (2022), 7702. doi:10.1021/acs.jpclett.2c01812. (cited on p. 53)

[171] J. K. Cooper, S. Gul, F. M. Toma, L. Chen, P. A. Glans, J. Guo, J. W. Ager, J. Yano, and I. D. Sharp. *Electronic structure of monoclinic BiVO₄*. Chemistry of Materials **26** (2014), 5365. doi:10.1021/cm5025074. (cited on p. 53)

[172] M. V. Malashchonak, E. A. Streltsov, D. A. Kuliomin, A. I. Kulak, and A. V. Mazanik. *Monoclinic bismuth vanadate band gap determination by photoelectrochemical spectroscopy*. Materials Chemistry and Physics **201** (2017), 189. doi:10.1016/j.matchemphys.2017.08.053. (cited on p. 53)

[173] S. Stoughton, M. Showak, Q. Mao, P. Koirala, D. A. Hillsberry, S. Sallis, L. F. Kourkoutis, K. Nguyen, L. F. Piper, D. A. Tenne, N. J. Podraza, D. A. Muller, C. Adamo, and D. G. Schlom. *Adsorption-controlled growth of BiVO₄ by molecular-beam epitaxy*. APL Materials **1** (2013). doi:10.1063/1.4824041. (cited on p. 53)

[174] C. Kaiser, O. J. Sandberg, N. Zarrabi, W. Li, P. Meredith, and A. Armin. *A universal Urbach rule for disordered organic semiconductors*. Nature Communications **12** (2021), 1. doi:10.1038/s41467-021-24202-9. (cited on p. 55)

[175] D. W. Miller, G. E. Eperon, E. T. Roe, C. W. Warren, H. J. Snaith, and M. C. Lonergan. *Defect states in perovskite solar cells associated with hysteresis and performance*. Applied Physics Letters **109** (2016). doi:10.1063/1.4963760. (cited on p. 55)

[176] Y. Liang, T. Tsubota, L. P. Mooij, and R. V. D. Krol. *Highly improved quantum efficiencies for thin film BiVO₄ photoanodes*. Journal of Physical Chemistry C **115** (2011), 17594. doi:10.1021/jp203004v. (cited on pp. 55 and 57)

[177] C. Liu, N. P. Dasgupta, and P. Yang. *Semiconductor nanowires for artificial photosynthesis*. Chemistry of Materials **26** (2014), 415. doi:10.1021/cm4023198. (cited on pp. 55 and 57)

[178] S. Wang, P. Chen, Y. Bai, J. H. Yun, G. Liu, and L. Wang. *New BiVO₄ dual photoanodes with enriched oxygen vacancies for efficient solar-driven water splitting*. Advanced Materials **30** (2018), 1. doi:10.1002/adma.201800486. (cited on pp. 55 and 57)

[179] COMSOL AB. *COMSOL Multiphysics version: 5.6* (2020). (cited on p. 59)

[180] A. Grimm, A. Sainte-Marie, G. J. Kramer, and M. Gazzani. *Modeling photovoltaic-electrochemical water splitting devices for the production of hydrogen under real working conditions*. International Journal of Hydrogen Energy **47** (2022), 11764. doi:10.1016/j.ijhydene.2022.01.223. (cited on pp. 62 and 93)

[181] R. A. Janssen and J. Nelson. *Factors limiting device efficiency in organic pho-tovoltaics*. Advanced Materials **25** (2013), 1847. doi:10.1002/adma.201202873. (cited on pp. 62 and 93)

[182] P. Mantilla-Perez, T. Feurer, J. P. Correa-Baena, Q. Liu, S. Colodrero, J. Toudert, M. Saliba, S. Buecheler, A. Hagfeldt, A. N. Tiwari, and J. Martorell. *Monolithic CIGS-perovskite tandem cell for optimal light harvesting without current match-ing*. ACS Photonics **4** (2017), 861. doi:10.1021/acsphotonics.6b00929. (cited on p. 62)

[183] S. M. Hosseini, N. Tokmoldin, Y. W. Lee, Y. Zou, H. Y. Woo, D. Neher, and S. Shoaee. *Putting order into PM6:Y6 solar cells to reduce the Langevin recombination in 400 nm thick junction*. Solar RRL **2000498** (2020), 1. doi:10.1002/solr.202000498. (cited on p. 63)

[184] L. Bolzonello, F. Bernal-Texca, L. G. Gerling, J. Ockova, E. Collini, J. Martorell, and N. F. V. Hulst. *Photocurrent-detected 2D electronic spectroscopy reveals ul-trafast hole transfer in operating PM6/Y6 organic solar cells*. Journal of Physical Chemistry Letters **12** (2021), 3983. doi:10.1021/acs.jpclett.1c00822. (cited on p. 65)

[185] Z. Chen, T. F. Jaramillo, T. G. Deutsch, A. Kleiman-Shwarsctein, A. J. Forman, N. Gaillard, R. Garland, K. Takanabe, C. Heske, M. Sunkara, E. W. McFar-land, K. Domen, E. L. Milled, and H. N. Dinh. *Accelerating materials devel-opment for photoelectrochemical hydrogen production: Standards for methods, definitions, and reporting protocols*. Journal of Materials Research **25** (2010), 3. doi:10.1557/jmr.2010.0020. (cited on pp. 71 and 88)

[186] G. Hodes. *Photoelectrochemical cell measurements: Getting the basics right*. Journal of Physical Chemistry Letters **3** (2012), 1208. doi:10.1021/jz300220b. (cited on pp. 71 and 88)

[187] A. Tejada, L. Montañez, C. Torres, P. Llontop, L. Flores, F. D. Zela, A. Win-nacker, and J. A. Guerra. *Determination of the fundamental absorption and optical bandgap of dielectric thin films from single optical transmittance measurements*. Applied Optics **58** (2019), 9585. doi:10.1364/ao.58.009585. (cited on p. 79)

[188] D. Poelman and P. F. Smet. *Methods for the determination of the optical constants of thin films from single transmission measurements: A critical review*. Journal of Physics D: Applied Physics **36** (2003), 1850. doi:10.1088/0022-3727/36/15/316. (cited on pp. 79 and 80)

[189] F. A. Jenkins and H. E. White. *Fundamentals of optics*. McGraw-Hill. (1976). (cited on pp. 79 and 80)

[190] F. Wooten. *Optical properties of solids*. Academic Press. (1972). doi:10.1016/0165-1633(89)90057-9. (cited on pp. 79 and 80)

[191] E. Palik. *Handbook of optical constants of solids*. Academic Press. (1991). doi:10.1016/C2009-0-20920-2. (cited on p. 79)

[192] F. Abdel Wahab, F. El-Diasty, and M. Abdel-Baki. *Dispersion dependence of second-order refractive index and complex third-order optical susceptibility in oxide glasses*. Physics Letters A **373** (2009), 3855. doi:10.1016/j.physleta.2009.08.031. (cited on p. 80)

[193] R. Synowicki. *Spectroscopic ellipsometry characterization of indium tin oxide film microstructure and optical constants*. Thin Solid Films **313-314** (1998), 394. doi:10.1016/S0040-6090(97)00853-5. (cited on p. 80)

[194] Y. Yang, X. Sun, B. Chen, C. Xu, T. Chen, C. Sun, B. Tay, and Z. Sun. *Refractive indices of textured indium tin oxide and zinc oxide thin films*. Thin Solid Films **510** (2006), 95. doi:10.1016/j.tsf.2005.12.265. (cited on p. 80)

[195] B. von Blanckenhagen, D. Tonova, and J. Ullmann. *Application of the Tauc-Lorentz formulation to the interband absorption of optical coating materials*. Applied Optics **41** (2002), 3137. doi:10.1364/AO.41.003137. (cited on p. 80)

[196] D. Franta, M. Cermák, J. Vohánka, and I. Ohlídal. *Dispersion models describing interband electronic transitions combining Tauc's law and Lorentz model*. Thin Solid Films **631** (2017), 12. doi:10.1016/j.tsf.2017.03.051. (cited on p. 80)

[197] G. E. Jellison, V. I. Merkulov, A. A. Puretzky, D. B. Geohegan, G. Eres, D. H. Lowndes, and J. B. Caughman. *Characterization of thin-film amorphous semiconductors using spectroscopic ellipsometry*. Thin Solid Films **377-378** (2000), 68. doi:10.1016/S0040-6090(00)01384-5. (cited on p. 80)

[198] R. Raciti, R. Bahariqushchi, C. Summonte, A. Aydinli, A. Terrasi, and S. Mirabella. *Optical bandgap of semiconductor nanostructures: Methods for experimental data analysis*. Journal of Applied Physics **121** (2017). doi:10.1063/1.4986436. (cited on p. 80)

[199] G. Cody, B. Brooks, and B. Abeles. *Optical absorption above the optical gap of amorphous silicon hydride*. Solar Energy Materials **8** (1982), 231. doi:10.1016/0165-1633(82)90065-X. (cited on p. 80)

[200] T. Lohner, E. Szilágyi, Z. Zolnai, A. Németh, Z. Fogarassy, L. Illés, E. Kótai, P. Petrik, and M. Fried. *Determination of the complex dielectric function of ion-implanted amorphous germanium by spectroscopic ellipsometry*. Coatings **10** (2020), 480. doi:10.3390/coatings10050480. (cited on p. 80)

[201] A. Alfano, A. Mezzetti, F. Fumagalli, C. Tao, E. Rovera, A. Petrozza, and F. D. Fonzo. *Photoelectrochemical water splitting by hybrid organic-inorganic systems: Setting the path from 2% to 20% solar-to-hydrogen conversion efficiency*. iScience **24** (2021), 102463. doi:10.1016/j.isci.2021.102463. (cited on p. 93)

[202] G. Segev, J. W. Beeman, J. B. Greenblatt, and I. D. Sharp. *Hybrid photoelectro-chemical and photovoltaic cells for simultaneous production of chemical fuels and electrical power*. Nature Materials **17** (2018), 1115. doi:10.1038/s41563-018-0198-y. (cited on p. 93)